THE UNIVERSITY OF CHICAGO

TRANSIENT DYNAMICS OF CONCENTRATED PARTICULATE SUSPENSIONS UNDER SHEAR

A DISSERTATION SUBMITTED TO
THE FACULTY OF THE DIVISION OF THE PHYSICAL SCIENCES
IN CANDIDACY FOR THE DEGREE OF
DOCTOR OF PHILOSOPHY

DEPARTMENT OF PHYSICS

BY
ENDAO HAN

CHICAGO, ILLINOIS
AUGUST 2018

To my family

The greatest obstacle to discovery is not ignorance - it is the illusion of knowledge.

- Daniel J. Boorstin

TABLE OF CONTENTS

LIST OF FIGURES

LIST OF TABLES

ACKNOWLEDGMENTS

I want to express my most sincere gratitude to my advisor, Heinrich Jaeger, for all the support he consistently provided over the years. Nothing that I have been working on at Chicago could have been achieved without his insights, advice, encouragement, and patience. From Heinrich I learnt not only how to be a good scientist, but also how to be a better person. His influnce on me is on a wide range of scales.

At the James Franck Institute, I am extremely lucky to have had the chance to be around faculty who are interested, open minded, and treat every scientific problem seriously. I would like to thank Sidney Nagel and Thomas Witten for many inspiring discussions and good advice. Every moment with them was a memorable learning experience for me. Bozhi Tian always had great ideas during a discussion, and no matter when I sent him an email, he replied in 5 minutes. I would also like to thank my thesis committee members Arvind Murugan and Stephan Meyer, for their valuable inputs on my research and my thesis.

I am very grateful to my collaborators at Chicago and other institutions. Matthieu Wyart showed me how an outstanding theorist thinks. Working with him was both challenging and exciting. Patrick La Riviere provided a lot of help when we set up the ultrasound system, and his lectures kick-started my research with ultrasound. Yin Fang, Yuanwen Jiang, Xianghui Xiao, and Jin Wang opened doors for me that led to brand new research opportunities. I am really glad to have been part of this wonderful collaboration between people with such diverse backgrounds. I enjoyed working with Rui Zhang, Tonia Hsieh, Swapnil Pravin, and Kenneth Bader. I also appreciate the expertise of Qiti Guo, Justin Jureller, Helmut Krebs, Luigi Mazzenga, and John Phillips. They were always there when I was in trouble.

I am particularly thankful to my labmates. Ivo Peters is a good mentor, collaborator, and friend. I can never thank him enough for all the help he offered. I can hardly think of a better person than Nicole James to share an office with for five years. When I needed to work with any chemical that was not tap water, I asked Nicole first. Scott Waitukaitis and Qin Xu provided great help when I was an innocent rookie and had no idea what to do. I

would also like to thank Victor Lee, Yifan Wang, Mengfei He, Sayantan Majumdar, Marc Miskin, Kieran Murphy, Leah Roth, Adam Wang, Melody Lim, Nigel Van Ha, Liang Zhao, Michael van der Naald, Daniel Hexner, Irmgard Bischofberger, Kimberly Weirich, Andrzej Latka, Noah Mitchell, Sofia Magkiriadou, Edward Barry, Tom Caswell, Carlos Orellana, Justin Burton, Michelle Driscoll, Nidhi Pashine, and everyone else in the Jaeger and Nagel labs. Thank you for all the help during this unforgettable journey.

My special appreciation to Tom Mullin, who showed me the beauty of fluids and grains before I came to Chicago.

Last but not least, I thank my parents Peiji Han and Xiuqin Xue for everything they gave me. Special thanks to my lovely wife Junchi Li for her companionship and support through good and bad times. She is my sunshine everyday.

ABSTRACT

Suspensions are dispersions of solid particles in liquids. A remarkable property of dense (concentrated) suspensions is that they can transform from liquid-like at rest to solid-like under sudden impact, and back to liquid-like when the applied stress is removed. Previous work showed that this impact-induced solidification involves rapidly moving jamming fronts. Furthermore, dense suspensions can solidify not only under impact, but also under sudden extension or shear. However, compared to the intensively studied steady-state rheology, these transient dynamics of dense suspensions are still poorly understood, and many details of the sudden solidification process have remained unresolved.

In this thesis we use high-speed ultrasound imaging to non-invasively probe how the interior of a dense suspension responds to impact. By measuring the speed of sound we demonstrate that the solidification proceeds without any detectable increase in packing fraction, and by imaging the evolving flow field we find that the shear intensity is maximized right at the jamming front. Taken together, this provides direct experimental evidence for jamming by shear, rather than densification, as driving the transformation.

To develop a quantitative description of such transient flows, we then study the fronts that appear when dense suspensions are subjected to sudden shear in a quasi-one-dimensional system. We extract the front propagation speed, local shear rate, and stress distributions from the flow field, and map out their dependence on boundary conditions and packing fraction. We show that the experimental findings can be explained by generalizing a phenomenological model originally developed to describe steady-state rheology. This is achieved by introducing a sole additional parameter: the characteristic strain scale that controls the crossover from start-up response to steady-state behavior. Finally, taking advantage of the fact that the shear fronts operate at fixed stress, we are able to map out properties of suspensions in the shear jamming regime, which is difficult if not impossible with standard steady-state rheology.

CHAPTER 1

INTRODUCTION

In our daily lives, most materials we see are in one of three states of matter: solid, liquid, or gas. When a material in one state is broken up into small particles and mixed with a material in another state, rich and interesting phenomena can happen. For example, air is so "soft" that most of the time one can hardly feel its existence. However, when a lot of air bubbles are distributed in water, the foam that forms develops a rigidity that can hold its shape against gravity, and flows only when it is squeezed between one's hands. Another popular example of such mixtures is a suspension of hard cornstarch particles in water, which is sometimes referred to as the "Oobleck" in Dr. Seuss' stories. One striking behavior of this solid-liquid mixtures is that it flows like a viscous fluid under normal conditions, but solidifies under sudden impact. The transition is so dramatic, that people can jog or jump on the surface of such mixture. Yet when they stop moving, the material can no longer support their weight and they sink. This reversible, dynamic fluid-solid transition is the main focus of this thesis.

Suspensions are mixtures of solid particles and liquids. The "particles" can have various shapes, such as spheres, rods, plates, *etc.* Here we consider suspensions comprised of spherical or non-spherical particles with aspect ratio close to 1. We also focus on non-Brownian suspensions, which means that the particles are so big (1 - 100 μm) that the effect of thermal motion can be ignored. Such system is far from thermal equilibrium. We will show that the dynamic fluid-solid transition in a system of this kind is purely driven by stress. The applied stress plays two major roles: it provides kinetic energy for the system to explore phase space, and also it changes the interaction between the particles on a microscopic level. Such microscopic interactions at the points where surfaces of particles come into contact determine the stable (or unstable) configurations that can form locally, and subsequently control the macroscopic mechanical properties of the material. It is the complex interplay of forces arising from hydrodynamic interactions and frictional contacts that makes dense suspensions so rich and fascinating.

1.1 Steady-state rheology of suspensions

The mechanical properties of suspensions are normally characterized by rheology experiments. Rheology is the study of the deformation and flow of matter [1]. When a shear stress Σ is applied on a solid, it deforms and reaches a finite shear strain γ. The ratio $G = \Sigma/\gamma$ is called the shear modulus, which represents the rigidity of the solid. In comparison, for a fluid sheared under a constant stress, the deformation keeps accumulating. Now shear stress controls the rate of deformation, or strain rate, instead of the shear strain. For a fluid under simple shear, the ratio between Σ and the shear rate $\dot{\gamma}$ is its viscosity $\eta = \Sigma/\dot{\gamma}$.

The research on how solid particles change the viscosity of suspensions dates back to Einstein [2]. In his PhD thesis, he calculated the viscosity of very dilute suspensions where the interactions between particles can be ignored, and found a linear relation between the viscosity of the suspension and the volume fraction of the particles (also called the packing fraction) ϕ:

$$\eta_{\mathrm{r}} \equiv \frac{\eta}{\eta_0} = 1 + 2.5\phi, \tag{1.1}$$

where η is the viscosity of the suspension, η_0 is the viscosity of the solvent or the liquid phase in the suspension, and η_{r} is the relative viscosity. For denser suspensions, higher order terms need to be taken into consideration [3, 4].

On the extreme end of the ϕ axis we have the phenomenon of jamming [5, 6]. This occurs when the particle concentration becomes so large, and there is so little space for each particle to move, that the whole system can not flow any more. This critical packing fraction is named the jamming packing fraction ϕ_{J}. For mono-disperse hard spheres, the jamming point approaches random close packing $\phi_{\mathrm{J}} = \phi_{\mathrm{RCP}} \approx 0.64$ as the system size goes to infinity [5]. For a dense suspension, while ϕ approaches ϕ_{J}, the viscosity diverges. This behavior is captured by a more general relation between η_r and ϕ,

$$\eta_\mathrm{r} = \left(1 - \frac{\phi}{\phi_\mathrm{J}}\right)^{-\alpha}, \tag{1.2}$$

which is based on the work of Maron and Pierce ($\alpha = 2$) [7], Krieger and Dougherty ($\alpha = 2.5\phi_\mathrm{J}$) [8], Brady [9], and others. Krieger and Dougherty's model [8] reproduces Einstein's equation (Eq. 1.1) in the low-ϕ limit, but based on experimental results obtained from both colloidal and non-colloidal suspensions, Maron and Pierce's model [7] better describes the data [10]. Here in this thesis we use $\alpha = 2$.

While the suspension viscosity is a function of the packing fraction, $\eta_\mathrm{r}(\phi)$, the mechanical properties of the suspension are also dependent on how fast or how strongly it is sheared. For so-called Newtonian fluids like air, water or glycerol, the viscosity is independent of the shear rate $\dot{\gamma}$. In non-Newtonian fluids the viscosity depends on applied shear rate or shear stress. The fluids whose viscosity increases with $\dot{\gamma}$ are called shear thickening fluids, and cornstarch-water mixtures are a typical example. In comparison, the fluids whose viscosity decreases while $\dot{\gamma}$ increases are called shear thinning fluids, such as paint or blood. Another type of non-Newtonian fluid flows only when the applied shear stress exceeds a certain yield stress, for example foam or toothpaste, and they are referred to as Bingham fluids.

In practice, suspensions can exhibit different non-Newtonian behaviors under different steady-state driving conditions, as shown in Fig. 1.1 [11]. Correspondingly, various mechanisms have been proposed. At low shear stress, suspensions can be Newtonian (at low ϕ), shear thinning, or have a non-zero yield stress (at high ϕ). The possible causes of shear thinning include attractive interactions [12, 13], repulsive interactions [14], changes in particle structure (entropic) [15], plus others [16]. As the applied shear stress increases, there often is a Newtonian regime where η_r remains constant, and then the suspension shear thickens. At a relatively low packing fraction, typically up to $\phi \approx 0.4$, the increase in η_r is mild and continuous. This behavior is named continuous shear thickening (CST) [17]. A model

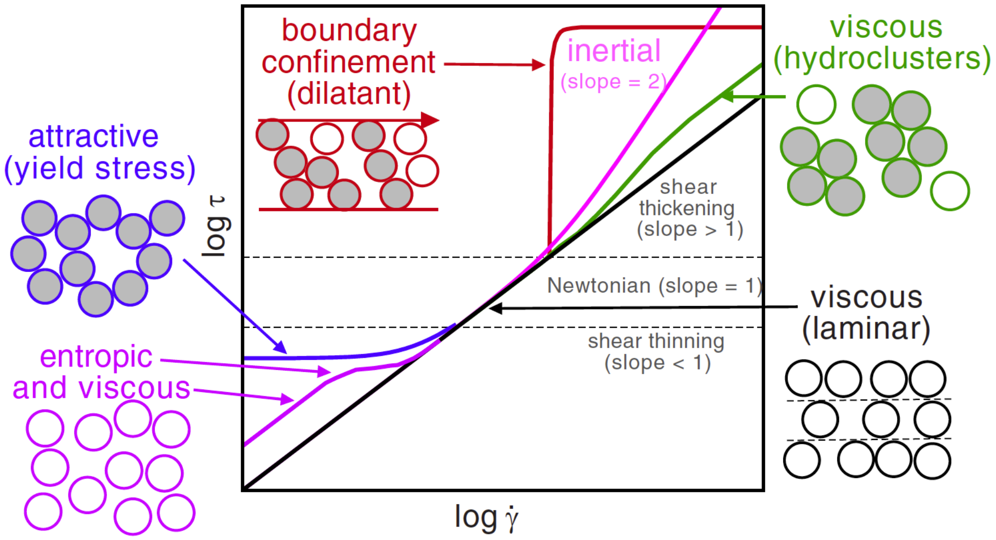

Figure 1.1: Different regimes of suspension rheology and corresponding mechanisms. Figure reproduced from Brown and Jaeger (2014) [11] with permission.

based on hydrodynamic interactions between particles was introduced by Brady and Bossis [18, 19], which demonstrated that, at high enough Péclet number, particles form clusters due to hydrodynamic couplings. This model is normally referred to as the hydrocluster model, and hydroclusters have been observed experimentally with confocal microscopy [15]. At higher packing fractions, typically above $\phi \approx 0.5$, a more dramatic increase in η_r can be observed, where η_r shoots up discontinuously as a function of $\dot{\gamma}$ [20]. Consequently, this behavior is named discontinuous shear thickening (DST). For steady-state rheology, Brown and Jaeger [21] related DST to frustrated dilation, which pointed out the significance of direct particle-particle contacts in the process of shear thickening [22, 23].

1.2 Shear jamming in dry granular materials and in dense suspensions

Jamming is the onset of rigidity in granular materials [5, 6, 12]. For frictionless particles, jamming can be achieved by increasing the packing fraction ϕ across the jamming point

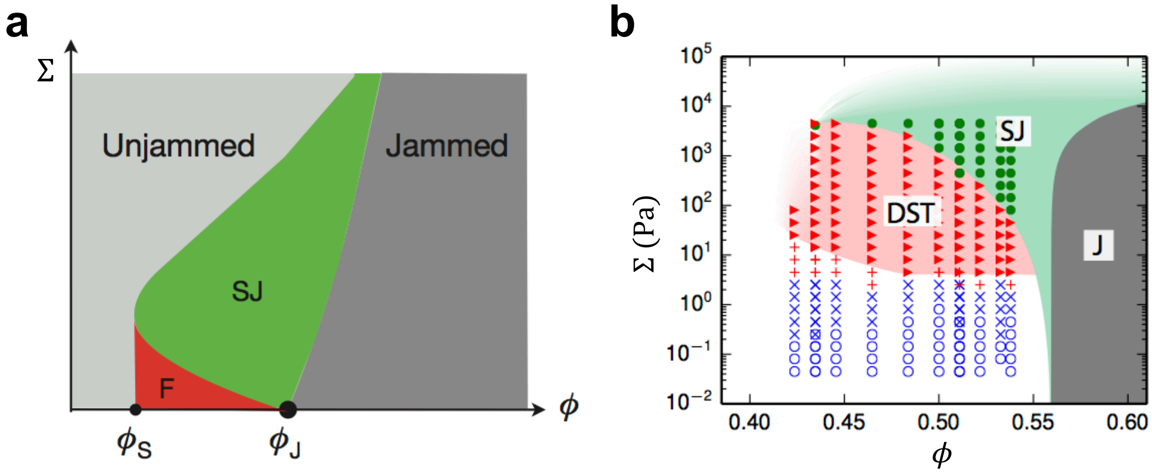

Figure 1.2: Shear jamming state diagrams for dry grains (a) and suspensions (b). F represents the fragile state, DST represents discontinuous shear thickening, SJ represents the shear jammed state, and J represents the frictionless jammed state. Figure (a) reproduced from Bi *et al.* (2011) [24]. Figure (b) reproduced from Peters *et al.* (2016) [25]

ϕ_J [26]. Applied shear stress Σ unjams the system when Σ exceeds its yield stress Σ_{yield}. When the interaction between particles is frictional, the system can be jammed by shear at a packing fraction below ϕ_J [24]. As shown in Fig. 1.2(a), for a two-dimensional dry granular system under quasi-static pure shear, while ϕ is in the range of $\phi_S < \phi < \phi_J$, the system goes through three different states as Σ increases: In the fragile state (red), the strong force networks [1] only percolate in the compression direction, so perturbations in the transverse direction can cause instability in the system [6, 24]. At higher Σ, the strong force networks percolate in all directions, and the system reaches a shear jammed state (green). At an even higher Σ, the jammed solid yields and goes into the unjammed regime (light grey). Jamming by shear was also found in frictionless systems [27] or with weakly attractive particles [28] by numerical simulations.

Shear jamming in dense suspensions was observed by Peters *et al.* [25] with a wide gap Couette cell. The macroscopic feature of shear jammed suspensions is that they develop

---

[1] Strong force is defined as $F > F_{\text{ave}}$, where F is the local contact forces, and F_{ave} is the average of F across the whole system [24].

a non-zero shear modulus [2]. A state diagram has been mapped out for dense suspensions under steady-state driving conditions as shown in Fig. 1.2(b). Like dry granular systems, in suspensions the transitions are also controlled by ϕ and Σ. One major difference is that at low Σ, suspensions flow like a viscous fluid because of the lubrication interaction between the particles. The strongly non-Newtonian rheological properties become most pronounced at high ϕ and Σ, where suspensions start to exhibit characteristics also found in dry granular material [6, 24, 26, 29, 30]. Recent experiments [23, 31, 32, 33, 34, 35] and numerical simulations [36, 37, 38, 39] point to the existence of a stress threshold above which the dominant interaction between particles switches from hydrodynamic lubrication to frictional contact forces.

In dry granular systems, there are three interesting thresholds: a lower boundary in packing fraction ϕ_{S}, below which the system can not shear jam; an onset stress $\Sigma_{\mathrm{SJ}}(\phi)$ above which shear jamming is obtained, and a strain scale that represents the necessary rearrangement of the particle configurations from a uniformly distributed initial state into contact networks [40]. In suspensions there are also three scales: a lower boundary for shear jamming at packing fraction ϕ_{m}, a stress threshold Σ^* that is related to the break-down of the lubrication layer between particles, and a strain scale γ^*. The stress scale Σ^* is relatively well understood based on studies using steady-state rheology. In contrast, prior to the work in this thesis, ϕ_{m} was never tested experimentally, and the importance of γ^* was not recognized, especially for transient phenomena. These will be discussed in Chapter 4.

1.3 Wyart-Cates model for steady-state rheology

The idea that there is a transition in particle-particle interactions from hydrodynamic lubrication forces to frictional contact forces and that this transition should be controlled by the

---

[2] Some literature does not clearly distinguish shear thickening and jamming. Sometimes discontinuous shear thickening is referred to as "temporary jamming". In this thesis, jamming is only designated to a state that does not flow under applied stress (with a non-zero shear modulus) during the time scale of the experiments.

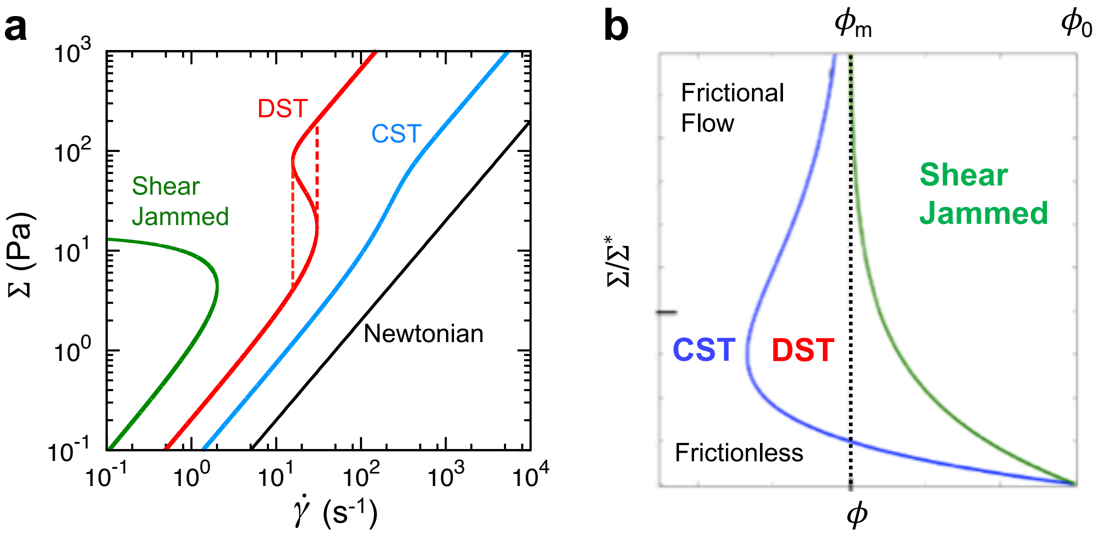

Figure 1.3: Wyart-Cates model for suspension rheology. (a) Examplary Σ-$\dot{\gamma}$ relations for Newtonian, CST, DST, and SJ suspensions. (b) State diagram. Panel (b) reproduced from Wyart and Cates (2014) [41].

applied stress forms the basis of a phenomenological model developed by Wyart and Cates [41]. This model unifies CST, DST and jamming under a common framework for suspensions under conditions of steady-state driving. The central ideas are as follows:

(1) Frictional contacts between particles will be made beyond a characteristic pressure P^*. The fraction of frictional contacts $f(P)$ should be a smooth function that grows with P, such as:

$$f(P) = 1 - \exp(-P/P^*). \tag{1.3}$$

(2) The packing fraction ϕ_J at which jamming occurs is known to depend on the friction coefficient [42]. In suspensions, ϕ_J must then depend on P, and this can be captured by a linear interpolation

$$\phi_\mathrm{J}(P) = f(P)\phi_\mathrm{m} + [1 - f(P)]\,\phi_0, \tag{1.4}$$

where ϕ_0 and ϕ_m are the frictionless and frictional jamming packing fractions, respectively. The exact value of ϕ_m is controlled by the friction between particles. Importantly, "friction" here is a phenomenological parameter that can have different microscopic origins. It can be the coefficient of friction [31, 39], surface roughness of particles [43, 44], interactions between polymer brushes [34], or hydrogen bonding [45].

(3) When a suspension with packing fraction ϕ is under shear, the ratio between normal stress P and shear rate $\dot{\gamma}$ diverges at ϕ_{J} because that is where the viscosity diverges (see Eq. 1.2):

$$\frac{P}{\dot{\gamma}} \propto \left[1 - \frac{\phi}{\phi_{\mathrm{J}}(P)}\right]^{-\alpha}. \tag{1.5}$$

For frictionless particles the exponent α can be computed analytically, leading to $\alpha = 2.85$ [29], whereas for frictional particles it is smaller [46]. Here we pick $\alpha = 2$ for simplicity, a value also in good agreement with previous experimental results [32, 47, 48].

(4) Eqs. 1.3, 1.4, and 1.5 allow one to compute $P(\dot{\gamma})$, eventually leading to a phase diagram predicting CST, DST, and jamming in the (ϕ, P) plane. A further prediction of the shear stress can be obtained following the relation $\Sigma = \mu P$, where μ is the macroscopic friction [32]. In principle, μ depends on P and ϕ, but in practice the dependence is weak, thus μ can be well approximated as a constant of order one. Therefore, we can replace P with Σ, and P^* with Σ^* in Eqs. 1.3, 1.4, and 1.5. Then Eq 1.5 will have the same form as Eq. 1.2.

Some Σ-$\dot{\gamma}$ relations predictions by the Wyart-Cates model are shown in Fig. 1.3 (a). At $\phi = 0$, the system consists only of solvent and thus is a Newtonian fluid. For a denser suspension, the curve continuously shifts towards larger η as Σ increases. In the CST regime, there is a one-to-one correspondence between $\dot{\gamma}$ and Σ. At even higher ϕ, the Σ-$\dot{\gamma}$ curve becomes sigmoidal. For curves like this, stress controlled experiments and rate controlled experiments will lead to different results, because for each Σ there is only one corresponding $\dot{\gamma}$, but for some $\dot{\gamma}$, there are more than one possible Σ. A stress controlled experiment will reproduce the solid red curve in Fig. 1.3 (a), while in a rate controlled experiment discontinuous jumps will happen as shown by the dashed red lines, and there will be hysteresis [49]. In this regime, we obtain DST. When $\phi > \phi_{\mathrm{m}}$, the Σ-$\dot{\gamma}$ curve intersects with the vertical axis where $\dot{\gamma} = 0\ \mathrm{s}^{-1}$. At the intersection, the suspension is in a state of zero shear rate, but non-zero shear stress, which means that it must have developed a non-zero shear modulus, i.e., must have turned into a solid. The stress at the intersection therefore is the onset stress of shear jamming Σ_{SJ}.

From the Σ-$\dot{\gamma}$ curves, a state diagram is obtained as shown in Fig. 1.3 (b). In steady-state rheology, the state of a suspension is controlled by two parameters ϕ and Σ. Here we call it the $\eta(\phi, \Sigma)$ rheology. This phenomenological model allows us to predict the various behaviors of an unknown suspension by measuring four parameters (η_0, ϕ_0, ϕ_{m}, and Σ^*) with a rheometer, without the necessity of knowing any details about the material on the microscopic level.

1.4 Dynamic jamming and transient flows under impact, extension, and shear

Although steady-state rheology of dense suspensions have been studied extensively in the past decade or so, the experimental observation of shear jamming under steady-state conditions occurred only very recently [25]. In contrast, dynamic jamming of dense suspensions was noticed much earlier as transient phenomena. Under a wide range of dynamic conditions, dense suspensions can undergo a fluid-solid transformation, for example ahead of quickly sinking objects [50, 51], during sudden impact at their free surface [52, 53, 54, 55], under shear [25] or during rapid extension [56]. Detailed investigation of the dynamics during impact has shown how such solidification is associated with a propagating front that converts fluid-like, unjammed suspension into a solid-like, jammed material in its wake [52, 57]. This dynamic front moves through the suspension with a speed that can be much greater than that of the impactor itself.

To explain "impact-activated solidification" and the formation of the front, a model was proposed [52] that assumed the impact pushes the particles closer together until they jam. This densification scenario was based on the standard jamming phase diagram for frictionless hard particles, where entry into a jammed state requires an increase in particle packing fraction ϕ [5]. Since the volume of particles is conserved, the front propagation speed U_{f} along the direction of impact then is related to the impactor speed U_{p} via [58]

$$U_{\mathrm{f}} = \frac{\phi_{\mathrm{J}}}{\phi_{\mathrm{J}} - \phi} U_{\mathrm{p}}, \tag{1.6}$$

where ϕ_{J} is the packing fraction at which jamming occurs and $\phi < \phi_{\mathrm{J}}$ is the packing fraction of the initially unjammed suspension at rest. The closer the initial packing fraction is to jamming, the faster the front will propagate, in principle diverging at ϕ_{J}. This model shows excellent agreement with measurements of U_{f} in systems where the local packing fraction can change easily, such as dry granular particle layers that are being compacted snowplough-like from one end [58].

However, this model has certain limitations. Firstly, since compression in required, it does not explain why suspensions can also jam under shear or extension. Secondly, since liquid is effectively incompressible for speeds U_{p} that are only several meters per second, compression would imply migration of particles. Since the particles are non-Brownian, the concentrated regions would be unable to return to the original state when the stress is removed, which contradicts experimental observations. Lastly, as shown in [57] where the flow field in 2D was measured accurately, the suspension does not really jam before the front interacts with a solid boundary. A small but definitely non-zero velocity gradient was observed behind the freely propagating front, which means the suspension is only solid-like, but not a solid yet. All these issues point to the need for a revised and more detailed understanding, which is the focus of this work.

1.5 The scope of this thesis

The major goal of this work is to understand the transient dynamics of dense particulate suspensions, especially in the shear jamming regime. The main body of this thesis is comprised of four parts: In Chapter 2 we introduce several ultrasound techniques that are useful for characterizing the properties of suspensions, including imaging interior flows, measuring the bulk modulus using the speed of sound, and measuring the porosity of porous micro particles. Chapter 3 shows how we applied some of these ultrasound techniques to understand the impact-activated solidification of dense suspensions. We found that there is no measurable variation in packing fraction during the jamming process, and showed that the impact-activated front is, in fact, a propagating shear front. Chapter 4 points out that the $\eta(\phi, \Sigma)$ rheology is not sufficient to explain the transient flows. To fix this, we generalize the original Wyart-Cates model by introducing a term $g(\gamma)$ that accounts for the accumulated shear strain in the system. This generalized model is then validated using a quasi-one dimensional wide-gap shear experiment. Chapter 5 demonstrates how the steady-state shear jamming states predicted by the Wyart-Cates model can by realized in a stress controlled rheology experiment that exploits the transient shear flows instead of conventional steady-state rheology. Chapter 6 contains conclusions and outlines some open questions that future work might address.

CHAPTER 2

ULTRASOUND TECHNIQUES FOR STUDYING SUSPENSIONS

2.1 Introduction

Compared to the Higgs boson or exoplanets, colloidal or non-colloidal particles are much easier to visualize. However, imaging is still a challenging task for soft matter experiments in general, because they may involve a wide range of length scales, require a high temporal resolution, need information deep in the bulk, or deal with optically opaque materials [59]. To understand transient dynamics of dense suspensions, all these challenges must be met.

As an important diagnostic imaging technique, ultrasound has been studied extensively in medicine. At the same time, it has become a useful tool for granular material and suspensions, either to make observations, or to manipulate the tested material. For example, diffusion acoustic wave spectroscopy (DAWS) was developed to measure relative velocity and strain rate in suspensions [60]. Combined with steady-state rheology, ultrasound speckle velocimetry has been used to measure the flow field [61, 62]. The transmission of compression or shear waves can be used to probe the mechanical properties of jammed granular materials [63, 64, 65, 66]. As a well developed technique, ultrasound has a lot of potential for soft matter experiments, especially for aqueous but optically opaque materials.

One advantage of ultrasound is its high acquisition frequency. One major limitation, however, is the attenuation due to scattering or absorption, which limits the penetration depth of the signals [67]. Standard medical ultrasound has a frequency f range of 1-20 MHz, and is coupled [1] to water or soft tissues, in which the speed of sound c is around 1500 m/s. Therefore the range of wave length $\lambda = c/f$ covered is about 0.1-1 mm. For suspensions comprised of micro particles, λ is normally at least one order of magnitude larger than the particle diameter, so scattering is relatively weak. The absorption is still there, though,

---

[1] Here "couple" means that the acoustic impedance is matched. Details see Section 2.6

especially in highly viscous fluids such as dense suspensions. Higher frequency leads to finer spatial resolution but stronger absorption, thus it shortens the range of view into the material. Resolution beyond the diffraction limit can be achieved [68], but the temporal resolution has to be sacrificed to accumulate data for statistics. Depending on the purpose of the observation, we need to find a balance between temporal resolution, spacial resolution, and penetration depth.

For suspensions, there are three important length scales: the surface interaction is at nanometer or sub-nanometer scales, the particle diameter is around 10 μm, and the characteristic length scale in the transient shear flow is of order 1 mm. Even with the ultra-fast ultrasound localization microscopy (uULM) technique (a few μm resolution) [68], it is still difficult to visualize individual particles. Luckily, sometimes to model a system, we only need to choose the "appropriate" length scale, and do not need to have a complete understanding of the details at smaller scales [69]. As will be discussed later, models can be developed treating suspensions as a continuum. Experimentally, this allows us to push the limit of temporal resolution and penetration depth while we only aim for "reasonable" spatial resolution. This is where ultrasound imaging can really help.

2.2 Introduction to the ultrasound system

The apparatus we used for the experiments described in this thesis was a Verasonics Vantage 128 research ultrasound platform, which is shown in Fig. 2.1(a). It has three main parts: the data acquisition hardware, the host controller computer, and an ultrasound transducer. The data acquisition hardware has 128 independent channels that control and communicate with the ultrasound transducer. Transducers are made of piezoelectric materials that transform pressure signals into electric signals, and vice versa. Our ultrasound system can work with linear array, curved array, or phased array transducers. We primarily used a Philips L7-4 linear array transducer, which has a flat surface as schematically illustrated in Fig. 2.1(b).

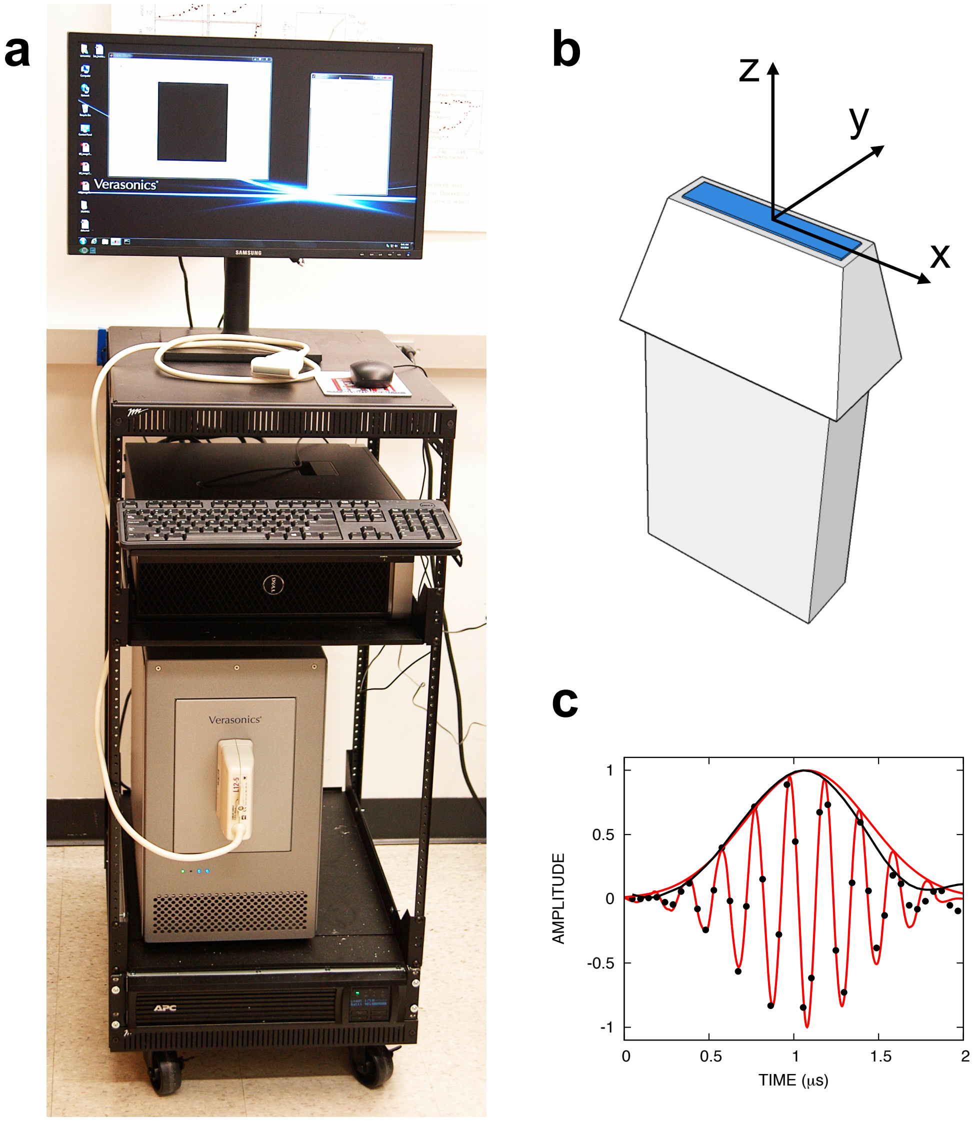

Figure 2.1: Introduction to the ultrasound system. (a) Photo of the Verasonics Vantage 128 system with a Philips L7-4 transducer connected. (b) A schemaitc illustration of an L7-4 transducer, with the conventional coordinate system for transducers labelled. (c) An examplary transmitted signal. The red curves show the functional form of the signal and its Gaussian envelope. The black dots show the measured transmitted signal reflected from a surface parallel to the $x-y$ plane. The black line is the envelope of the reflected signal. The amplitude of the signals are normalized by the peak heights of the envelopes.

Its working part is comprised of a one dimensional linear array of 128 elements. The width of each element in x direction is 0.250 mm and the distance between the centers of adjacent elements is 0.298 mm. In the y direction, the elements have a width of about 7mm, but the beam is focused, so the transducer only scans a thin sheet in the x-z plane.

A transducer can be used as an ultrasound transmitter, receiver, or both (transceiver). Each element in the array can transmit or receive ultrasound signals independently. The shape, duration, frequency, and other parameters of the transmitted signal are all adjustable according to the specific application. Our most commonly used transmitted signal is a $f = 5.00$ MHz sinusoidal wave with the amplitude modulated by a Gaussian envelope, as shown in Fig. 2.1(c). When all the elements transmit the same signal simultaneously, we get a plane wave that propagates in the z direction. By controlling the relative transmission time of each element, we can also realize tilted plane waves, beam sweeping, or focused beam.

After sending out the signal, the transducer is switched to the receiving mode. For $f = 5$ MHz signals, we set the center frequency of data acquisition f_c to be 5.208 MHz. The actual sampling frequency is $4 \times f_\mathrm{c} = 20.832$ MHz, so the system acquires a bit more than 4 data points in one period of the transmitted signal. The bandwidth of the L7-4 transducer is $4 \sim 7$ MHz. The original acquired signal is called the radio frequency (RF) data, which is a time series of the amplitude of the echo signals. Each ultrasound element provides one such series, so with all 128 elements, we obtain an $N_\mathrm{RF} \times 128$ matrix, where N_RF is the number of acquisitions, based on the maximum depth z_max required for the images:

$$N_\mathrm{RF} \geq \frac{z_\mathrm{max}}{c} \cdot 4 f_\mathrm{c} \cdot 2, \tag{2.1}$$

where c is the speed of sound, $4f_\mathrm{c}$ is the data acquisition rate, and the factor 2 is because of the round trip of the signal. For image reconstruction, the RF data are transformed into in-phase and quadrature (IQ) components. Then two-dimensional brightness mode (B-mode) images can be reconstructed based on the IQ data. In the experiments, we can choose to use the RF data, the IQ data, or the B-mode images depending on the purpose of the measurement. The data acquisition module can take RF data at a very high rate, and save the data in the local memory. Transferring data to the host computer takes more time, and the slowest process is image reconstruction. The highest frame rate can be obtained by taking RF data consecutively, then transferring and processing the data afterwards. The image depth z_{max} is also a limiting factor. Time between two frames should not be shorter than $2z_{\text{max}}/c$ to make sure the echoes are from one transmitted signal only. The maximum frame rate we used for imaging when all 128 elements were active was $10,000$ frames per second. It can be even faster if the imaging window is shrunk.

2.3 Speed of sound measurements

The speed of sound c (phase speed of the compression wave) in a homogeneous and isotropic fluid is

$$c = \sqrt{\frac{1}{\kappa\rho}} = \sqrt{\frac{K}{\rho}}, \tag{2.2}$$

where ρ is the density, κ is the compressibility, and $K = 1/\kappa$ is the bulk modulus [67]. For a solid the speed of sound depends on the shear modulus G as well

$$c = \sqrt{\frac{K + \frac{4}{3}G}{\rho}}. \tag{2.3}$$

So for liquids and soft solids ($G \ll K$), a speed of sound measurement is a good way to obtain their bulk modulus.

For a dilute suspension of solid non-porous particles in liquids, Eq. 2.2 still applies, but ρ and κ should be replaced by the effective density ρ_{eff} and the mean compressibility $\bar{\kappa}$, respectively. In the limit where the ultrasound wave length is much larger than the particle

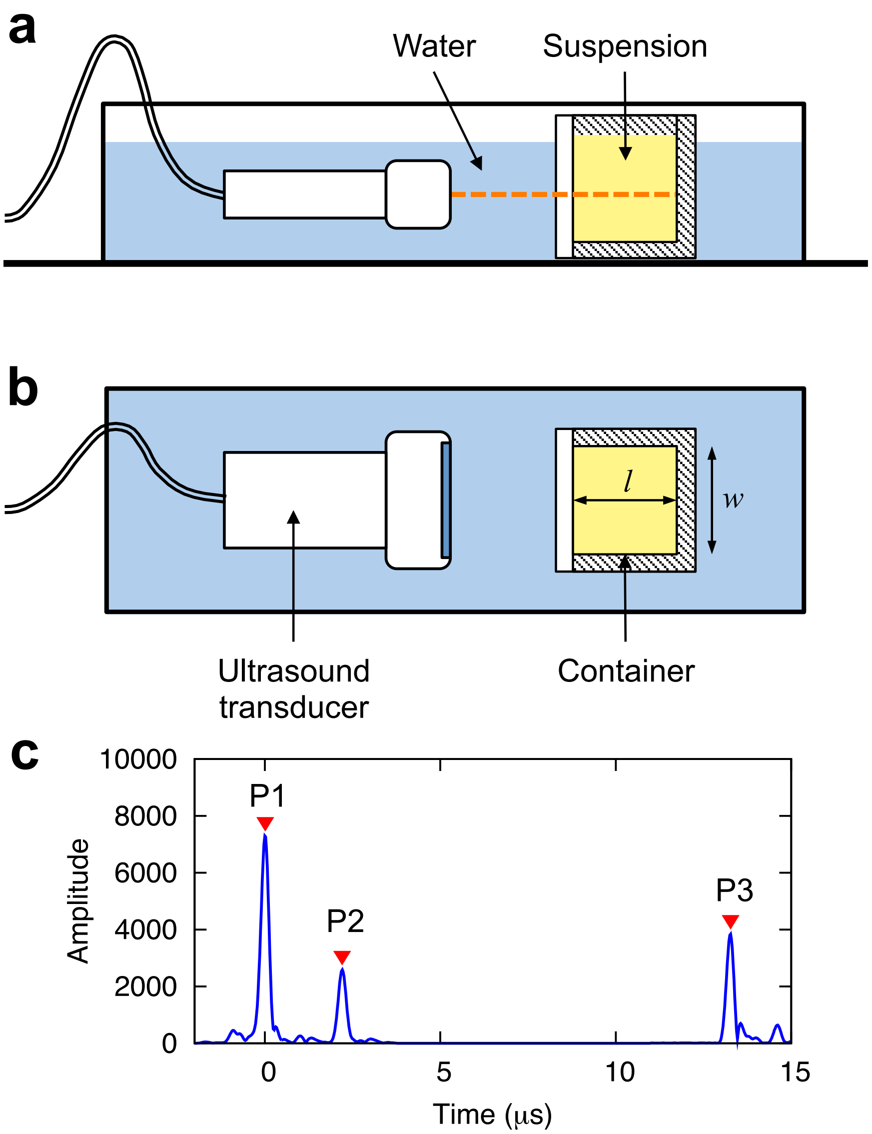

Figure 2.2: Experimental setup for measuring the speed of sound: (a) side view, (b) top view. The ultrasound transducer was submerged in water and it scanned a horizontal slice as represented by the dashed orange line. Liquid or soft solid samples were placed in a rectangular container. Shaded walls of the container were made of aluminum and the white wall was acrylic. To show it more clearly, we plot the container in cross-section in panel (a). (c) Envelope of an exemplary received RF signal. The three peaks labeled are reflections from the water-acrylic interface (P1), the acrylic-sample interface (P2), and the sample-aluminum interface (P3), respectively.

size, the average density and compressibility of the suspension can be expressed as

$$\begin{aligned}\bar{\rho} &= \phi\rho_{\mathrm{s}} + (1-\phi)\rho_{\mathrm{l}},\\ \bar{\kappa} &= \phi\kappa_{\mathrm{s}} + (1-\phi)\kappa_{\mathrm{l}},\end{aligned} \tag{2.4}$$

where ϕ is the volume fraction, and the subscripts "s" and "l" represent solid and liquid, respectively. For density-matched suspensions, meaning that the particles and the liquid have the same density, the effective density equals the mean density [70, 71]: $\rho_{\mathrm{eff}} = \bar{\rho}$. However, if the suspension is not density-matched, a correction ρ_{δ} has to be made: $\rho_{\mathrm{eff}} = \bar{\rho} + \rho_{\delta}$. The detailed form of ρ_{δ} is introduced in Appendix A. According to Eq. 2.2 and Eq. 2.4, by measuring c, we can calculate the compressibility of the suspending particles κ_{s} if we know ϕ, or measure ϕ if we know κ_{s}. For porous micro particles, we can even use this method to measure their porosity, as will be discussed in Section 2.4

The experimental setup for the speed of sound measurements is illustrated schematically in Fig. 2.2. The suspension samples were placed in a rectangular container with four aluminum walls and one acrylic wall. The length and width of the container were $l = 16.4$ mm and $w = 29.0$ mm as labeled in the figure. The thickness of the acrylic was 6.1 mm. The transducer was adjusted so the ultrasound beam was horizontal and perpendicular to the acrylic surface of the container. The ultrasound signal was a pulse of a sinusoidal wave at $f = 5$ MHz, modulated with a Gaussian profile, as shown in Fig. 2.1(c). After being emitted from the transducer, the sound wave travels through water toward the front (acrylic) wall of the container, passes through this wall and then through the suspension until it hits the back (aluminum) wall of the container. In this configuration the wave is reflected from three interfaces: the water-acrylic interface, the acrylic-suspension interface, and the suspension-metal interface. Consequently, in the time series of the received signal, there are three main peaks. The time between the second and the third peak is the round-trip travel time τ of sound in the suspension. For fixed container geometry, the speed of sound then is inversely proportional to the measured time τ in different suspension samples. Here we use the speed of sound in water as a reference, thus

$$c_{\text{sample}} = \frac{\tau_{\text{water}}}{\tau_{\text{sample}}} c_{\text{water}}. \tag{2.5}$$

The temperature of the water in the tank was kept at $20.8 \pm 0.4°\text{C}$, which was also the temperature of the suspension samples in the experiments. The speed of sound in pure water at this temperature is $c_{\text{water}} = 1484.8 \pm 1.2$ m/s [72, 73]. Calibration with deionized water gave $\tau_{\text{water}} = 22.127 \pm 0.007$ μs from 13 independent measurements.

2.4 Measurement of porosity and bulk modulus of micro-particles in liquids[2]

A key parameter describing behaviors of suspensions is the volume fraction ϕ of the solid particles that are dispersed in the liquid. Obtaining accurate values for ϕ becomes difficult for porous particles, because they can absorb some of the liquid. A prime example is the widely used cornstarch suspensions. Starch granules are mostly comprised of amylose and amylopectin, which are hydrophilic polymers [74]. They tend to form a layered structure with concentric growth rings [75] and small voids between adjacent lamellae [74]. When immersed in an aqueous solvent, starch particles will absorb some of the solvent [76, 77], which makes it difficult to ascertain the correct value for the particle volume fraction in the suspension.

As far as their rheological behavior is concerned, what matters is the effective volume occupied by the particles. For any given particle, this is the space enclosed by the surface that can come in contact with neighboring particles. Therefore, the volume of small pores or hollow regions inside a particle still counts toward the particle volume, and the result is larger

---

[2] This section is based on Endao Han, Nigel Van Ha, and Heinrich M. Jaeger. Measuring the porosity and compressibility of liquid-suspended porous particles using ultrasound. Soft Matter, 13(19):3506-3513, 2017.

than the volume calculated from the particle mass and the density of the particle material. Given the difficulty of reliably extracting the particle porosity in systems like cornstarch, there has been no general, agreed-upon method for calculating the volume fraction. Typically the volume corresponding to the mass of the dry particles divided by their material density is used instead. According to different papers, a cornstarch suspension loses the ability to flow (or is reported as "hard to handle") when this dry-material-based volume fraction reaches 0.42-0.45 [78, 53, 51]. This value is considerably lower than the packing fraction at which glass spheres exhibit strongly non-Newtonian effects such as discontinuous shear thickening (~ 0.58) [79], or the random close packing of mono-disperse spheres (0.64). Even taking the poly-dispersity [3], non-sphericity, and surface roughness of cornstarch particles into consideration, this discrepancy is still too large. To compare cornstarch suspensions with other particulate suspensions, dry granular systems [5, 24, 78] or theoretical calculations [36, 41], it is therefore essential to find accurate volume packing fractions by accounting for the particle porosity. Here we describe an approach that achieves this using ultrasound.

If the particles have porosity ψ [4] and the pores become filled with solvent once the particles are suspended, then the volume fraction of saturated particles ϕ is

$$\phi = \frac{1}{1-\psi}\phi_{\mathrm{M}}, \tag{2.6}$$

where ϕ_{M} is given by Eq. B1. By plugging Eqs. 2.4 and 2.6 into Eq. 2.2 and rearranging terms, we find

$$\frac{1}{1-\psi}(\kappa_{\mathrm{s}} - \kappa_{\mathrm{l}})\phi_{\mathrm{M}} + \kappa_{\mathrm{l}} = \frac{1}{c^2\rho_{\mathrm{eff}}}. \tag{2.7}$$

Here c can be directly measured, and ρ_{eff} can be obtained by plugging experimentally obtained parameters into Eq. A2. This is the central equation for the experiments described

---

[3] Usually poly-dispersity tends to increase the packing fraction because smaller particles can fill the gaps between larger particles.

[4] Here we define the particle porosity as the ratio between the pore volume and the total volume enclosed by the particle surface.

here. For suspensions in the same solvent (thus the same κ_{l}), $\frac{1}{c^2\rho_{\mathrm{eff}}}$ is a linear function of ϕ_{M}. The slope of the line is $S_\kappa = \frac{1}{1-\psi}(\kappa_{\mathrm{s}} - \kappa_{\mathrm{l}})$, which is a function of the solvent compressibility κ_{l}.

The mean compressibility of the saturated porous particles κ_{s} is a function of κ_{l} as well. We use Gassmann's equation [80, 81, 82] to calculate $\kappa_{\mathrm{s}}(\kappa_{\mathrm{l}})$:

$$\kappa_{\mathrm{s}}(\kappa_{\mathrm{l}}) = \kappa_0 + \left(\frac{1}{\kappa_{\mathrm{d}} - \kappa_0} + \frac{1}{\psi}\frac{1}{\kappa_{\mathrm{l}} - \kappa_0}\right)^{-1}, \tag{2.8}$$

where κ_0 is the compressibility of the solid material by itself, κ_{d} is the compressibility of the dry particles including all the pores, and ψ is the porosity [5]. Thus the complete expression for the slope S_κ is

$$S_\kappa = \frac{1}{1-\psi}\left[\kappa_0 - \kappa_{\mathrm{l}} + \left(\frac{1}{\kappa_{\mathrm{d}} - \kappa_0} + \frac{1}{\psi}\frac{1}{\kappa_{\mathrm{l}} - \kappa_0}\right)^{-1}\right]. \tag{2.9}$$

When particles are non-porous, we have $\psi = 0$, $\kappa_0 = \kappa_{\mathrm{d}} = \kappa_{\mathrm{s}}$, and thus $S_\kappa = \kappa_0 - \kappa_{\mathrm{l}}$. This means S_κ is a linear function of κ_{l} with a slope of -1. If the particles are porous but have a much smaller compressibility than the liquid ($\kappa_0 \ll \kappa_{\mathrm{l}}$ and $\kappa_{\mathrm{d}} \ll \kappa_{\mathrm{l}}$), then $S_\kappa \to \frac{1}{1-\psi}(\kappa_{\mathrm{d}} - \kappa_{\mathrm{l}})$. The slope of the S_κ-κ_{l} curve becomes $-1/(1-\psi)$ as $\kappa_{\mathrm{d}}/\kappa_{\mathrm{l}} \to 0$. As κ_{l} decreases and approaches κ_0, the function $S_\kappa(\kappa_{\mathrm{l}})$ deviates from the line $\frac{1}{1-\psi}(\kappa_{\mathrm{d}} - \kappa_{\mathrm{l}})$ and approaches $\kappa_0 - \kappa_{\mathrm{l}}$. This means that by performing experiments with different solvents, and therefore different κ_{l}, we can obtain all three parameters ψ, κ_0, and κ_{d} from fitting the S_κ-κ_{l} data with Eq. 2.9. Note that we assume ψ, κ_0 and κ_{d} of the particles do not vary with the different solvents we used.

To find the porosity and compressibility of cornstarch particles experimentally, we measured the speed of sound c in dilute suspensions with various solvents. For each suspension,

---

[5] Gassmann's equation applies in the "low frequency limit" where there is enough time for the pore pressure to equilibrate[83, 84]. This is reasonable for our experiments, because for cornstarch particles of $\sim 10\ \mu$m size and reasonable permeability, the time it takes for the Biot wave to diffuse through the whole particle is sufficiently short.

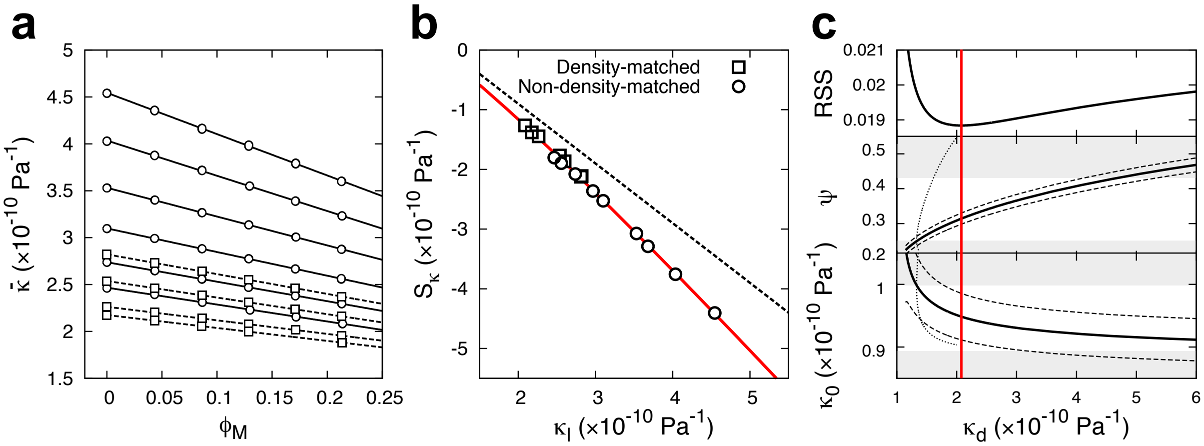

Figure 2.3: Measuring the porosity and compressibility of micro particles in liquids using the speed of sound. (a) Linear relations between the mean compressibility $\bar{\kappa} = 1/(c^2\rho_{\mathrm{eff}})$ and the material volume fraction ϕ_{M} for cornstarch suspensions in different aqueous solvents. Solid and dashed lines are the best fits of non-density-matched (circles) and density-matched (squares) samples, respectively. (b) Slopes S_κ of the lines in (a) as functions of κ_{l}. The solid red line shows the best fit using Eq. 2.9. The black dashed line shows slope -1 . (c) Uncertainty of the fitting parameters κ_{d}, κ_0, and ψ. RSS is the residual sum of squares. The solid red line goes through its minimum at $\kappa_{\mathrm{d}} = 2.08 \times 10^{-10}$ Pa^{-1}. (b) Porosity ψ as a function of κ_{d}. In the lower two panels the solid black lines show the best fits, and the dashed black lines label the region of 95% confidence. The dotted black lines show the boundaries based on Eq. 2.10. The white central areas bound by the horizontal gray regions indicate the range of ψ or κ_0 plus or minus one standard deviation.

we measured the masses of cornstarch m_{cs} and solvent m_{l}, then calculated ϕ_{M} with Eq. B1 and $\bar{\rho}$ with Eq. B2. We performed experiments with both density matched and non-density matched suspensions. For the non-density matched cases, the effective density ρ_{eff} was calculated using Ament (1953) [85] (Eq. A2).

As shown in Fig. 2.3(a), the mean compressibilities of the suspensions $\bar{\kappa} = 1/(c^2\rho_{\text{eff}})$ were indeed linear functions of ϕ_{M} for both density-matched (squares) and non-matched (circles) suspensions, as predicted by Eq. 2.7. The solvents for non-density matched samples were mixtures of glycerol and deionized water at different mass ratios. In Fig. 2.3(a), from top to bottom, the mass ratio of glycerol was 0%, 15%, 30%, 45%, 60% and 75%. In the density-matched experiments we adjusted the density of the glycerol water mixtures to 1.63×10^3 kg/m^3 by adding an appropriate amount of CsCl. From top to bottom the mass ratio of glycerol over the sum of glycerol and water was 0%, 25%, 50% and 60%. It can be seen that the compressibility of the solvent was greatly reduced when CsCl was added. From linear regression, we obtained the slopes of the lines S_κ.

The relation between S_κ and the solvent compressibility κ_{l} is shown in Fig. 2.3(b). We fit all data with Eq. 2.9 and obtain the three fitting parameters: $\psi = 0.31 \pm 0.12$, $\kappa_0 = (0.95 \pm 0.06) \times 10^{-10}$ Pa^{-1}, and $\kappa_{\text{d}} = (2.1 \pm 1.7) \times 10^{-10}$ Pa^{-1}. Since the bulk modulus of a dry porous material decreases with porosity [86, 87], its compressibility κ_{d} satisfies

$$\kappa_{\text{d}} > \frac{1}{1-\psi}\kappa_0. \tag{2.10}$$

With this condition, we can narrow down the possible range of the parameters as shown in Fig. 2.3(c). We varied κ_{d} from 1×10^{-10} Pa^{-1} to 6×10^{-10} Pa^{-1} and fitted the experimental results in Fig. 2.3(b) with the other two parameters ψ and κ_0 at each κ_{d}. From the residual sum of squares (RSS) we find that the best fit is obtained at $\kappa_{\text{d}} = 2.1 \times 10^{-10}$ Pa^{-1}. The boundary given by Eq. 2.10 is shown with dotted lines in Fig. 2.3(c). Possible values for κ_{d} lie on the right hand side of the dotted lines. Therefore, the lower limit of ψ becomes 0.25,

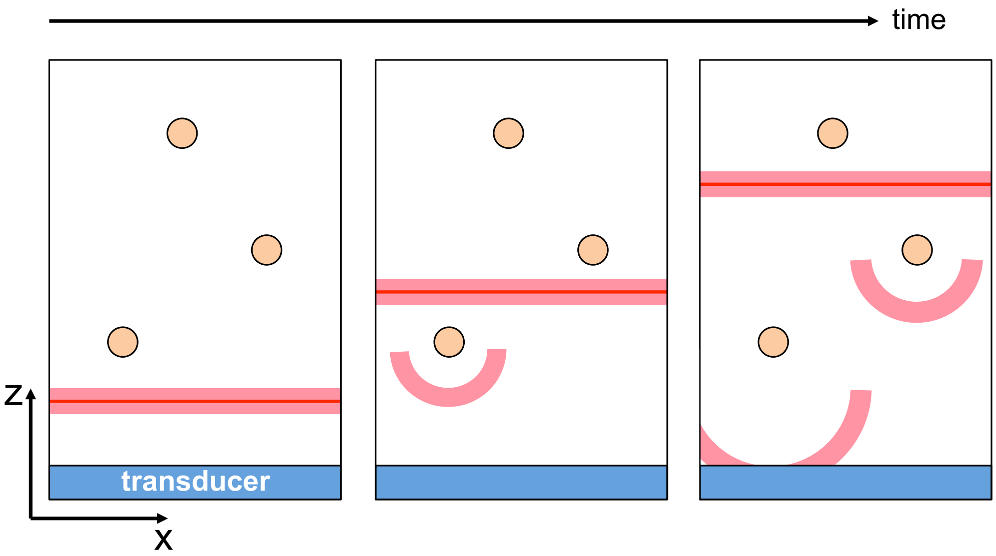

Figure 2.4: Illustration of how ultrasound reflects back from scatterers. The scatterers are represented by the orange disks, the head of the transducer is the blue rectangle, and the ultrasound wave pulses are represented by the red bands.

and the upper limit of κ_0 becomes 1.0×10^{-10} Pa^{-1}. From this we obtain the porosity $\psi = 0.31^{+0.12}_{-0.06}$, the material compressibility $\kappa_0 = 0.95^{+0.05}_{-0.06} \times 10^{-10}$ Pa^{-1} and the compressibility of the dry particles $\kappa_\mathrm{d} = 2.1^{+1.7}_{-0.8} \times 10^{-10}$ Pa^{-1}.

The uncertainty associated with these fits will be further reduced if the range (especially the upper limit) of the compressibility κ_d for the dry particles can be constrained, e.g. by independent measurements. Waitukaitis [88] used indentation by atomic force microscopy (AFM) to extract Young's modulus E_cs of dry cornstarch granules, and found $E_\mathrm{cs} \approx 5$ GPa. The Poisson's ratio of dry cornstarch particles ν_d is not well known, but for most polymers the Poisson's ratio is greater than 0.25 [89]. Assuming $\nu_\mathrm{d} > 0.25$, we can use the relation $\kappa_\mathrm{d} = 3(1 - 2\nu_\mathrm{d})/E_\mathrm{cs}$ to obtain $\kappa_\mathrm{d} < 3.0 \times 10^{-10}$ Pa^{-1}. This leads to $\kappa_\mathrm{d} = 2.1^{+0.9}_{-0.8} \times 10^{-10}$ Pa^{-1} and $\psi = 0.31^{+0.06}_{-0.06}$.

2.5 Ultrasound imaging

One of the most powerful functions of ultrasound is imaging the interior of optically opaque materials. Essentially, what the ultrasound system measures is the time of flight of the sound wave. The reconstruction process of B-mode images is basically transforming the time information to position information. A schematic illustration of one data acquisition event is shown in Fig. 2.4. A plane wave of the signal shown in Fig. 2.1(c) is transmitted by the transducer and propagates along the z direction. When the plane wave interacts with a scatterer, it will be reflected back to the transducer, but the scattered echo has a curved wave front. By comparing the phase difference of the detected signals between adjacent piezoelectric elements, we can find the x position of the scatter. And by measuring the time of flight, we can find the z position of the scatterer given the speed of sound in the surrounding medium. As a result, to reconstruct images correctly, firstly we need to measure the speed of sound in the tested material as introduced in Section 2.3.

With the ability to measure the positions of scatterers, ultrasound allows us to track the motion of the material in which the scatters are embedded by applying particle image velocimetry (PIV) to the reconstructed images. To check the reliability of this method, we measured the velocity field in a gelatin block with embedded particles under simple shear. As illustrated in Figure 2.5(a), the gelatin sample was a cuboid made of 10% (w/w) gelatin in water, with a layer of glass spheres uniformly distributed in the middle of the sample. The experimental setup is sketched in Fig. 2.5(b). The gelatin block was placed vertically (meaning the particle layer is vertical) on a 5/64 inch thick acrylic board and sheared by a plane that can slide horizontally on the top. An L12-5 (50 mm wide) transducer ($f = f_{\mathrm{c}} = 8.93$ MHz) was placed below the acrylic board, and the imaging plane (x-z plane in Fig. 2.1(b)) was aligned with the layer of particles in the sample. Since gelatin is optically transparent, we observed the motion of the particles simultaneously with a high-speed camera (Phantom V9), at a spatial resolution of 65.6 μm/pixel. In this way, the ultrasound images could be directly compared with the optical images.

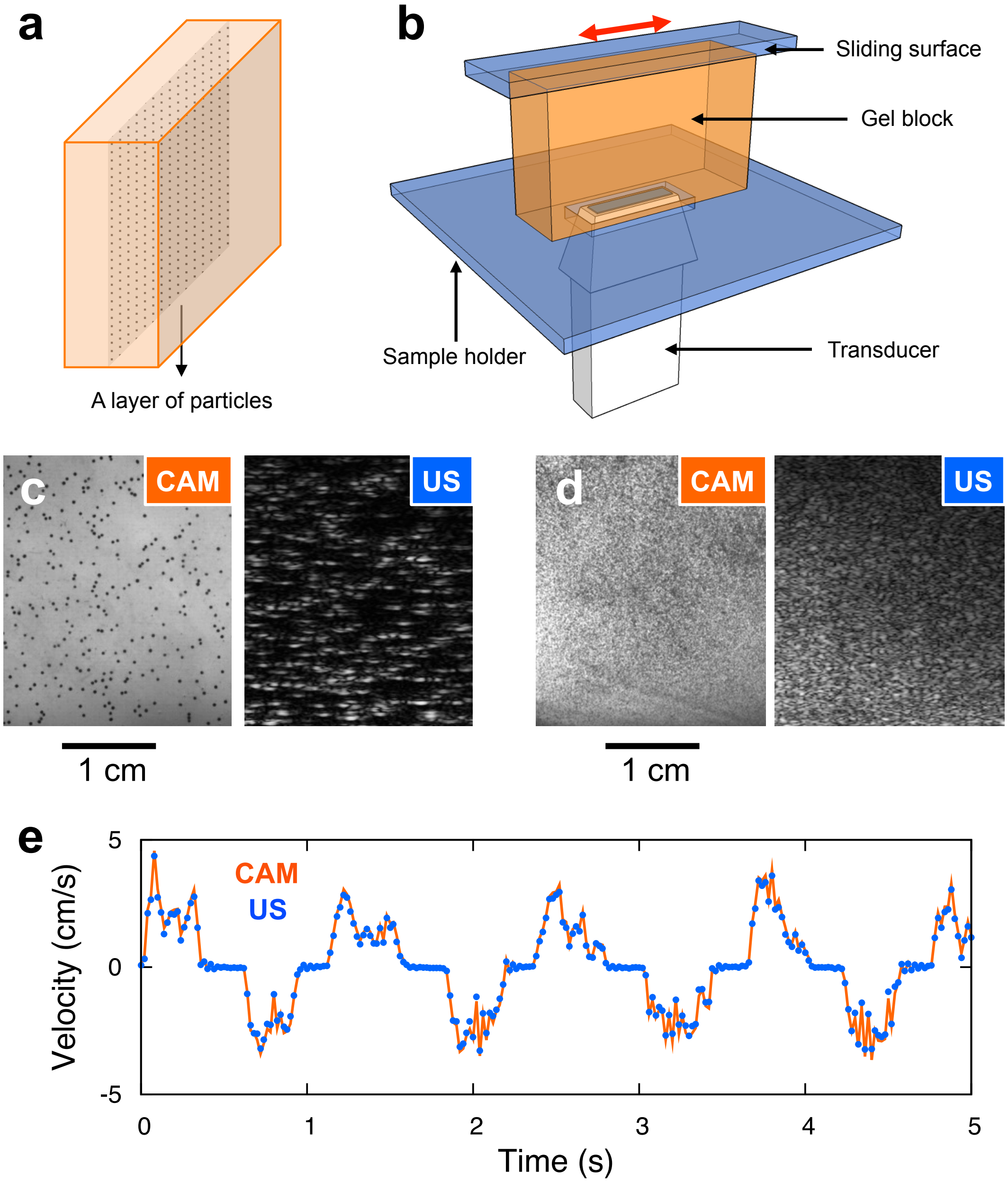

Figure 2.5: (a) Gelatin block with a layer of embedded glass particles. (b) Experimental setup. The slider on the top can move horizontally. (c) Comparison between camera (CAM) image and ultrasound B-mode image (US) for 300-400 μm ($\approx 2\lambda$) particles. (d) Comparison for 45-63 μm ($\approx 0.3\lambda$) particles. (e) Horizontal velocity as a function of time obtained from the camera (orange) and the ultrasound (blue) at the same height, for the sample in (d).

We tried spherical scatterers with two different diameters: $d = 300\text{-}400\ \mu\text{m}$ ($\approx 2\lambda$) and $d = 45\text{-}63\ \mu\text{m}$ ($\approx 0.3\lambda$), where $\lambda \approx 0.17$ mm is the wavelength. The spatial resolution of the reconstructed images is limited by the wavelength - only objects with a length scale greater than λ can be resolved. As shown in Fig. 2.5(c & d), the positions of individual particles were captured in the ultrasound images when $d \approx 2\lambda$, but we can only see a speckle pattern that does not have a one-to-one correspondence with the real particle positions when $d \approx 0.3\lambda$. However, in both cases the motion of the speckle pattern can represent the motion of the materials.

To test the correlation between the speckle motion and the material motion, we moved the sliding surface back and forth horizontally by hand, and took consecutive images with camera and ultrasound simultaneously. We performed PIV analysis with both optical and ultrasound images. Each image was divided into square elements and the velocity of each element is calculated through a cross-correlation algorithm between two subsequent frames. As expected for an elastic solid, the local horizontal velocities increase linearly with the height, and the two independent measurements showed excellent agreement, for both large and small scatters. An exemplary result is shown in Fig. 2.5(e), which compares horizontal velocities as a function of time measured by the two methods at a certain height of the sample with $d \approx 0.3\lambda$ spheres. Since the sample was sheared by hand in a random manner, there were many fine details in its motion. Nevertheless, the ultrasound measurements captured all the details in the changing velocity.

2.6 Visualizing flows of dense suspensions

When sound wave propagates from one medium into another, reflection happens at the interface. The intensity reflection coefficient R_I is defined as the ratio between the intensity

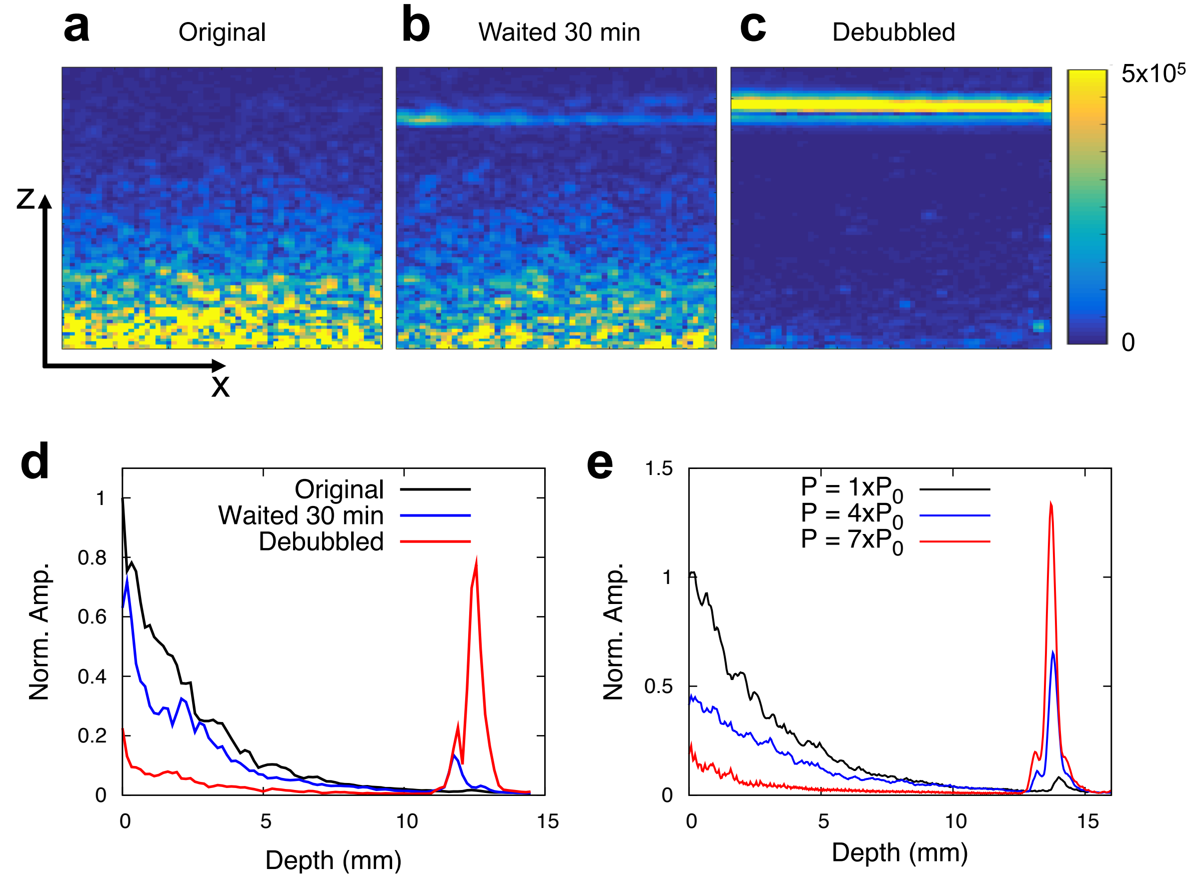

Figure 2.6: Effect of air bubbles in ultrasound imaging of dense suspensions. (a-c) Ultrasound B-mode images of dense cornstarch suspensions in a 10 ml syringe. The transducer is at the bottom of these images. (d) Amplitude of RF signals in suspensions with different air concentration. (e) Amplitude of RF signals in suspensions under different pressure.

magnitudes of the reflected wave and the incident wave. For normal incidence, we have

$$R_I = \left(\frac{Z_2 - Z_1}{Z_2 + Z_1} \right)^2 , \tag{2.11}$$

where $Z = \rho c$ is the acoustic impedance, and 1, 2 represent the media on each side of the interface. The corresponding intensity transmission coefficient for normal incidence is $T_I = 1 - R_I$. The acoustic impedance of some materials are listed in Table 2.1.

As Table 2.1 shows, air has a very different impedance compared to water or cornstarch suspensions. As a result, when there are air bubbles in the suspensions, we receive strongly scattered signals. After preparing a dense cornstarch suspension, we immediately transferred it into a 10 ml syringe, sealed the nozzle, and observed with ultrasound by pushing the transducer against the wall of the syringe. The B-mode image is shown in Fig. 2.6(a). We saw very strong signals close to the transducer, and the sound wave did not penetrate deeply. We then left the suspension rest for 30 minutes, and observed with ultrasound again, as shown in Fig. 2.6(b). Now the system became more transparent, and we can see the wall of the syringe on the opposite side, but there was still strong scattering in the suspension. Lastly, we debubbled the suspension by pulling the plunger of the syringe to create a low pressure inside. The size of the bubbles expanded and by tapping the syringe, we got rid of most of the bubbles visible by the ultrasound as shown in Fig. 2.6(c). A strong reflection

Material	c (m s^{-1})	ρ (kg m^{-3})	Z (kg m^{-2} s^{-1})
Air	340	1.20	408
Water	1480	1000	1.48×10^6
Density-matched solvent	1630	1647	2.68×10^6
Cornstarch suspension	1630	1939	3.16×10^6
VoroWhite plastics	2412	1210	2.92×10^6
Acrylic	2744	1180	3.24×10^6

Table 2.1: Speed of sound c, density ρ, and acoustic impedance Z in some materials at room temperature (20°C). The density-matched solvent was a mixture of 44.3% CsCl, 27.8% glycerol, and 27.8% water by mass. The Cornstarch suspension was prepared with the solvent above at packing fraction $\phi = 0.48$.

is seen from the opposite wall. We average the corresponding RF data of the three images along the x direction, and plot the averaged signal amplitudes as functions of the depth z in Fig. 2.6(c). From the plot we can see the much reduced scattering, and much stronger transmission signal reflected from the opposite wall at $z \approx 13$ mm.

A similar effect can be obtained by pressurizing the suspension. We kept the plunger sealed, and pushed its plunger with an Instron material tester. The results are plotted in Fig. 2.6(e), which can be directly compared to (d). Again, we can see that the amplitude of the signals in the sample decreased when the applied pressure increased from P_0 to $7 \times P_0$ (P_0 is the atmospheric pressure). The amplitude of the signal reflected from the opposite wall increased with pressure, which confirmed that the decrease of brightness in the bulk was not because of an increased energy dissipation (attenuation), but less scattering. We think this phenomenon is caused by the decrease in bubble size, and thus of the scattering cross section, at high pressure. Potentially, this method could be used to detect pressure in the suspensions, but much more careful calibration is required.

To track the motion of the suspensions, we need an appropriate speckle density in the B-mode images. A freshly made dense suspension normally has too many bubbles in it, as shown in Fig. 2.7(c). In this case, the penetration depth of the signal is highly limited, and when the suspension moves, the speckle pattern shows deformation as well as translational motion, which makes the tracking more difficult. Thus for ultrasound imaging, we debubbled a suspension first, so that it became almost transparent and featureless as shown in Fig. 2.7(a). Then we added a certain amount of air bubbles back to the suspension by slowly stirring with a spatula. Fig. 2.7(b) shows an example of speckle concentration and contrast that worked well in practice. The speckle pattern in a flowing suspension is demonstrated in Fig. 2.7(d). A vertical slice taken at the same position from a series of B-mode images are stitched next to each other. The speckles move with the flow in the vertical direction, as labelled by the dashed black lines. The slope of each line represents the local vertical velocity of the suspension, which agrees with the results obtained from the PIV analysis.

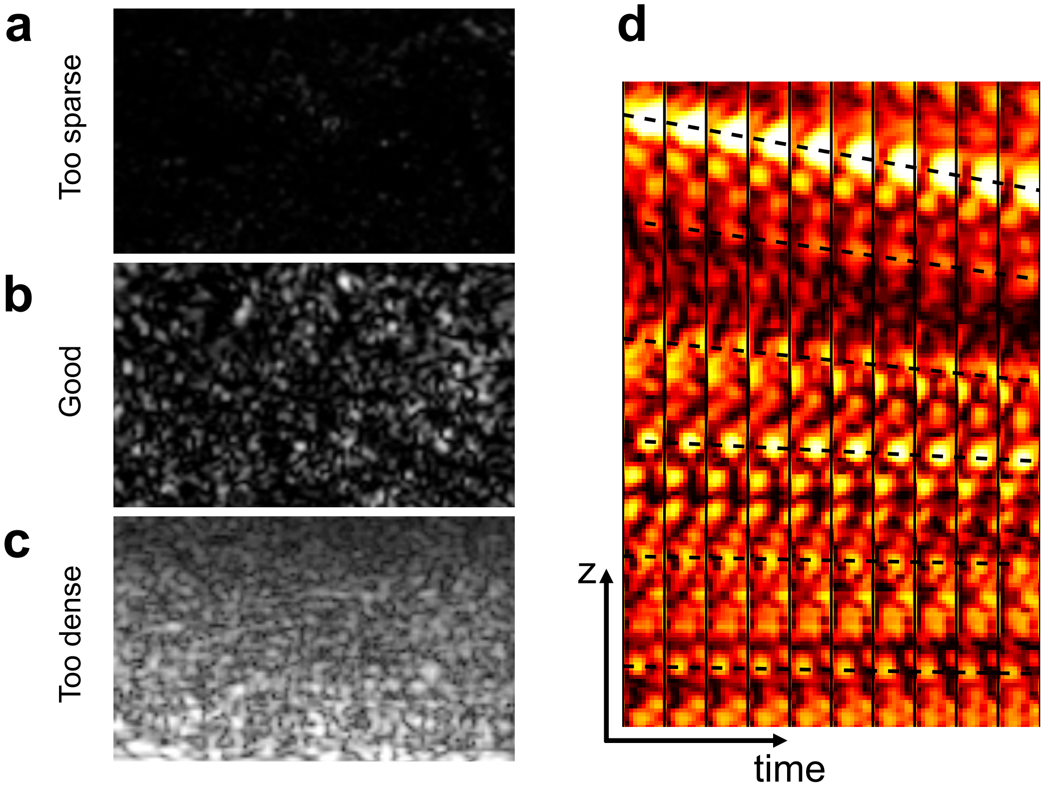

Figure 2.7: Speckle patterns in dense suspensions for tracking. (a-c) Speckle patterns generated by different air bubble concentrations in dense suspensions: (a) too few scatterers; (b) good speckle pattern; (c) too many scatterers. (d) Speckle patters at the same position in a series of B-mode images obtained from exemplary suspension flow.

We checked the effect of air bubbles on the mechanical properties of dense suspensions with steady-state rheology experiments. When the suspension was just made (ultrasound image shown in Fig. 2.6(a)), it had higher viscosity at low shear stress compared to the debubbled suspension, which led to stronger shear thinning. At shear stress above 1 Pa, there was no difference between the two samples from the rheology measurements. For a non-debubbled sample that was tested 30 min after preparation, there was still a significant amount of air bubbles in the suspension as shown in Fig. 2.6(b), but its rheological properties were identical to a fully debubbled suspension across the whole stress range measured. Thus we conclude that adding a small amount of small bubbles as tracers does not affect the mechanical properties of the suspensions.

CHAPTER 3

INVESTIGATING IMPACT-ACTIVATED FRONTS WITH ULTRASOUND[1]

3.1 Introduction

In this Chapter, we focus on understanding the mechanism of impact-activated solidification by applying the ultrasound techniques described in Chapter 2. As introduced in Section 1.4, impact on the suspension surface generates a front that propagates across the system with a speed faster than the impactor speed [52]. This front transforms the suspension from a fluid-like state into a solid-like state. Originally, a model [58] based on jamming by compression and thus densification [26] was proposed to explain this dynamic jamming transition. However, this model has certain limitations. In suspensions the presence of an interstitial liquid makes it possible to prepare three-dimensional systems at packing fractions ϕ well below ϕ_{J} by density matching the particles to the liquid. Given that such systems can still exhibit impact-induced solidification, jamming by densification would imply significant particle packing fraction changes $\Delta\phi = \phi_{\mathrm{J}} - \phi$. However, unless the impact speed is so high that the liquid becomes compressible [90], viscous drag will counteract any densification of the particle sub-phase. This calls into question the mechanism underlying Eq. 1, even though there is experimental evidence for the basic outcome, namely that the ratio between the front speed and the impact speed increases dramatically as $\Delta\phi$ approaches zero [52, 57].

One intriguing alternative mechanism has recently emerged with the concept of jamming by shear [24, 41]. In this extension of frictionless, standard jamming, the presence of frictional interactions between particles makes it possible to start from initially isotropic, unjammed configurations at $\phi < \phi_{\mathrm{J}}$ and, without changing ϕ, rearrange the particles into

---

[1] This Chapter is based on Endao Han, Ivo R. Peters, and Heinrich M. Jaeger, High-speed ultrasound imaging in dense suspensions reveals impact-activated solidification due to dynamic shear jamming. Nature Communications, 7, 12243, 2016.

anisotropic fragile or jammed configurations by applying shear. Shear jamming is also possible in frictionless systems, albeit over a much smaller range in $\Delta\phi$ [27]. So far, such shear jamming has been observed experimentally in two-dimensional (2D) dry granular systems under quasi-static conditions, where there is direct visual access to particle positions and stresses by imaging perpendicular to the 2D plane [24]. Investigating the role of shear jamming in dynamic impact-induced solidification of 3D suspensions requires the capability of non-invasively tracking the jamming fronts and the associated, quickly evolving flow field in the interior of an optically opaque system.

Here we achieve this with ultrasound. Related methods have been applied to studying dry granular materials [63, 64] and steady-state flow in suspensions [91, 92, 61, 62, 93]. Measuring the speed of sound c we obtain an upper bound on the change of packing fraction $\Delta\phi$ as the suspension jams. We find that at $U_\mathrm{p} \ll c$, $\Delta\phi$ is much smaller than required if densification was the primary driver for impact-activated solidification. To investigate the crossover as U_p increases, we use high-speed ultrasound imaging to track the emergence of concentrated shear bands at the location of the propagating jamming fronts. In the regime of slow U_p, the suspension responds to stress like a fluid, and in the regime of fast U_p, the suspension develops solid-like characteristics, which we identify by investigating the flow fields. The invariant packing fraction and existence of shear bands provides direct evidence of dynamic shear jamming in 3D suspensions. Furthermore, access to the full flow field allows us to extract the local shear rates and identify the origin of a key, but so far unexplained, feature of the response to impact: the longitudinal front propagation speed exceeds the transverse propagation speed by a factor very close to two [57].

3.2 Impact experiment and the measured flow field

The experimental setup is illustrated in Fig. 3.1. The ultrasound measurements and imaging were performed with our Verasonics Vantage 128 system. The experiments were performed

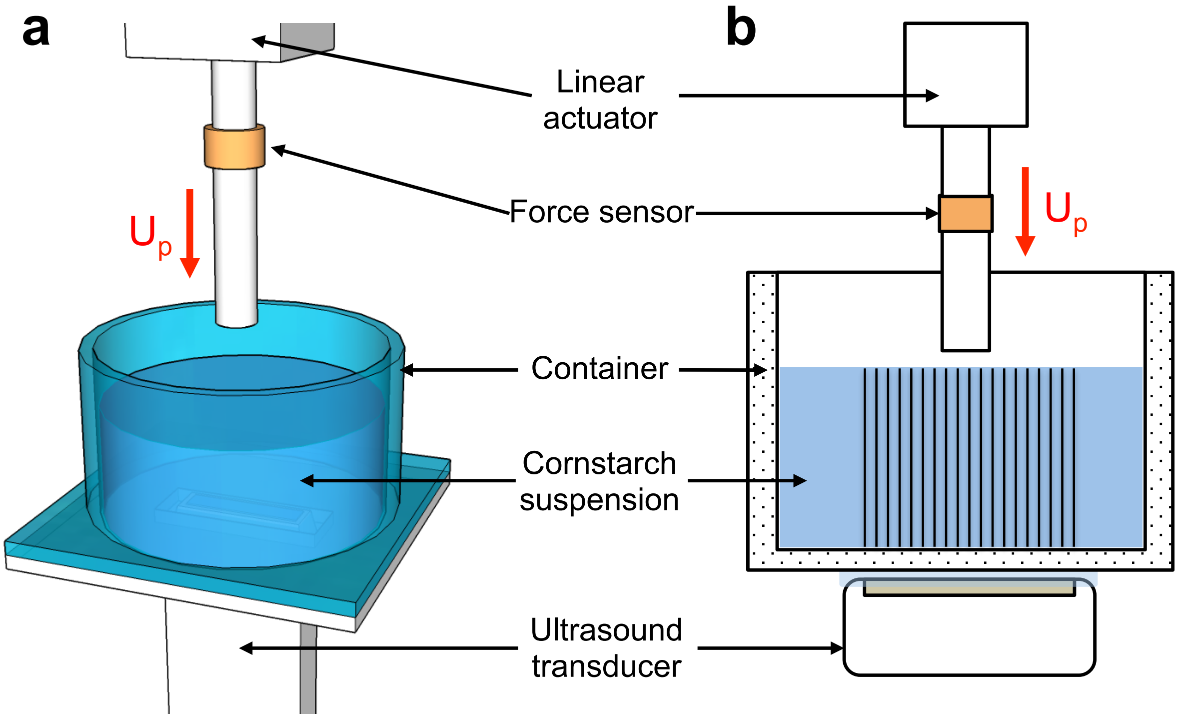

Figure 3.1: Schematic of the experimental setup. (a) shows a 3D sketch of the setup, and (b) shows the 2D cross-section. The sample container and impactor are cylindrical and concentric. The ultrasound transducer scans a vertical slice along the central z-axis, providing a field of view as indicated by the striped area.

with a prototypical suspension: cornstarch particles dispersed in water-glycerol CsCl solutions. To increase the amount of sound energy transmitted into the suspensions, the sample container was made of materials that closely matched the acoustic impedance of the suspensions. According to Table 2.1, we can use either "Vero White Plus" plastic, which is a UV-cured resin, or acrylic. Here the sample container was 3D-printed with Vero White Plus (Objet Geometries Inc.). The inner diameter of the container was 10.0 cm and the typical depth H of the suspension was 2.5 to 3.5 cm. This insured that the front reached the bottom before it interacted with the side wall. The impactor was a cylinder of diameter of 6 mm or 10 mm, driven by a computer controlled linear actuator (SCN5, Dyadic Systems) and equipped with a force sensor (DLC101, Omega). The ultrasound transducer (Philips L7-4; 128 independent elements; total width of 3.8 cm) contacted the bottom of the container through a thin layer of ultrasound gel.

In the impact experiments the impactor was driven vertically downward with constant velocity U_{p}. The ultrasound system was triggered as the impactor approached the surface; images were taken at a frame rate of 10 to 10,000 frames per second, adjusted according to U_{p}. The spatial resolution of the ultrasound was limited by the wavelength, about 0.4mm in our experiments. Once triggered, the ultrasound system made several hundred acquisitions consecutively. In one acquisition each of the 128 transducer elements transmitted the same ultrasonic pulse at the same time and received an individual reflected time series. The pulse was a 5 MHz sinusoidal wave modulated by a Gaussian profile (Gaussian envelope) for a pulse length of 6 periods. From the time series received by the transducer and using the previously measured speed of sound c we reconstructed B-mode images [67] that captured the positions of the tracer particles (air bubbles) in the suspension. By tracking the tracer bubble displacements with a particle imaging velocimetry (PIV) algorithm, we obtained a two-dimensional flow field from within the bulk of the suspension. We verified that the amount of bubbles did not suppress the penetration of the ultrasound in the suspensions and produced a negligible change in the speed of sound. We also determined that the effect of the bubbles on the suspension viscosity was limited (see Section 2.6). Between successive impact experiments the suspension was relaxed by gently shaking and rotating the container.

A representative flow field (u_r, u_z) inside the suspension during an impact is shown in Fig. 3.2(a)-(c). The vertical and horizontal axes in the image correspond to the z and r directions in cylindrical coordinates. The flow field shows a solid-like plug in the center, as evidenced by the fact that all points move vertically with speed close to U_{p}. Also evident is a strong velocity gradient around the periphery of the solid-like region. To show this more explicitly, we calculate the local shear rate from the velocity field (u_r, u_z). Given rotational symmetry, the shear rate tensor becomes

$$\dot{\varepsilon} = \begin{bmatrix} \frac{\partial u_r}{\partial r} & 0 & \frac{1}{2}(\frac{\partial u_r}{\partial z} + \frac{\partial u_z}{\partial r}) \\ 0 & \frac{u_r}{r} & 0 \\ \frac{1}{2}(\frac{\partial u_r}{\partial z} + \frac{\partial u_z}{\partial r}) & 0 & \frac{\partial u_z}{\partial z} \end{bmatrix}. \tag{3.1}$$

Fig. 3.2(d) and (e) show the two components $|\dot{\varepsilon}_{zz}| = -\frac{\partial u_z}{\partial z}$ and $|\dot{\varepsilon}_{rz}| = -\frac{1}{2}(\frac{\partial u_r}{\partial z} + \frac{\partial u_z}{\partial r})$. Underneath the solid-like region, *i.e.*, in longitudinal direction, $\dot{\varepsilon}_{zz}$ dominates. This corresponds to pure shear that compresses the suspension in the z direction and expands it radially. By contrast, along the sides of the jammed plug $\dot{\varepsilon}_{rz}$ dominates, and here the main contribution arises from the term $\frac{\partial u_z}{\partial r}$. As a result, the velocity gradient is mainly perpendicular to U_{p}. This is analogous to simple shear as seen, for example, in parallel plate setups. We will return below to the implications of having both types of shear.

3.3 Invariant packing fraction during front propagation

In an unjammed suspension of solid particles in a Newtonian liquid the shear modulus vanishes. In the limit that the solid particles are much smaller than the wavelength, the speed of sound is then given by $c = (K/\rho)^{\frac{1}{2}}$, where K is the average bulk modulus and

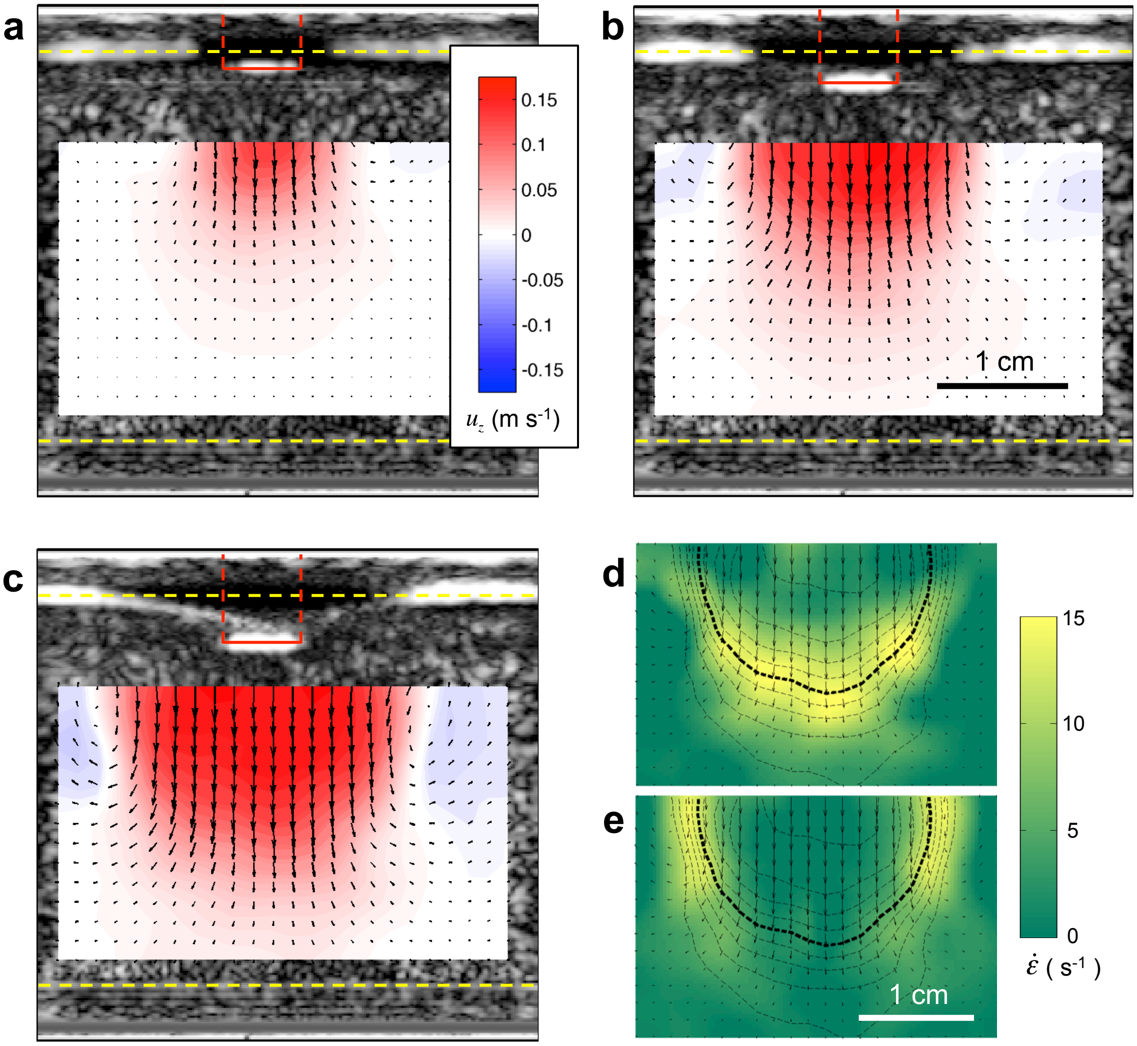

Figure 3.2: Visualization of the flow field with ultrasound. (a)-(c) Velocity field during an impact at time 6.0 ms (a), 13.2 ms (b) and 20.3 ms (c) (the impactor reached the surface at time $t = 0$ ms). The images are B-mode images (shown in gray scale) with overlaid velocity field from PIV analysis. The color code represents the magnitude and sign of the vertical component of the local velocity u_z (red corresponds to downward, blue to upward flow). Dashed yellow lines indicate the locations of the free surface of the suspension and of the bottom of the container. The impactor is outlined in red. The experimental parameters were $\phi = 0.47$, $U_\mathrm{p} = 175$ mm$\cdot$s^{-1}, liquid viscosity $\eta_0 = 4.6 \pm 0.2$ mPa$\cdot$s, fill depth $H = 30$ mm, and impactor diameter of 6.0 mm. The black scale bar in (b) represents 1 cm for (a)-(c). (d),(e) Two components of the shear rate tensor, $|\dot{\varepsilon}_{zz}|$ (d) and $|\dot{\varepsilon}_{rz}|$ (e), shown for the same instant in time as the flow field in (c). Dashed lines are contours connecting points with the same u_z. The thicker line indicates $u_z = U_\mathrm{p}/2$. The white scale bar is 1 cm for (d) and (e).

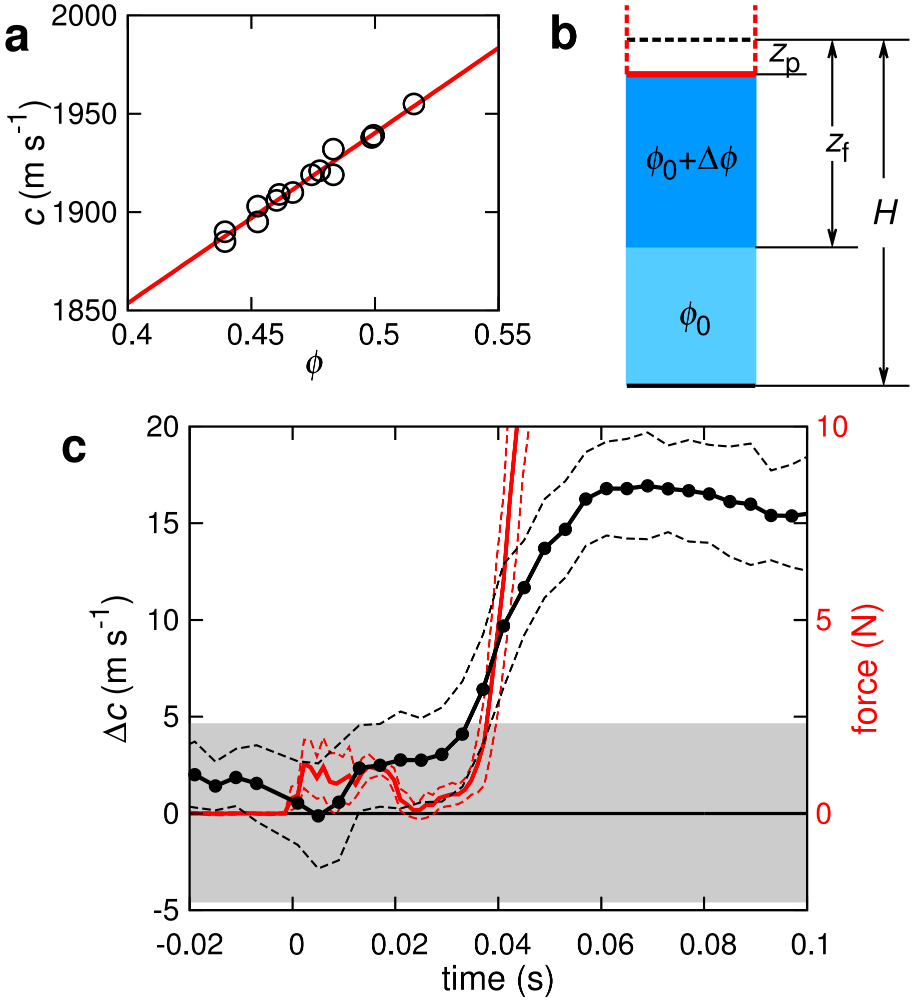

Figure 3.3: Direct measurement of packing fraction changes. (a) Speed of sound c as a function of packing fraction ϕ. All data were taken with suspensions in their quiescent fluid-like state, at packing fractions well below ϕ_J. (b) Sketch of the region beneath the impactor. The black dashed line represents the initial suspension surface at a fill height H above the bottom of the container (bold black solid line). As the impactor (outlined in red) pushes down a vertical distance z_p the front (dark blue region) propagates a distance z_f. (c) Change in sound speed Δc as a function of time (black trace) at $\phi_0 = 0.48$. Impact at the free suspension surface occurs at $t = 0$ ms. Once the front has reached the bottom of the container (at $t \approx 35$ ms), the force on the impactor (red trace) rises dramatically. Note that within our experimental uncertainties, the speed of sound does not increase until the shear-jammed region becomes compressed. Data are averages from seven experiments that simultaneously measured force and sound speed as functions of time. Dashed lines indicate one standard deviation. The grey region shows the uncertainty (given by one standard deviation) in determining Δc at low U_p, where no solidification takes place.

ρ the average material density of the suspension [70, 94]. In our experiments the particles and suspending solvent were density matched, but the average K still increases with ϕ since cornstarch particles have a bulk modulus larger than that of the liquid (see Section 2.4). As shown in Fig. 3.3a, the resulting dependence of c on ϕ is, to good approximation, linear across the regime of ϕ where fronts can be generated. This allows us to find any variation in packing fraction $\Delta\phi = \phi_{\mathrm{f}} - \phi_0$ straightforwardly by detecting changes in c with ultrasound, where ϕ_{f} is the packing fraction in the solid-like region, and ϕ_0 is the initial packing fraction of the suspension.

The experimental setup was identical to the one illustrated in Fig. 3.1. The impactor started from the surface of the suspension and pushed down a distance z_{p}. The position of the impactor was measured with a high speed camera (Phantom V9, Vision Research). The ultrasound measured the time of flight T of the signal transmitted from the bottom, reflected by the impactor and sent back to the bottom. Thus the average speed of sound $\bar{c}$ along this path is

$$\bar{c} = 2\frac{H - z_{\mathrm{p}}}{T}. \tag{3.2}$$

We started with experiments at $U_{\mathrm{p}} = 5$ mm·s^{-1} to measure the speed of sound in the fluid-like, unjammed suspension, where $\bar{c} = c(\phi_0)$. Defining T_0 as the initial time of flight when $z_{\mathrm{p}} = 0$ mm, we have $H = c(\phi_0)T_0/2$, and from this

$$c(\phi_0) = \frac{2z_{\mathrm{p}}}{T_0 - T}. \tag{3.3}$$

The initial packing fraction ϕ_0 in these experiments was 0.48. The liquid was a mixture of 44.3% CsCl, 27.8% glycerol and 27.8% water by mass, with $\eta_0 = 4.6$ mPa·s and $\rho = 1.63 \times 10^3$ kg·m^{-3}. From six measurements we obtain $c(\phi_0) = 1939.2 \pm 4.6$ m·s^{-1} and $H = c(\phi_0)T_0/2 = 34.1 \pm 0.1$ mm.

At fast U_{p} (200 mm·s^{-1}), a front was generated as illustrated in Fig. 3.3b. It indicates two regions: the solid-like region (dark blue) directly underneath the impactor and an unjammed region (light blue) ahead of the front. Here we use the value of H measured above and Eq. 3.2 to calculate $\bar{c}$. The time of flight now becomes

$$T = 2\Big[\frac{H - z_{\mathrm{f}}}{c(\phi_0)} + \frac{z_{\mathrm{f}} - z_{\mathrm{p}}}{c(\phi_0 + \Delta\phi)}\Big]. \tag{3.4}$$

For $\Delta\phi = 0$, $T_{\Delta\phi=0} = 2(H - z_{\mathrm{p}})/c(\phi_0)$. If $\Delta\phi > 0$, there will be a difference between T and $T_{\Delta\phi=0}$, and the difference becomes increasingly larger as z_{f} increases, which leads to an increase in $\bar{c}$ according to Eq. 3.2.

Note that when a suspension transforms from an unjammed state to a jammed state, an increase in ϕ may not be the only cause for a faster speed of sound. There are two other possible mechanisms: (1) an increase in effective bulk modulus K; (2) the development of a finite shear modulus G [26]. Currently we can not determine how much these three mechanisms each contribute, but we can estimate the upper limit of each individual term by assuming the other two to be zero.

Firstly, we estimated the maximum possible increase in ϕ. Fig. 3.3c shows the measured change in sound speed $\Delta c = \bar{c} - c(\phi_0)$ during impact for a suspension prepared at $\phi_0 = 0.48$. The impactor hits the suspension surface at time $t = 0$, generating a front that reaches the bottom at $t \approx 0.035$ s. We can identify this point by the dramatic increase in force on the impactor, as established by prior investigations of quasi-2D [57] and 3D [52] systems. Until the front interacts with the bottom wall $\Delta c = \bar{c} - c(\phi_0)$ is less than the measurement uncertainty of about 5 m/s. Neglecting any increases in K and G, we find from Fig. 3.3a that our noise floor $\Delta c \approx 5$m/s implies $\Delta\phi \approx 0.006$ during the free propagation of the fronts. This means that ϕ could have increased to 0.49 at best. On the other hand, even at the highest packing fraction in Fig. 3.3(a) $\phi = 0.52$, the suspension can still flow when sheared slowly, implying an isotropic jamming threshold ϕ_{J} greater than 0.52. This means that the increase in packing fraction due to impact is much less than required for jamming by the densification model (Eq. 1.6).

If instead we assume $\Delta\phi = 0$ and use $c = \left[\left(K + \frac{4}{3}G\right)/\rho\right]^{\frac{1}{2}}$, as appropriate for solids [67], to describe the dependence of the speed of sound on K and G within the jammed region behind the front, the same noise floor $\Delta c \approx 5$ m/s implies that the net increase in the sum of the moduli $\tilde{K} = K + \frac{4}{3}G$ could not have been larger than $\Delta\tilde{K} \approx 32$ MPa. This is very small compared to the bulk modulus K_0 of the quiescent suspension at $\phi_0 = 0.48$: $\Delta\tilde{K}/K_0 \approx 0.5\%$.

Once the front has reached the bottom, we find $\Delta c \approx 16$ m·s^{-1}. While this is significantly above the noise floor, it limits any packing fraction changes to $\Delta\phi \approx 0.02$, still less than necessary to reach ϕ_{J}. Nevertheless, the interaction with the solid boundary increases the stress in the dynamically jammed region significantly and this drives the suspension deeper into the shear jammed state. We can therefore expect concomitant increases in bulk and shear moduli and thus in sound speed. From the sound speed data in Fig. 3.3, the upper limit of the net increase in the sum of the moduli $\tilde{K}$ is $\Delta\tilde{K} \approx 101$ MPa.

3.4 Impact-activated fronts are shear fronts

From the evolution of the flow fields as shown in Fig. 3.2 we extract the position of the moving jamming front, defining the front position as the line of points where the vertical component of the impact velocity has dropped to $U_{\mathrm{p}}/2$. In the following we focus on the points in the flow field that propagate the furthest in z and r directions, *i.e.*, on the maximum longitudinal and transverse front speeds. As shown in Fig. 3.4a, after an initial stage the fronts in both directions propagate essentially linearly as function of time before slowing down when they start to interact with boundaries and the incipient jammed region gets compressed by the impactor; further compression causes the motion to stop quickly. Here we investigate this linear regime, where the front propagates freely. To compare how quickly the front propagates relative to U_{p}, we define two dimensionless front propagation factors, or normalized front speeds, k as

$$k_{\mathrm{t}} = \frac{U_{\mathrm{ft}}}{U_{\mathrm{p}}},\ k_{\mathrm{l}} = \frac{U_{\mathrm{fl}}}{U_{\mathrm{p}}} - 1, \tag{3.5}$$

where the subscripts t and l represent transverse and longitudinal directions, respectively. The "-1" in k_{l} compensates for the vertical motion of the impactor itself.

Our experiments show that the parameters that affect k_{l} and k_{t} include ϕ, U_{p}, and the suspending liquid's viscosity η_0. For a suspension with given η_0 and ϕ that is impacted very slowly, the response is fluid-like and both k_{t} and k_{l} are close to zero. However, beyond a threshold value U_{p0} fronts start to appear. Their normalized speed initially increases quickly with impactor speed U_{p} but eventually asymptotes to a fixed k^*. The relation between k_{l} and U_{p} in suspensions with the same η_0 but different ϕ is shown in Fig. 3.4b; the behavior of k_{t} is similar. As ϕ increases the curves shift towards lower U_{p0} and higher k^*. For comparison, in suspensions with the same ϕ, larger solvent viscosity η_0 leads to lower threshold U_{p0}. In order to extract k^* and U_{p0} we fit the data to

$$\frac{k}{k^*} = \begin{cases} 0 & (U_{\mathrm{p}} \leq U_{\mathrm{p0}}), \\ 1 - e^{1-U_{\mathrm{p}}/U_{\mathrm{p0}}} & (U_{\mathrm{p}} > U_{\mathrm{p0}}). \end{cases} \tag{3.6}$$

Eq. 3.6 is not derived but a phenomenological relation that captures the key aspects of the data discussed above: (1) $k = 0$ at small U_{p}; (2) k increases when $U_{\mathrm{p}} > U_{\mathrm{p0}}$; (3) k approaches k^* as $U_{\mathrm{p}} \to \infty$. Plotting the data in terms of normalized variables k/k^* and $U_{\mathrm{p}}/U_{\mathrm{p0}}$ scales out the dependencies on ϕ and η_0. The resulting data collapse for the longitudinal front speed ratio $k_{\mathrm{l}}/k_{\mathrm{l}}^*$ is plotted in Fig. 3.4c. A similar result is obtained for the transverse speed ratio $k_{\mathrm{t}}/k_{\mathrm{t}}^*$.

To quantify the anisotropy in front propagation in longitudinal and transverse directions, we plot k_{l}^* versus k_{t}^* in Fig. 3.4d, using data from experiments varying ϕ (larger packing fraction increases both k_{l}^* and k_{t}^*) and η_0. To a good approximation, all data follow $k_{\mathrm{l}}^* = 2k_{\mathrm{t}}^*$.

Comparison with data obtained for quasi-2D suspension [57] shows excellent agreement as well, except that for higher k_t the ratio $k_\mathrm{l}/k_\mathrm{t}$ slightly exceeds 2.

Our data in Fig. 3.3c demonstrate that impact-activated jamming of dense suspensions proceeds without significant increase of ϕ, and certainly without increasing ϕ to values close to ϕ_J. This rules out earlier explanations based on entering the jammed state via densification of the particle sub-phase [52, 58]. On the other hand, analysis of the flow field shows that the jamming fronts initiated by the impact coincide with the location of the maxima in local shear rate (Fig. 3.2 d and e). Together, these two findings provide strong evidence for dynamic shear jamming: the impact triggers propagating fronts that locally create sufficient shear to reorganize particles into (anisotropic) jammed configurations without changing the average packing fraction. There are several implications of the shear jamming scenario for suspensions and several differences from dry granular systems, both of which we discuss next.

To start, we examine the stress. In a dry granular system stress is sustained only via direct contact between particles. By contrast, in a dense suspension stress can also be transmitted without contact via lubrication forces. Thus while in dry granular systems there is only a single characteristic stress scale for entry into the shear-jammed regime [24], for a suspension the situation can be more complex. A number of theoretical models [41], simulations [36, 38, 39] and experiments [23, 31, 33, 48] have recently suggested that lubrication breaks down and particles start to experience frictional interactions beyond a local stress threshold Σ_1. Thus, for stress levels below Σ_1 the suspension behaves fluid-like, while above Σ_1 the system can be thought to behave more like a frictional granular system, *i.e.*, enter a fragile regime before crossing over into the shear-jammed regime at a second characteristic stress level Σ_2 [24, 25]. Within this picture, we associate the transition at U_p0 with the situation where the stress levels at the leading edge of the jamming front have reached Σ_1 and are large enough for frictional interactions to occur. Thus, when $U_\mathrm{p} < U_\mathrm{p0}$ the suspension is in the lubrication regime, but when $U_\mathrm{p} > U_\mathrm{p0}$ it transforms into a fragile state with behavior intermediate between solid and fluid [6, 24, 95], as frictional contacts

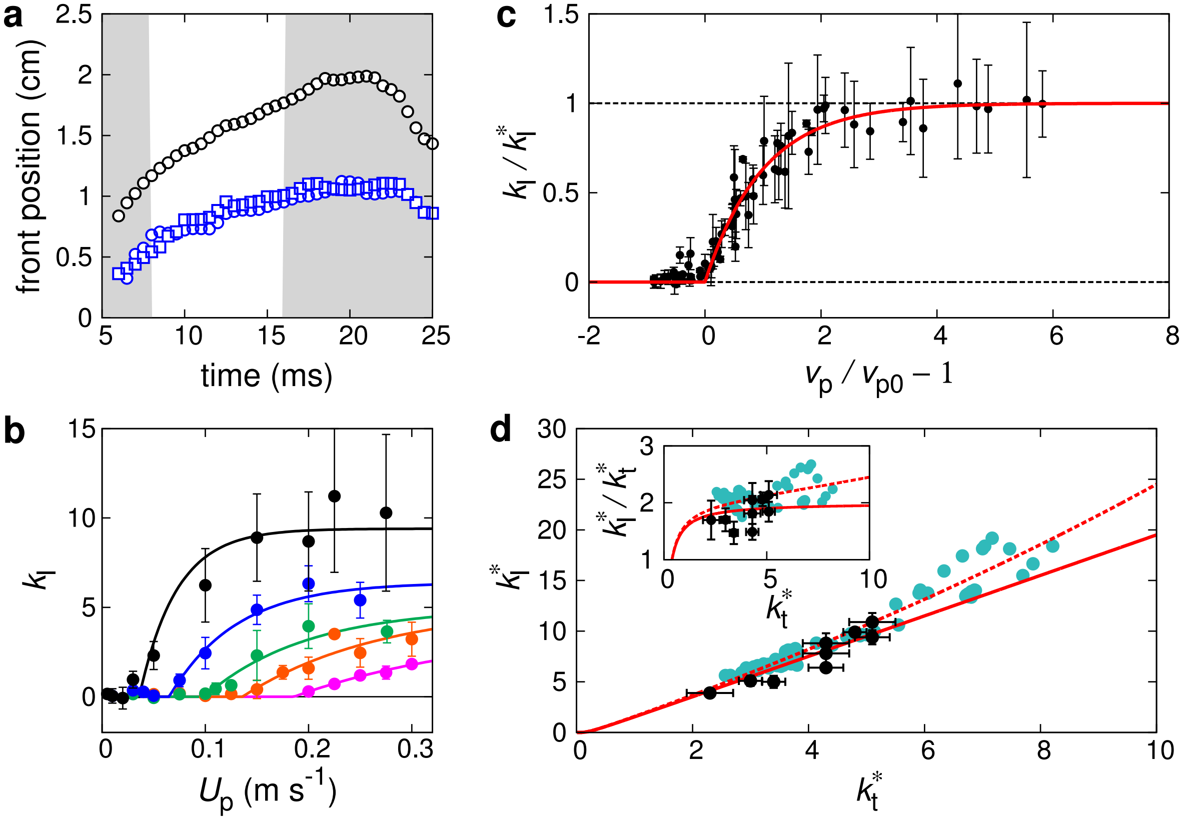

Figure 3.4: Propagation of impact-activated fronts. (a) Front position in longitudinal (black) and transverse (blue circles: right, blue squares: left) directions as functions of time. The impactor touches the suspension surface at time $t = 0$ ms. The grey shaded background indicates the initial front build-up (left), and the regime where the fronts starts to interact with boundaries and slows down (right). For these data $U_\mathrm{p} = 200$ mms, $\phi = 0.460$. (b) Normalized front propagation speed k_l in longitudinal direction as function of U_p for different ϕ (magenta: 0.439, orange: 0.453, green: 0.460, blue: 0.474, black: 0.498). All data are for suspending liquid viscosity $\eta_0 = 4.6 \pm 0.2$ mPa·s. Error bars show the standard deviation of three measurements. (c) Front speed $k_\mathrm{l}/k_\mathrm{l}^*$ normalized by its asymptotic value as function of impactor speed U_p normalized by threshold speed U_p0. Data from experiments with different ϕ and η_0 collapse onto a master curve of Eq. 3.6 (solid red line). (d) Relationship between the asymptotic front speeds k_l^* and k_t^*. Data from both quasi-2D [57] (turquoise) and 3D (black) impact experiments are shown. The solid red line is the prediction from Eq. 3.7. The slope approaches 2 as k_t^* increases. The dashed red line is a modified version of the model, which includes a small strain anisotropy δ, here plotted using a value of $\delta = 0.01$. Error bars are the asymptotic standard error from the fittings of each k-U_p curve with Eq. 3.6.

start percolating through the system to form a load-bearing network, eventually reaching a shear-jammed state as U_p increases further. We point out that a non-zero shear modulus is not strictly necessary for the front to propagate (with $k > 0$). The front will propagate as long as it transforms the initially liquid-like suspension into a state with sufficiently large viscosity. However, we know that this state behaves solid-like while interacting with a system boundary [52, 53, 25, 57]. Thus, how the shear modulus evolves in the region behind the jamming front before a system-spanning jammed state has been established remains an open question. We will continue this discussion in Chapter 4. In Chapter 5, we will link Σ_1 and Σ_2 to the onset stress of DST, Σ_DST, and of shear jamming, Σ_SJ, under steady-state shearing.

The above stress-based argument also provides an explanation of the relaxation or "melting" of the jammed region when the impact stops. During front propagation the stress inside the solid-like region is sustained by the inertia of the suspension in the shear zone. When the motion of the impactor stops, the shear zone disappears and the stress applied on the boundary of the jammed suspension falls below Σ_1, insufficient to sustain frictional interactions between particles and therefore any network of force chains that could generate a yield stress and support a load. As a result, the suspension returns to the lubrication regime.

However, while necessary, the existence of threshold stress levels is not sufficient to explain the asymptotic front speed k^* at high U_p and the seemingly universal anisotropy in front propagation, expressed by the ratio $k_\mathrm{l}^*/k_\mathrm{t}^* \approx 2$. Particles also need to move out of an initial uniform isotropic distribution and reorganize under shear into anisotropic structures (force networks) that can support the stress. Such reorganization requires a minimum shear strain ε_c to engage neighboring particle layers. As a result, shear jamming happens only when stress and strain both reach their threshold values. In a quasi-static granular system [24, 40] the threshold strain only matters when the shear jammed state is prepared or when the shear is reversed. In the dynamic system considered here, the front continues to propagate into unperturbed suspension, and therefore, the front advances by applying strain ε_c locally during the whole process of front propagation.

For dense suspensions in the high U_p regime, where the stress threshold is clearly exceeded, we can show that k^* is governed by ε_c and that, in fact, the front speed anisotropy is a direct consequence of the existence of a strain threshold. As described above, the suspension experiences pure shear in the longitudinal direction and simple shear in the transverse direction. In 2D we can directly compare the two types of shear using the positive eigenvalues of the shear rate tensors, treating the propagation of the front in the longitudinal and transverse directions as two effectively 1D problems. We now assume that a suspension element jams when the shear strain it experiences reaches ε_c, irrespective of propagation direction. This leads to the following relations between k_l^*, k_t^* and ε_c (see Appendix C):

$$k_\mathrm{t}^* = 1/(2\varepsilon_\mathrm{c}),\ k_\mathrm{l}^* = 1/(e^{\varepsilon_\mathrm{c}} - 1) \tag{3.7}$$

and

$$k_\mathrm{l}^* = \frac{1}{e^{1/(2k_\mathrm{t}^*)} - 1}. \tag{3.8}$$

Eq. 3.8 is plotted in Fig. 3.4d. For small ε_c we find from Eq. 3.7 that $k_\mathrm{l}^* \approx 2k_\mathrm{t}^* = 1/\varepsilon_c$. In other words, the anisotropy ratio of 2 in the normalized front speeds originates from the factor 1/2 in the non-diagonal terms of the shear rate tensor, which in turn arises because simple shear can be decomposed into a combination of pure shear and solid body rotation. In 3D it is not possible to quantify the effects of pure shear and simple shear via the same approach (see Appendix D). However, one possible solution is to use the "strain intensity" $\mathscr{D}$ [96], which provides a scalar measure of the relative strength of the two types of shear. As we show in Appendix D, this leads to a ratio $k_\mathrm{l}^*/k_\mathrm{t}^* \approx 3/\sqrt{2} \approx 2.12$, very close to the value for the 2D case. Therefore, an anisotropy ratio ≈ 2 agrees very well with the experimental data for both quasi-2D [57] and 3D systems within our measurement precision.

With increasing packing fraction ϕ we expect the strain threshold ε_c to decrease, which agrees qualitatively with the measurements of ε_c in dry granular systems [24]. Via Eq. 3.7 this explains the increase in k^* with ϕ seen in Fig. 3.4b: since it takes less strain to reorganize the particles into a shear-jammed network the front will propagate faster for given impactor velocity. We point out that Eq. 1.6, which formalizes such relationship between packing fraction and front speed, appears to capture the overall trend qualitatively. However, this seems fortuitous, since Eq. 1.6 was based on the assumption that the moving front significantly increases the packing fraction, in fact driving it up all the way to ϕ_J, which we now can rule out in our system. In addition, Eq. 1.6 cannot predict the observed propagation anisotropy. One of the outstanding tasks therefore is to develop a model for $k^*(\phi)$ that is based on jamming by shear rather than densification. We will provide such model in Chapter 4.

An interesting aspect of the data in Fig. 3.4d is the deviation from the anisotropy ratio ≈ 2 at large k^* values or, equivalently, large packing densities. This is most apparent in the data available for the quasi-2D system and it indicates that the longitudinal speed becomes faster. We speculate that this may be connected to a breakdown of the assumption of an isotropic threshold ε_c. For example, if the impact were to introduce a small amount of compression of the particle sub-phase in longitudinal direction, ε_c would be reduced in that direction. This effect would become increasingly significant at large ϕ. We can model this by introducing a correction δ so that

$$k_\mathrm{l}^* = 1/(e^{\varepsilon_\mathrm{c}-\delta} - 1). \tag{3.9}$$

Using $\varepsilon_\mathrm{c} = 1/(2k_\mathrm{t}^*)$ and $\delta \approx 0.01$ we can reproduce the trend in Fig. 3.4d well (dotted red line). However, we point out that this is just the simplest way to account for the trend in the data and there might be other reasons for the deviation.

3.5 Conclusions

Taken together, these results provide important insights into the mechanism responsible for impact-induced solidification of dense suspensions. The finding that the packing fraction does not increase measurably during impact, together with the observation of strong shear at the leading edge of the propagating solidification fronts, rules out jamming via densification as the dominant mechanism and points to jamming by shear (densification is likely to play a significant role at much larger impact velocities, when the interstitial liquid's compressibility can no longer be neglected [90]). In dense suspensions this introduces a new stress scale or, equivalently, an impact velocity threshold, which we associate with the breakdown of lubrication films between particles and the onset of frictional interactions [36, 41, 31, 23, 48]. Behind the front, these frictional interactions create a dynamically shear-jammed region (corresponding to fragile and/or shear jammed states in [41, 24]). Further support for the shear-jamming scenario comes from the observation of anisotropic front propagation, where we can relate the fact that the fronts propagate longitudinally twice as fast as in transverse direction to an equivalent factor in the ability to transmit shear strain. We point out that for dynamic shear jamming, both shear stress and strain need to exceed threshold values, and the critical shear strain determines the front propagation speed.

CHAPTER 4

MODELING SHEAR FRONTS IN ONE DIMENSION[1]

4.1 Introduction

Efforts to map out a state diagram that delineates the properties of dense suspensions as a function of packing fraction and imposed forcing have focused almost exclusively on steady-state conditions. However, this does not capture the many remarkable transient phenomena exhibited by suspensions [51, 50, 52, 57, 53, 97, 56, 98, 25]. Only a couple years ago was it discovered [52, 57] that the impact-activated solidification is a dynamic process where impact at the suspension surface initiates jamming fronts that rapidly propagate into the bulk of the material, and transform the suspension from a fluid-like into a solid-like state in its wake. The jamming fronts discussed here are created by a different mechanism compared to compression fronts in granular materials below jamming [99, 100], above jamming [101, 102], or shear shocks in fragile networks [103]. So far, several key aspects have remained largely unresolved, including (1) the conditions under which dense suspensions can develop jamming fronts; (2) the shape of the flow profile at the front; and importantly (3) the relation between the applied stress and the front speed. These questions underline the need to build a description that would encompass both transient and steady-state properties of shear thickening materials.

In this Chapter, we consider the arguably simplest geometry in which these properties can be measured: a plane of fluid that is sheared along one of its boundaries. With a resulting flow field that changes only along the direction perpendicular to the sheared boundary, this configuration exhibits one-dimensional (1D) dynamics. A key finding is that the velocity-stress relation measured at the boundary, i.e., the macroscopic response of the suspension to applied forcing, is governed by a microscopic, particle-scale quantity: the amount of strain accumulated locally when the jamming front passes through. This accumulated strain

---

[1] This Chapter is based on Endao Han, Matthieu Wyart, Ivo R. Peters, and Heinrich M. Jaeger, Shear fronts in shear-thickening suspensions. Physical Review Fluids 3(7), 073301 (2018).

depends on both the intrinsic properties of the suspension, such as the packing fraction, and the system's initial preparation condition. We can capture this transient behavior by introducing one additional parameter, a strain amplitude γ^* characterizing the cross-over to steady-state flow, into a model originally developed for steady state rheology [41]. With this generalization the model exhibits well-defined jamming fronts and allows us to compute their dependence on packing fraction and forcing conditions, leading to predictions for (1,2,3) in close agreement with our experimental observations.

4.2 Quasi-one dimensional wide gap shear experiment

Our experimental system, based on Ref [57] and illustrated schematically in Fig. 4.2, consisted of a layer of cornstarch suspension into which a thin plate was inserted. Starting from rest, the plate was impacted by a computer-controlled linear actuator (Parker ETT050) and then moved along the y-direction at constant speed U_0. The suspension was floated on heavy, low-viscosity oil (Fluorinert FC-3283 from 3M), providing a nearly stress-free boundary condition. This allowed us to deduce the stress applied at the boundary from the momentum of the suspensions, which we measured experimentally. A high-speed camera (Phantom V12) was used to image the motion of the suspension surface. The videos were analyzed using a particle imaging velocimetry (PIV) algorithm to obtain the flow field.

4.2.1 Features of dynamic shear fronts

At high enough boundary speed U_0, shear fronts can be generated. The flow field obtained inside the dashed red box in Fig. 4.1 is shown in Fig. 4.2a. Colors represent the y component of local velocities v_y. In the yellow regions, the suspension moved with a velocity very close to $U_0 = 0.46$ m/s, and in the dark green regions the suspension did not move. We can see a clear boundary between the yellow and green regions that propagate away from the plate and into the bulk. The system is, to very good approximation, quasi-1D, with significant flow

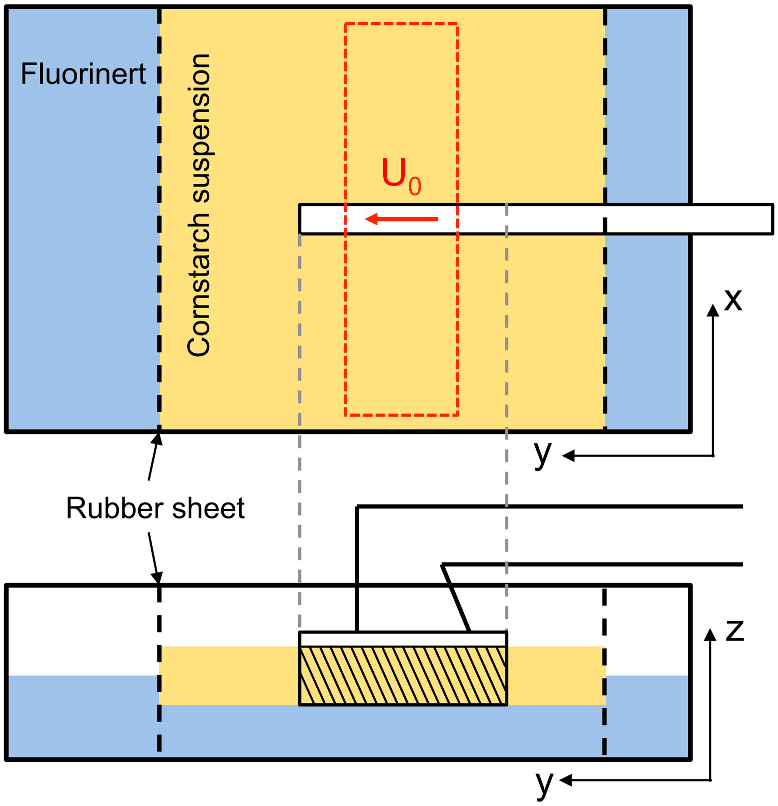

Figure 4.1: Illustration of the wide-gap shear experiment. The setup consists of a layer of cornstarch suspension (yellow) that floats on a heavy oil (blue). Dashed black lines represent rubber sheets confining the suspension. An acrylic plate with roughened surface was inserted in the middle of the container (at $x = 0$ m) and moved with speed U_0. The dashed red box indicates the area used for data analysis. The shaded area in the side view illustrates the cross sectional area S_p.

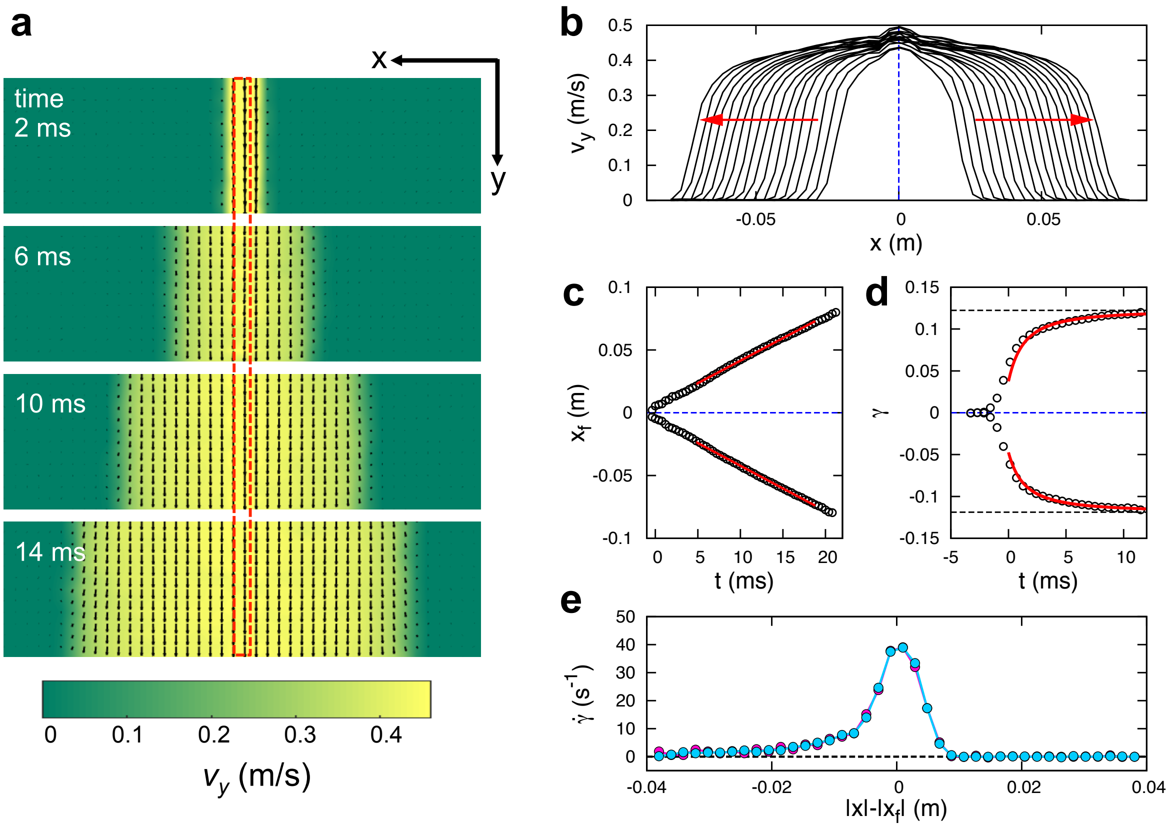

Figure 4.2: Flow of the shear front obtained from the quasi-1D experiment. (a) Flow field on the suspension surface at four different times. Arrows label local velocities. Colors represent v_y. Dashed red box outlines the position and width of the plate. (b) Exemplary velocity profiles of a shear front for $\phi = 0.532$ and $U_0 = 0.46 \pm 0.02$ m/s, propagating transversely to either side of the plate (dashed blue line). (c, d) Front position x_f and accumulated strain γ as functions of time t. In (c), red lines show linear fits. In (d), time $t = 0$ ms represents the time when $x = x_\mathrm{f}$. Red lines show fits to a power law. Black dashed lines indicate the asymptotic accumulated strain γ_∞. (e) Local shear rate calculated from the mean velocity profiles. Blue and pink represent the left and right branches, respectively, in (b).

field gradients only along the x direction. We therefore average in the y direction and leave x as the only spatial coordinate. Fig. 4.2b shows the evolution of the resulting, averaged velocity profiles. As the arrows indicate, a moving region rapidly expands outward to either side of the plate, while the shape of the velocity profiles stays approximately invariant.

For convenience, we define the front position x_{f} as the point on a velocity profile where $v_y = 0.45U_0$. As shown in Fig. 4.2c, x_{f} is a linear function of time on both sides of the plate, providing a well-defined, constant front propagation speed U_{f}. In the example shown $U_{\mathrm{f}} = 3.60 \pm 0.03$ m/s, which is 7.8 times the plate speed $U_0 = 0.46 \pm 0.02$ m/s, but much slower than the speed of sound in the material (above 1900 m/s, see Chapter 3). From the flow fields, we also extract the local accumulated strain γ as a function of time. Because of the invariance of the velocity profiles, we collapse the γ-t curves at different x using the time when the front reaches that position, *i.e.* $x_{\mathrm{f}}(t) = x$. As shown in Fig. 4.2d, γ increases quickly at the beginning, but then slows down because of shear thickening. The red curves are power law fits to the data for $t > 0$ ms and indicate that the accumulated strain will approach 0.12 asymptotically. This asymptotic approach to a finite value of the accumulated strain γ_∞ (under continued finite stress) is a clear indicator of jamming

To obtain the shear rate distribution along the velocity profiles we average them after shifting the front positions x_{f} to zero. The absolute value of the local shear rate $|\dot{\gamma}| = |dv_y/dx|$ is shown in Fig. 4.2e [2]. The maximum shear rate $\dot{\gamma}_{\max}$ is found close to the front position. The shear rate profile is not symmetric with respect to $|x| - |x_{\mathrm{f}}| = 0$, exhibiting a steeper gradient at the leading edge ($|x| > |x_{\mathrm{f}}|$). Behind the front, we observe a tail of small, but finite shear rate. Thus, strictly speaking, the region in the wake of the passing front does not immediately become a jammed solid. However, as the front keeps moving ahead and the local strain approaches γ_∞, a jammed state with non-zero shear modulus is reached. By contrast, if a suspension does not "jam" but only shear "thickens", we expect the accumulated strain

---

[2] Since in our 1D system, γ always changes monotonically, we only consider the absolute value of $\dot{\gamma}$ and γ. In the paper the signs on $\dot{\gamma}$ and γ are ignored.

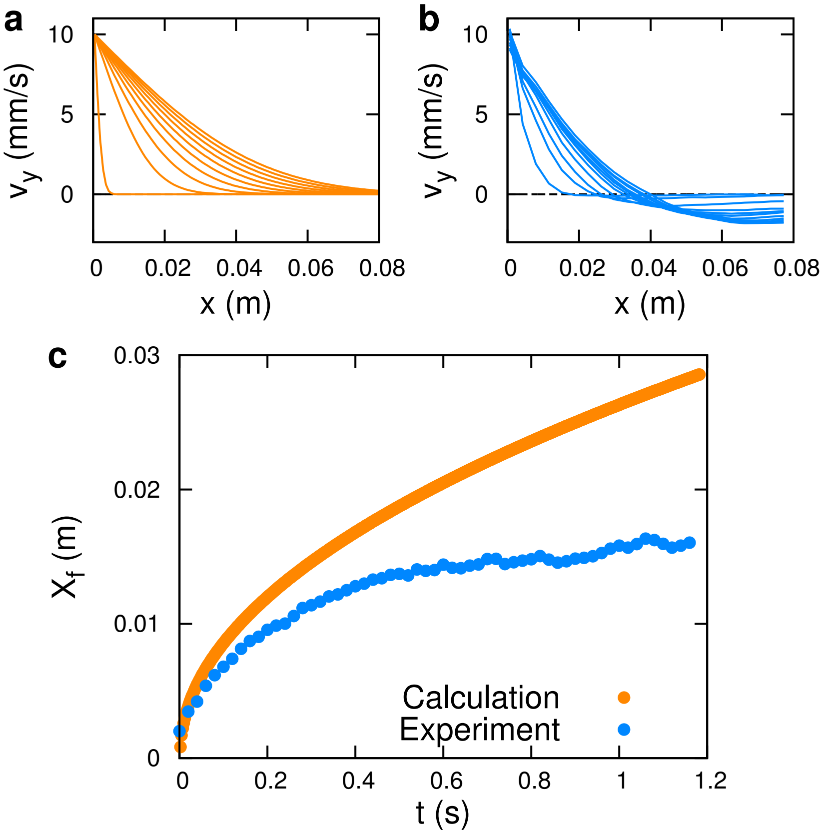

Figure 4.3: Flow profiles in the fluid-like regime and "front" position x_f at $\phi = 0.521$ and $U_0 = 0.01$ m/s. (a) Numerical calculation based on the model. (b) Experimental data. (c) Position of the front, defined as the position where $v_\mathrm{y} = 0.45U_0$.

to keep growing and the shear rate to stay finite.

From this discussion, we extract three defining features for jamming fronts: (1) A well-defined, step-like velocity profile that stays invariant over time; (2) A constant propagation speed U_f; (3) An asymptotically accumulated strain that stays finite. These characteristics distinguish jamming fronts from the more diffusive response to applied shear that occurs at low driving speeds U_0 or at low packing fractions, as discussed below. We will use these three features in comparing model calculations to the experiments.

Like the impact-activated fronts discussed in Chapter 3, the 1D shear fronts are generated only above a threshold boundary velocity. When U_0 is sufficiently slow, the suspension is in the lubrication regime and behaves like a Newtonian fluid. For a Newtonian fluid sheared in a semi-infinite 1D system, the flow profile is self-similar with a characteristic length scale $\sqrt{\nu t}$, where ν is the kinematic viscosity. If we define a normalized, time-dependent length scale $s_\nu = x/(\sqrt{\nu t})$, the velocity $v_y(x,t)$ is [104]:

$$v_y(x,t) = U_0\left[1 - \mathrm{erf}(s_\nu/2)\right], \tag{4.1}$$

where $\mathrm{erf}(x)$ is the error function. The numerically calculated and experimentally measured flow profiles at $\phi = 0.521$ and $U_0 = 0.01$ m/s are shown in Fig. 4.3 as an example. One major difference is that in the calculation the system is strictly one-dimensional and semi-infinite, so the local velocity is always positive during the whole process. However, in the experiment negative flow velocity is observed further away from the plate, which originates from fluid re-circulation due to the finite container size. However, we can still define the "front position" x_f as the x position at which $u = 0.45U_0$. As shown in Fig. 4.3c, in the calculation x_f keeps growing as a function of time, and before the flow reaches the other boundary it satisfies $x_\mathrm{f} \propto \sqrt{\nu t}$, where $\nu = \eta_0(1-\phi/\phi_0)^{-2}/\rho$. In the experiments, the front almost stopped propagating at late time and reached a steady state.

As U_0 increases, we start to see a front that propagates out. However, before U_0 is sufficiently fast, the flow does not exhibit the three defining features of jamming fronts. For example, the x_f-t relation is not strictly linear at intermediate driving speed. We now focus on the limit of sufficiently fast U_0, where we obtain jamming fronts as defined above.

4.2.2 Front speed and accumulated strain

Here we consider how U_f, γ_∞, the stress at the boundary Σ, and the maximum shear rate $\dot\gamma_\mathrm{max}$ depend on the wall velocity U_0 at different ϕ, as shown in Fig. 4.4. We define the normalized front propagation speed as $k \equiv U_\mathrm{f}/U_0$. The variation of k as a function of U_0 is presented in Fig. 4.4a, and Fig. 4.4b shows the corresponding γ_∞. At $\phi \leq 0.5$, both k and γ_∞ are essentially constant. For the largest values of ϕ and U_0 we probed, departures

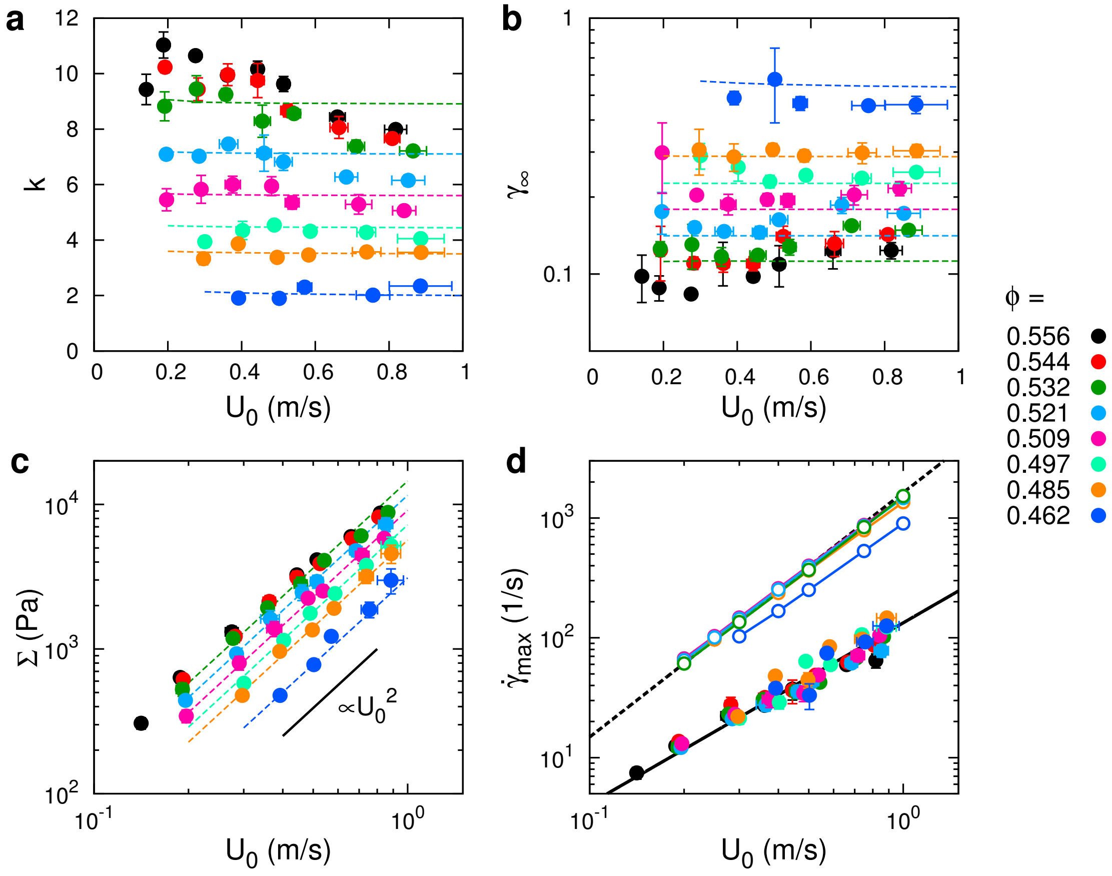

Figure 4.4: Characteristics of propagating jamming fronts as function of shearing speed U_0. Experimentally obtained data for different packing fractions ϕ are shown by solid symbols. In (a-c), dashed lines are from model calculations. (a) Dimensionless front propagation speed k. (b) Asymptotic accumulated strain γ_∞. (c) Stress at the boundary Σ. Solid circles are calculated by plugging experimentally measured U_0 and k into Eq. 4.3. Dashed lines show the stress at the boundary obtained from the numerical calculations, which satisfy $\Sigma \sim U_0^2$. (d) Maximum shear rate $\dot{\gamma}_{\mathrm{max}}$. Open circles are from the model (the same color scheme is used as for data from the experiments). Black lines are power law fits.

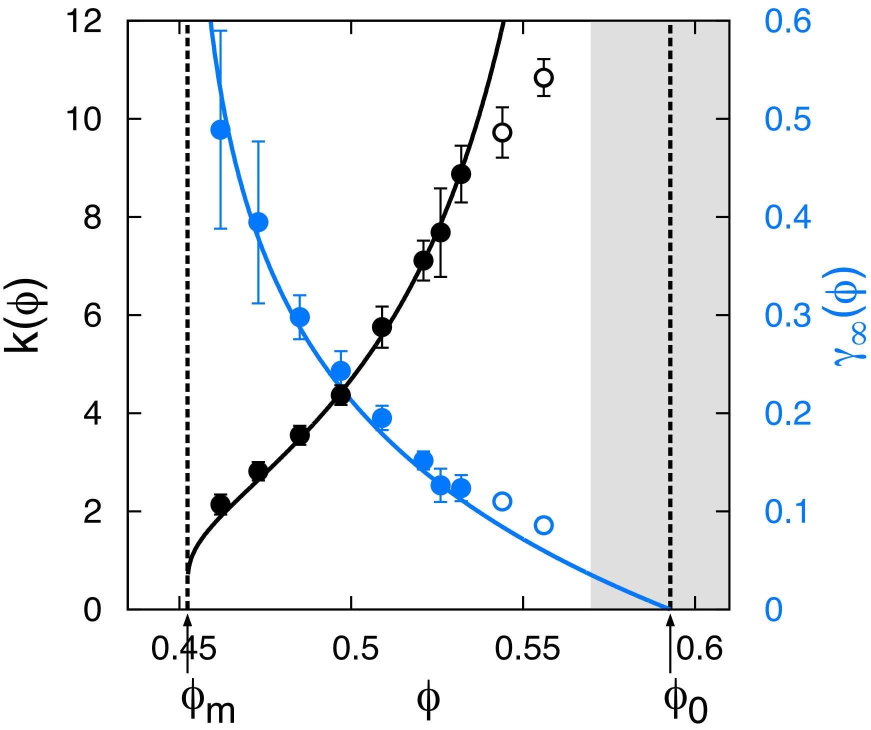

Figure 4.5: Dimensionless front propagation speed k (black) and asymptotic accumulated strain γ_∞ (blue) as functions of packing fraction ϕ. The blue curve shows Eq. 4.19, and the black curve shows its reciprocal, both with $\gamma^* = 0.197$. Data at $\phi = 0.556$ and 0.544 are represented by open circles.

from this constant behavior can be detected, an effect whose relative magnitude can be as large as 30%. Still, for each $\phi < 0.54$, we can find a range in which k and γ_∞ are nearly independent of U_0. Using the average value in such a range, we can define $k(\phi)$ and $\gamma_\infty(\phi)$ at each ϕ. Note that $\gamma_\infty(\phi)$ decreases with increasing ϕ, and the trend is reversed for $k(\phi)$. These results are documented in Fig.4.5.

Visual inspection of Fig. 4.4a, Fig. 4.4b, and Fig.4.5 suggests an inverse relationship between k and γ_∞, which we now derive. The total accumulated strain when the front passes through is $\gamma_\infty = \int_{-\infty}^{+\infty} \dot{\gamma} dt$. For a propagating front with invariant shape, we have $\dot{\gamma} = \frac{\partial v}{\partial x} = \frac{\partial v}{U_\mathrm{f} \partial t}$, so that

$$\gamma_\infty = \frac{1}{U_\mathrm{f}} \int_0^{U_0} dv = \frac{U_0}{U_\mathrm{f}} = \frac{1}{k}. \tag{4.2}$$

Thus, how fast a jamming front propagates depends on how much total strain is accumulated locally as the jamming front moves through. The physical picture is that a finite strain is required to shear the suspension out of an initial state, where the particles are uniformly distributed, into a contact network that jams. The denser the particles pack, the less rearrangement is necessary toward jamming and, consequently, the front propagates faster.

To further prove that the front propagation speed depends on the microscopic particle configuration, we prepared an anisotropic initial state of the suspension by moving the plate at a slow speed U_{pre} prior to the high speed shear. We moved the plate 10 mm forward or backward at $U_{\text{pre}} = 1$ mm/s or 10 mm/s, and then applied fast shear at U_0. Results for $\phi = 0.526$ and $U_0 = 0.36$ m/s are shown in Fig. 4.6 as an example. The front will propagate faster (slower) if the suspension has been pre-sheared along the same (opposite) direction. This suggests that the front propagation speed not only depends on ϕ, but also on the system preparation conditions and the straining history.

We performed pre-shear at different U_{pre} (from 0.1 mm/s to 10 mm/s), and waited for different lengths of time between pre-shear and fast shear, from several seconds to 10 minutes. In each case we obtained almost identical x_{f}-t curves, as long as U_{pre} was slow enough so that the suspension remained fluid-like. This also shows that cornstarch suspensions can be treated as an athermal system over time scales as long as several minutes. Note that in our experiments the velocity profile was not always linear during the pre-shear. This was due to the limited range the plate could move, so the distribution of "pre-strain" was not exactly the same everywhere. When the pre-shear finished, the accumulated strain close to the plate was the maximum and it decreased gradually to the side. As a result, in the following step, when sheared at speed U_0, U_{f} slowed down as it propagated away from the plate, which can be seen in Fig. 4.6.

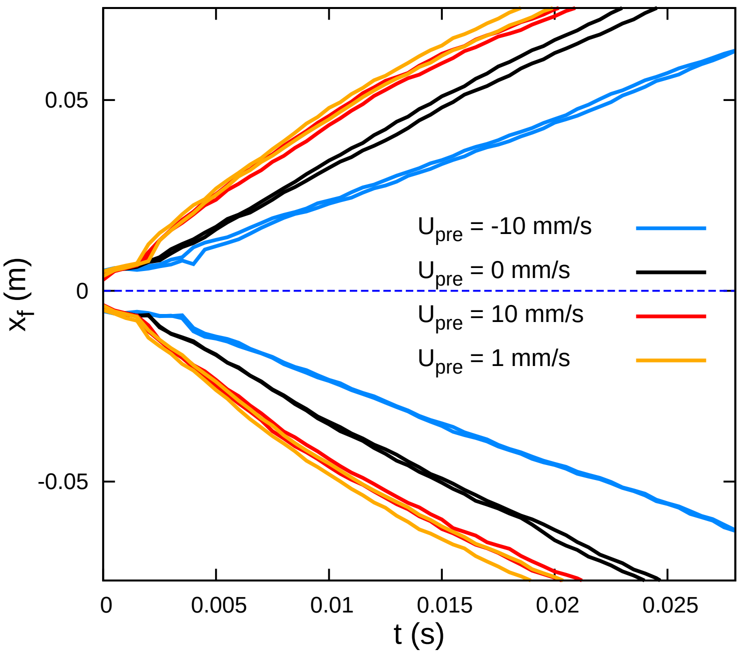

Figure 4.6: Front position as a function of time for different pre-shear. The fast plate speed was $U_0 = 360$ mm/s, and the slow pre-shear speed U_{pre} varied as labeled in the plot. Positive U_{pre} represents pre-shear in the same direction as U_0, and negative U_{pre} was in the opposite direction.

4.2.3 Relation between applied stress and front speed

In our geometry, a relation connecting the applied stress Σ to the velocity U_0 is readily extracted from momentum conservation. The momentum of an elongating jammed part of the material with a cross sectional area S_p in the plane perpendicular to the front propagation direction is $p = \rho S_\mathrm{p} x_f U_0$. Equating the time derivative of this quantity with the force ΣS_p, one obtains:

$$\Sigma = \rho U_0 U_\mathrm{f} = \rho k U_0^2, \tag{4.3}$$

where $\rho = 1.63 \times 10^3$ kg/m^3 is the density of the suspension. We calculated Σ with Eq. 4.3 using the experimental data. As Fig. 4.4c shows, the dependence of Σ on U_0 matches a quadratic power law well. Interestingly, the form of Eq.4.3 is identical to the expression for the dynamic pressure in a normal fluid, except that the density is renormalized by a factor k, so the effective density becomes $\rho_\mathrm{eff} \sim k\rho$, where k can be as big as a factor of 10 according to our experiments. This "added mass" generated by the propagating fronts was tracked and imaged in previous impact experiments [52, 57, 97].

Note that as the shear stress increases with U_0, so does the normal stress. As the front passes by, the surface of the suspension turns from smooth to matte due to the dilation of grains [105]. The protrusion of particles increases the confining stress applied by surface tension at the suspension-air interface [21]. However, there is an upper limit in confinement stress at free interfaces, which is of order 10^3 Pa for our suspensions [11]. As a result, at sufficiently fast U_0 the material could expand near the surface, causing ϕ to decrease in the bulk [32]. This effect may lead to the departure of the power-law behavior in Fig. 4.4c for the largest stresses we probed, or equivalently (according to Eq.4.3) to the erosion of the U_0-independent behavior of k in Fig. 4.4a. In the model developed below, we neglect this dilation effect, thus it predicts a constant $k(U_0)$ at fast U_0.

4.2.4 Maximum shear rate

The maximum shear rate $\dot{\gamma}_{\text{max}}$ characterizes the steepness of the fronts. It is inversely related to the front width Δ since dimensionally we must have $\Delta \sim U_0/\dot{\gamma}_{\text{max}}$. Fig. 4.4d shows $\dot{\gamma}_{\text{max}}$ as a function of U_0. The experimental data for different ϕ from 0.462 to 0.532 collapse to very good approximation onto a single curve, revealing a power law of the form $\dot{\gamma}_{\text{max}} \propto U_0^b$, with exponent $b_{\text{exp}} = 1.51 \pm 0.09$. From this observation we can deduce that $\Delta \propto U_0^{1-b} \propto U_0^{-0.5}$. Since $\dot{\gamma}_{\text{max}}$ is roughly independent of ϕ, we predict the front width to be insensitive to ϕ, which is different from what was found in the case of compression front [99].

4.3 Validating the original Wyart-Cates model with steady-state rheology

The steady-state rheology experiments were performed with an Anton Paar MCR 301 rheometer. The suspensions were tested between parallel plates, and the diameter of the upper plate was 25 mm (tool PP25). An enclosed solvent trap was used to prevent evaporation. We performed both shear rate controlled and shear stress controlled experiments at different ϕ. Before each measurement, the suspension was pre-sheared by ramping from $\Sigma = 0.1$ Pa to 100 Pa for 50 s in total, then sheared slowly at $\Sigma = 0.1$ Pa for 30 s to 60 s. After these two steps of preparation, we ran the actual measurements, where we took 20 data points in a scan from low to high $\dot{\gamma}$ or Σ (from approximately 0.1 Pa to 1000 Pa). At each point the measurement lasted for 10 s to 30 s, and we made sure that the time was long enough so that the viscosity did not vary with time. Some exemplary viscosity-shear rate data (η-$\dot{\gamma}$ curves) at different ϕ are shown in Fig. 4.7a.

The steady-state model predicts that, for suspensions in the CST and DST regimes, the η-$\dot{\gamma}$ curves have two Newtonian regimes: $\eta_{\text{N},1}$ at low stress and $\eta_{\text{N},2}$ at high stress. Both $\eta_{\text{N},1}$ and $\eta_{\text{N},2}$ increase with ϕ, and the stress threshold Σ^* controls the stress at which the transition occurs from one regime to the other. In the experiments there are several

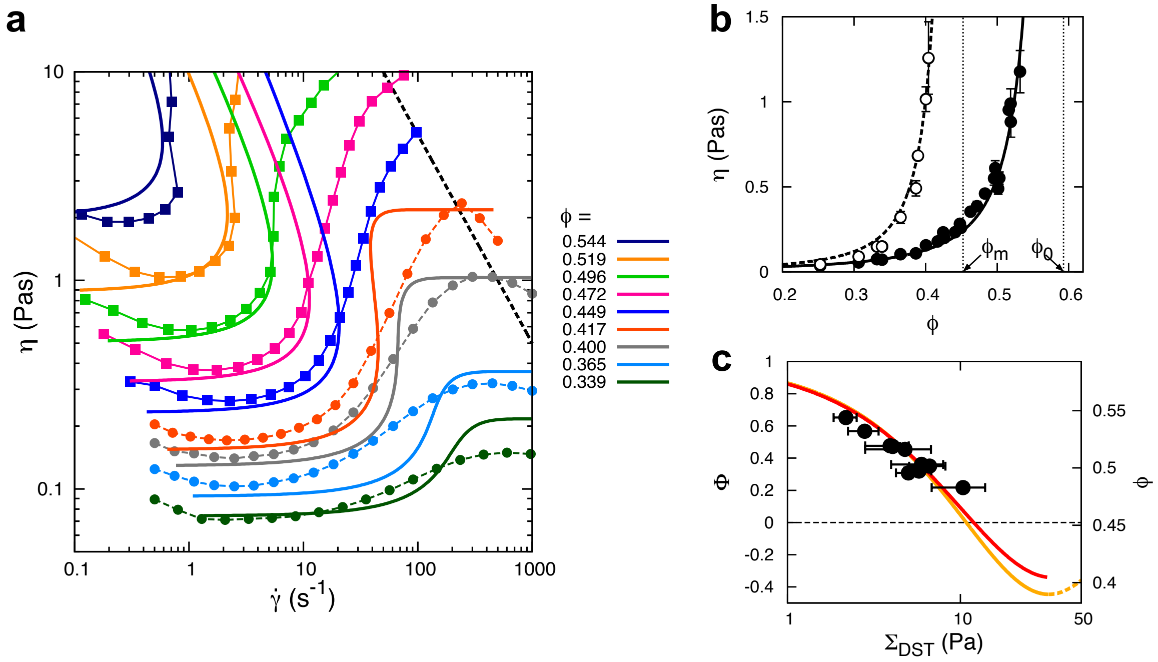

Figure 4.7: Validate the Wyart-Cates model with steady-state rheology. (a) Viscosity η at different shear rates $\dot{\gamma}$ and packing fractions ϕ. Squares connected by thin solid lines represent stress controlled experiments; circles connected by thin dashed lines represent shear rate controlled experiments. The predictions of the Wyart-Cates model are shown by the thick curves with the same color as the experiments. The dashed black line indicates a constant stress $\Sigma = 500$ Pa, which is provided by surface tension and corresponds to the upper limit of stress in steady-state experiments using our shear cell geometry. (b) The lower Newtonian viscosity $\eta_{\mathrm{N},1}$ (solid circles) and higher Newtonian viscosity $\eta_{\mathrm{N},2}$ (open circles) at different ϕ. The two curves show the best fit of $\eta_{\mathrm{N},1}$ and $\eta_{\mathrm{N},2}$ with Eq. 4.5. The vertical dashed lines label ϕ_{m} (left) and ϕ_0 (right) obtained from the fitting. (c) Relation between rescaled packing fraction Φ and onset stress Σ_{DST}. For each Φ, the corresponding ϕ is labeled on the right. The solid black points are experimental data. The red curve is the prediction of the model for $\Sigma^* = 20.4$ Pa.

differences from this model, which we need to account for. Firstly, dense suspensions show shear thinning at low shear rate. To accommodate this we took the average viscosity in the flat section near the minimum of a η-$\dot{\gamma}$ curve as $\eta_{\mathrm{N},1}$. Secondly, the higher branches of the η-$\dot{\gamma}$ curves are more like smooth peaks instead of plateaus. We therefore took the peak values of η as $\eta_{\mathrm{N},2}$. Lastly, in steady-state rheology experiments there is another stress limit set by the surface tension at the suspension-air interface, which confines the suspensions between the parallel plates. The empirical relation is $\Sigma_{\mathrm{max}} \approx 0.1\Gamma/d$, where Γ is the surface tension of the solvent and d is the particle diameter [11, 21]. The surface tension of our solvent was about 75 N/m and the average diameter of cornstarch granules was about 15 μm. As a result, Σ_{max} was 500 Pa approximately. Above this stress the surface tension could not confine the suspension and the measurements became unreliable, *i.e.* the data could no longer be used to extract $\eta_{\mathrm{N},2}$.

According to the model by Wyart and Cates, the viscosity of a suspension is

$$\eta = \frac{\Sigma}{\dot{\gamma}} = \eta_0 \left[1 - \phi/\phi_{\mathrm{J}}(\Sigma)\right]^{-2}. \tag{4.4}$$

In the two limits of Σ, Eq. 4.4 has two asymptotes

$$\begin{aligned} \eta_{\mathrm{N},1} &= \eta_0(1-\phi/\phi_0)^{-2},\ (\Sigma \to 0), \\ \eta_{\mathrm{N},2} &= \eta_0(1-\phi/\phi_{\mathrm{m}})^{-2},\ (\Sigma \to +\infty). \end{aligned} \tag{4.5}$$

This predicts that though both $\eta_{\mathrm{N},1}$ and $\eta_{\mathrm{N},2}$ increase with ϕ, they grow with different rate and diverge at different ϕ: $\eta_{\mathrm{N},2}$ diverges at $\phi = \phi_{\mathrm{m}}$ while $\eta_{\mathrm{N},1}$ diverges at ϕ_0. Fig. 4.7b shows $\eta_{\mathrm{N},1}$ and $\eta_{\mathrm{N},2}$ as functions of ϕ. We fit both $\eta_{\mathrm{N},1}$ and $\eta_{\mathrm{N},2}$ simultaneously on log scales to Eq. 4.5 and obtain the parameters $\eta_0 = 13.6$ mPas, $\phi_0 = 0.593$ and $\phi_{\mathrm{m}} = 0.452$.

We can then use the onset stress of DST, Σ_{DST}, to obtain the threshold stress Σ^*. Σ_{DST}

is the stress at the turning point where a η-$\dot{\gamma}$ curve becomes vertical, so we have

$$\left.\frac{d\dot{\gamma}}{d\Sigma}\right|_{\Sigma=\Sigma_{\mathrm{DST}}} = 0. \tag{4.6}$$

Now with the three parameters η_0, ϕ_0 and ϕ_{m} already extracted, Σ_{DST} is only a function of ϕ and Σ^*. Equivalently, we can use a rescaled packing fraction Φ, defined as

$$\Phi = \frac{\phi - \phi_{\mathrm{m}}}{\phi_0 - \phi_{\mathrm{m}}}. \tag{4.7}$$

Fig. 4.7c shows the relation between Φ and Σ_{DST} obtained from experiments. To obtain the Σ^* that best fits Φ-Σ_{DST}, we varied Σ^* from 15 Pa to 25 Pa. For each Σ^*, we calculated the Σ-$\dot{\gamma}$ curve and found the corresponding Σ_{DST} at the experimentally measured packing fractions. Then we calculated the sum of squared residuals (SSR) between the measured and calculated Σ_{DST}, and obtained $\Sigma^* = 20.4$ Pa, for the minimum SSR.

The four parameters to describe the steady-state behavior of our suspensions are: $\eta_0 = 13.6 \times 10^{-3}$ Pas, $\phi_0 = 0.593$, $\phi_{\mathrm{m}} = 0.452$, and $\Sigma^* = 20.4$ Pa. With these in hand, we can calculate the η-$\dot{\gamma}$ relation at any packing fraction and compare it with the experimental measurement, as shown in Fig. 4.7a. The lowest three curves (green, light blue, and gray) are in the CST regime with $\phi < \phi_{\mathrm{m}}$. The next two curves above, at $\phi = 0.417$ and 0.449, are in the DST regime where $\phi_{\mathrm{m}} < \phi < \phi_0$. In this regime, one might expect to see a discontinuous jump in viscosity, while the transitions seen in the experiments are less sharp than the model predicts. We note that this "sharpness" may be affected by the size distribution of the particles. It has been shown that the onset stress of shear thickening is a function of the particle size [48]: The larger the particles, the smaller the onset stress. Since cornstarch is highly poly-disperse, there should be a distribution of onset stress in the system, which smooths the transition. Lastly, the curves at the four highest packing fractions (from 0.472 to 0.544) are in the jamming regime where $\phi > \phi_{\mathrm{m}}$.

4.4 Generalized Wyart-Cates model for transient flows

The Wyart-Cates model for steady-state rheology of suspensions has been introduced in Section 1.3 and tested in Section 4.3. To model transient phenomena, consider an initial isotropic state where particles are not touching. There must be a characteristic strain γ^* beyond which the microscopic structure becomes anisotropic and particles start to make contact. Let us denote the fraction of such particles by $g(\gamma)$, whose contacts can be frictional or not (if the force is insufficient). $g(\gamma)$ must be a growing function, such as:

$$g(\gamma) = 1 - \exp\left(-\gamma/\gamma^*\right). \tag{4.8}$$

The density of frictional contacts can now be estimated as $g(\gamma)f(\Sigma)$. We thus obtain for the jamming packing fraction:

$$\phi_{\mathrm{J}}(\Sigma, \gamma) = g(\gamma)f(\Sigma)\phi_{\mathrm{m}} + \left[1 - f(\Sigma)g(\gamma)\right]\phi_0, \tag{4.9}$$

where

$$f(\Sigma) = 1 - \exp(-\Sigma/\Sigma^*) \tag{4.10}$$

and $\Sigma^* = \mu P^*$. Making the additional approximation[3] that also in the transient the viscosity only depends on ϕ_{J} we obtain for the shear stress (in the spirit of Eq. 1.5):

$$\Sigma = \eta_0\dot{\gamma}\left[1 - \phi/\phi_{\mathrm{J}}(\Sigma, \gamma)\right]^{-2}, \tag{4.11}$$

where η_0 is the solvent viscosity. Note that this equation can be applied to higher dimensions as well, where Σ and $\dot{\gamma}$ now indicate the shear stress and shear strain tensors respectively[4].

---

[3] This is clearly a simplification, as the viscosity should not only depend on the fraction of frictional contacts, but also on the anisotropy of the contact network characterized by γ. Our results support that this dependence is not essential to describe fronts.

[4] To describe propagating fronts in two or three dimensions, one may further assume that ϕ is constant in space since particle migration is slow, and use that the material is incompressible.

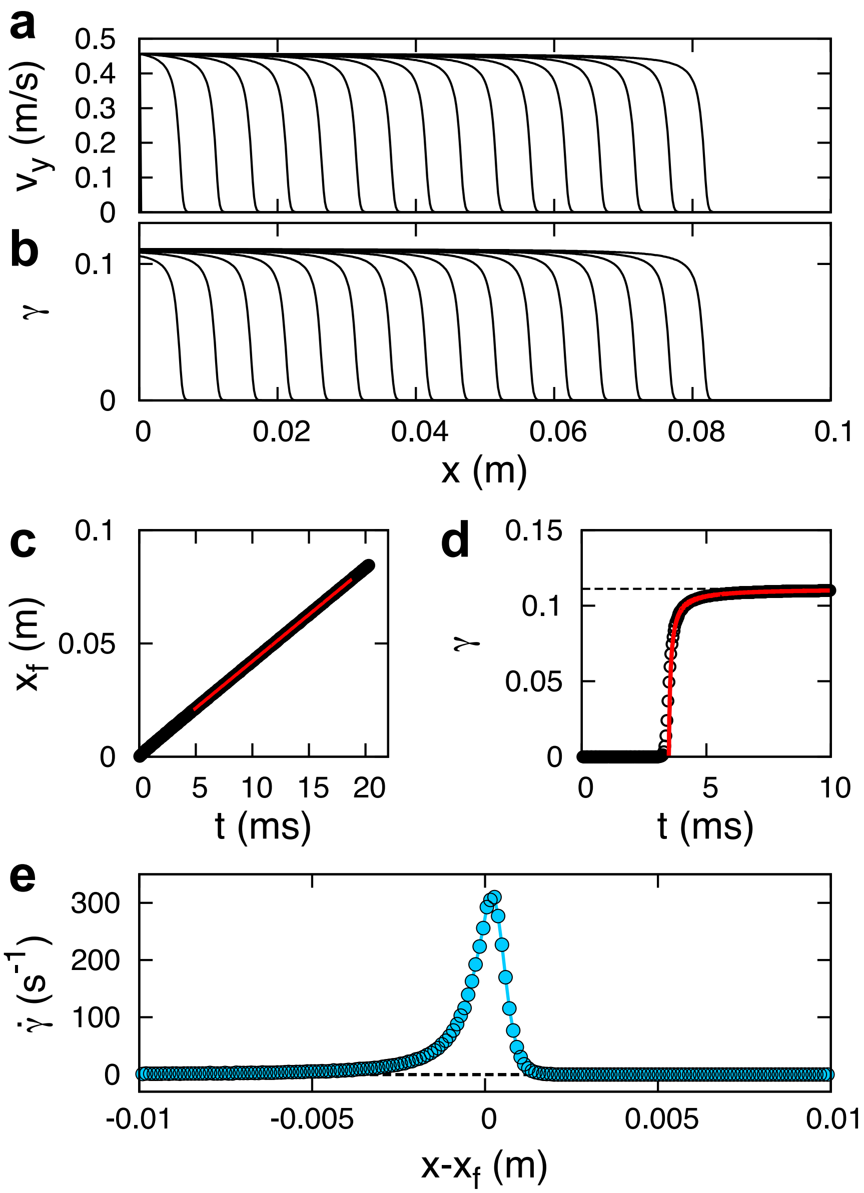

Figure 4.8: Calculated 1D front based on the generalized Wyart-Cates model. The parameters used in the calculation are obtained from Section 4.3. Here we used $\phi = 0.532$ and $U_0 = 0.456$ m/s, so the results can be directly compared with the experiment shown in Fig. 4.2. (a, b) Velocity profiles and accumulated strain γ at different time. (c) Front position x_{f} as a function of time. The red line shows a linear fit. (d) Accumulated strain γ as a function of time in element $n = 80$. The red curve is a fit to a power law. The dashed black line indicates the asymptotic strain. (e) Local shear rate calculated from the mean velocity profile.

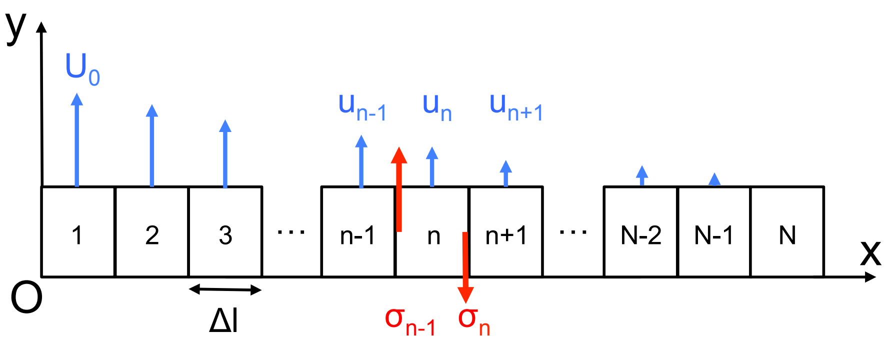

Figure 4.9: Schematic illustration of the model system used for the numerical calculations. The black boxes represent fluid elements, the blue arrows represent the local velocities and the red arrows show the shear stress applied on the left and right boundaries of the n-th element. The boundary conditions are $u_1 = U_0$ and $u_\mathrm{N} = 0$. The width of an element is Δl.

Eqs. 4.8,4.9, and 4.11 lead to a closed relationship for $\Sigma(\gamma, \dot{\gamma}, \phi)$. If the suspension does not jam, we can take the limit $\gamma \to +\infty$ and Eq. 4.9 reverts back to Eq. 1.4 for a steady-state system, as it should.

Furthermore, to study spatially non-uniform situations such as fronts, Newton's second law must be included. The equation of motion is

$$\rho \frac{\partial v_y}{\partial t} = -\frac{\partial \Sigma}{\partial x}, \tag{4.12}$$

where the minus sign is because Σ decreases when x increases, but $\partial v_y/\partial t$ is always positive. Here we calculate the velocity and stress distributions in a one dimensional model system with a finite element method, as illustrated in Fig. 4.9. It is comprised of N elements aligned in the x direction as labeled. Each element is allowed to move in the y direction only. The initial condition is zero velocity and zero strain for every element. At time $t = 0$ s the velocity of the 1st element is set to be U_0 and kept fixed throughout the calculation.

The velocity change of the n'th element Δv_n over a time step Δt is set by the shear stresses σ_{n-1} and σ_n applied on its left and right boundaries, respectively. Using Eq. 4.12, we get

$$\Delta v_n = \frac{\Delta t}{\rho \Delta l}(\sigma_{n-1} - \sigma_n), \tag{4.13}$$

where Δl is the width of individual element. We set $v_1 = U_0$ and $v_N = 0$ throughout the calculation. For the other elements, the velocity $v_n(t)$ is calculated using the forward Euler method. From time step i to $i+1$, we have

$$v_n(i+1) = v_n(i) + \Delta v_n(i). \tag{4.14}$$

The stresses $\sigma_{n-1}(v_{n-1}, v_n)$ and $\sigma_n(v_n, v_{n+1})$ are calculated as

$$\sigma_n = \eta_0 \dot{\gamma}_n \left[1 - \phi/\phi_{\mathrm{J},n}\right]^{-2}, \tag{4.15}$$

where

$$\dot{\gamma}_n = \frac{v_n - v_{n+1}}{\Delta l}. \tag{4.16}$$

In Eq. 4.15, $\phi_{\mathrm{J},n}$ is calculated according to the generalized model discussed above (Eqs. 4.8, 4.9, and 4.10). The increment of strain to calculate $g(\gamma)$ in every step is

$$\gamma_n(i+1) = \gamma_n(i) + \dot{\gamma}_n \Delta t. \tag{4.17}$$

Note that in the transient regime the inertia of the suspension plays a role on the macroscopic scale because of the acceleration term $\partial \mathbf{u}/\partial t$. However, on the length scale of a particle, the Stokes number $St = \rho_p d_p^2 \dot{\gamma}/\eta$ [38] is still at least two orders of magnitude smaller than 1 in our experiments. Some basic parameters are: particle diameter $d_p \approx 15$ μm; density of the particles ρ_p matched to the density of the solvent ρ_l, $\rho_p = \rho_l \approx 1.6 \times 10^3$ kg/m^3; dynamic viscosity of the solvent $\eta \approx 14$ mPas. Even at the maximum shear rate applied in the experiments, $\dot{\gamma} \approx 200$ s^{-1}, we get $St \approx 5 \times 10^{-3} \ll 1$. As a result, the "no inertia" requirement of the original model by Wyart and Cates [41] is still met as far as individual particles are concerned.

On the macroscopic level, when it comes to the effect of inertia in a transient flow, we need to consider both terms in the material derivative of velocity $\partial\mathbf{u}/\partial t + (\mathbf{u}\cdot\nabla)\mathbf{u}$ in the Navier-Stokes equations. In a steady flow $\partial\mathbf{u}/\partial t = 0$, and the effect of inertia is indicated by the Reynolds number Re, which is the ratio between the inertia term $(\mathbf{u}\cdot\nabla)\mathbf{u}$ and the viscous term $\nu\nabla^2\mathbf{u}$. In a transient flow, however, the $\partial\mathbf{u}/\partial t$ term should also be considered. In our case, the time scale T for the front to propagate through its own width Δ is $T \sim \Delta/(kU_0)$, and this time is also comparable to the time for the suspension to accelerate from 0 to U_0. This allows us to estimate the order of each term:

$$\begin{aligned} &O\left(\frac{\partial\mathbf{u}}{\partial t}\right) \sim O\left(\frac{U}{T}\right) \sim \frac{kU_0^2}{\Delta}, \\ &O\left((\mathbf{u}\cdot\nabla)\mathbf{u}\right) \sim O\left(\frac{U^2}{L}\right) \sim \frac{U_0^2}{\Delta}, \\ &O\left(\nu\nabla^2\mathbf{u}\right) \sim O\left(\nu\frac{U}{L^2}\right) \sim \nu\frac{U_0}{\Delta^2}, \end{aligned} \tag{4.18}$$

where U, L, T represent the characteristic speed, length, and time scales, respectively. In our experiments k ranges from ~ 2 to ~ 10 depending on ϕ (Fig. 4.5), thus $\partial\mathbf{u}/\partial t$ is several times larger than $(\mathbf{u}\cdot\nabla)\mathbf{u}$, except for ϕ very close to ϕ_m. Actually, in an ideal one-dimensional system (with this specific geometry), the $(\mathbf{u}\cdot\nabla)\mathbf{u}$ term simply vanishes because the direction along which the flow velocity varies is perpendicular to the direction of the flow itself. So finally, it is a balance between the acceleration term $\partial\mathbf{u}/\partial t$ and the viscous term $\nu\nabla^2\mathbf{u}$, just in this case ν is not a constant. As a result, before the front reaches any outside boundary, the inertia will always play a role. The suspension close to the front is accelerating, thus there must be a stress gradient. This should be a valid result as long as the flow in the suspension is still laminar and no circulation or instability is generated.

Lastly, to better understand the transition from slow U_0 to fast U_0, we look at the evolution of the Σ-$\dot{\gamma}$ relation as γ accumulates, as shown in Fig. 4.10. The Σ-$\dot{\gamma}$ relation for a steady-state system is labeled by the dashed black curve in (d). Since $\phi > \phi_\mathrm{m}$, it intersects

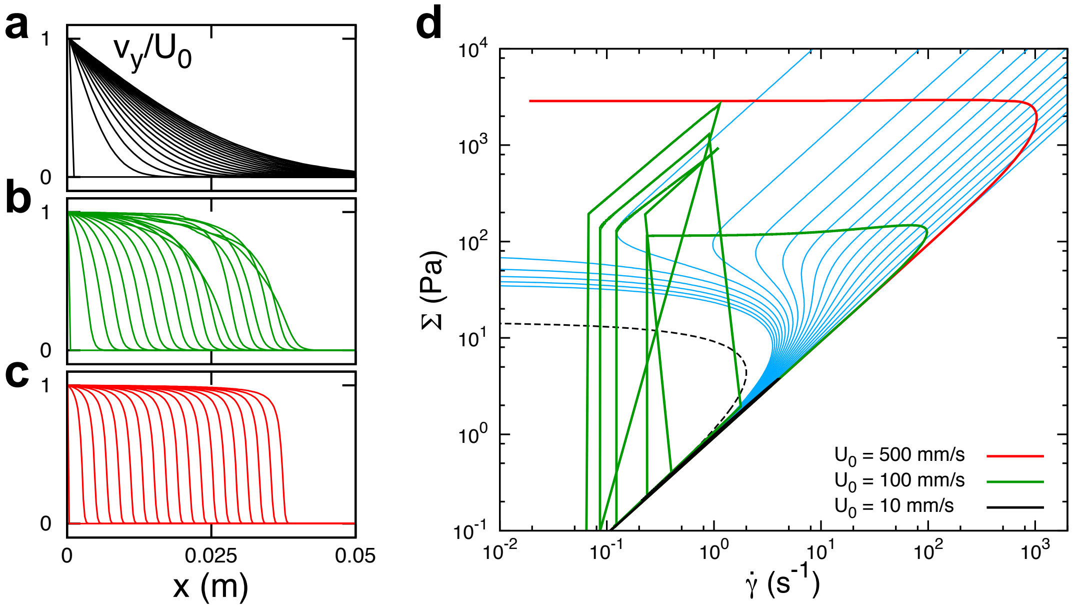

Figure 4.10: (a-c) Velocity profiles at different times for $\phi = 0.521$, $U_0 = 0.01$ m/s (a), 0.1 m/s (b), and 0.5 m/s (c). (a) is in the fluid-like regime, (b) is in the unstable regime, and (c) is in the front regime. (d) Evolution of Σ-$\dot{\gamma}$ at $\phi = 0.521$. The blue curves show the Σ-$\dot{\gamma}$ relations at different γ (starting from zero, with strain increments of 0.0105 between adjacent curves), as predicted by the generalized Wyart-Cates model. The dashed black line corresponds to the relation at steady state ($\gamma \rightarrow +\infty$). The thick black, green, and red lines show the relation between stress and shear rate in element no. 2, calculated numerically for different U_0 as indicated.

with the $\dot{\gamma} = 0 \text{ s}^{-1}$ axis, and does not have an upper branch. However, in the generalized model, since we introduced the g(γ) term, the Σ-$\dot{\gamma}$ relation evolves as γ accumulates. When $\gamma = 0$, the relation between Σ and $\dot{\gamma}$ is linear with a constant viscosity $\eta_0(1 - \phi/\phi_0)^{-2}$. As γ increases, the Σ-$\dot{\gamma}$ curve turns from linear to sigmoidal and finally approaches the black dashed line as $\gamma \to +\infty$.

Given the Σ-$\dot{\gamma}$ relation at any γ, we now discuss, as a specific example, the variation of Σ with $\dot{\gamma}$ in element no. 2 of the numerical 1D system, which we call the "state" of that element. When $U_0 = 0.01$ m/s, the state moves up along the Newtonian-fluid line and then turns back down along an almost identical path as $\dot{\gamma}$ is varied (black line). In contrast, at $U_0 = 0.5$ m/s the stress quickly reaches the upper branch of the sigmoidal curves and stays up there as γ keeps accumulating and $\dot{\gamma}$ slows down. If γ keeps increasing, the shear rate approaches $\dot{\gamma} = 0 \text{ s}^{-1}$. Since Σ stays constant, the viscosity of the suspension diverges as $\dot{\gamma} \to 0$. This then leads to a jammed state (red line). At intermediate U_0 the system can enter a regime where the flows become unstable (green lines). Here the stress reaches the upper branch and forms a plateau at the beginning. However, as γ accumulates and $\dot{\gamma}$ slows down, the state of the element (at that stress level) enters a section of the S-shaped Σ-$\dot{\gamma}$ curves with negative slope. As a consequence, the stress has to jump down to the lower branch. The stress then builds up again and jumps back to the upper branch, and the process repeats.

4.5 Validation of the generalized model

4.5.1 Qualitative predictions of the model

When U_0 (or equivalently the stress Σ) is sufficiently small, $\phi_J \approx \phi_0$ and the viscosity is constant according to Eq.4.11. Injecting this relation into Eq. 4.12 leads to a diffusion equation, and one recovers the usual flow profile for a liquid, evolving with a characteristic length scale $\sqrt{\nu t}$ toward a steady-state shear flow, where ν is the kinematic viscosity. We do recover such a diffusive profile in our finite element implementation of the model, as shown in Fig. 4.10a.

By contrast, if U_0 is large and $\phi > \phi_m$ then there must exist a front separating the solid-like and fluid-like regions. According to Eq.4.3, this front must move at constant speed. This is also recovered in our numerics. Fig. 4.8 shows the numerically obtained velocity (a) and local accumulated strain (b) profiles at different times, as well as the front location x_f (c), the accumulated strain γ at a fixed position(d), and local shear rate $\dot{\gamma}$ (e). The parameters are indicated in the caption, and they were chosen (see below) to correspond to the experimental data in Fig. 4.2, allowing a direct comparison. The model reproduces a front that propagates with a constant speed. The local accumulated strain always approaches a finite value asymptotically, which is in close agreement with observations. The shape of the $\dot{\gamma}(x)$ curve plotted in panel (e) also agrees with the experimental data in several key aspects. The maximum shear rate is obtained near $x = x_\mathrm{f}$, and both curves show asymmetry with respect to $|x| - |x_\mathrm{f}| = 0$: $\dot{\gamma}$ grows quickly as the front approaches, but decays with a tail after the front has passed by. However, the front is sharper than in the experiments, as quantified below.

Finally, at intermediate U_0 the model predicts a regime of instability (not seen in our experiments), exemplified in Fig. 4.10b. After propagating across a certain distance, the shape of the velocity profile in the co-moving frame oscillates back and forth. Such instability is not entirely surprising: for these velocities, the stress Σ lies inside the S-shaped portion of the flow curves (see Section 4.4). In that stress range a complex sequence of instabilities and chaotic behavior in steady-state systems has been reported experimentally [106], which appears to be sensitive to the presence of a free surface that can be deformed. Modeling the front in this velocity regime in the one-dimensional geometry discussed here may thus require to allow for deformation of the free surface. This goes beyond this work, and here we focus on the large U_0 regime.

4.5.2 Quantitative comparison with experiments

There are five parameters in our model, but we can obtain four of them, ϕ_0, ϕ_{m}, η_0, and Σ^*, from steady-state rheology. This is shown in Section 4.3 where we obtain $\phi_0 = 0.593$, $\phi_{\mathrm{m}} = 0.452$, $\eta_0 = 13.6$ mPa·s, and $\Sigma^* = 20.4$ Pa. We are left with a single parameter, $\gamma^* = 0.197 \pm 0.002$, obtained by fitting the front propagation speed k and its inverse γ_∞ at different ϕ, as shown in Fig. 4.5. Interestingly, a threshold strain of approximately 0.2 is also found in regular granular materials [107] and in suspensions [98] as the strain scale below which transient, start-up behavior is observed.

Note that the most important predicted quantities (k and γ_∞) can be estimated analytically in our model in the limit of large U_0. In that case, the stress is large when the front passes through and we may take $f(\Sigma) \approx 1$ in Eq.4.9. Jamming occurs when $\phi_{\mathrm{J}} = \phi$, leading to $g(\gamma^*) = (\phi_0 - \phi)/(\phi_0 - \phi_{\mathrm{m}})$. For our choice of g this implies:

$$\gamma_\infty = \gamma^* \cdot \ln \frac{\phi_0 - \phi_{\mathrm{m}}}{\phi - \phi_{\mathrm{m}}}. \tag{4.19}$$

To further test the model we compute k, γ_∞, Σ and $\dot{\gamma}_{\max}$ across a range of packing fractions ϕ and boundary speeds U_0, and compare the results with experiments directly in Fig. 4.4. As follows from Eq.4.19, we predict k and γ_∞ to be essentially independent of U_0 for large values, and $\Sigma \sim U_0^2$. These predictions match the data very well at each ϕ (except for the largest ϕ values where k shows some decay, presumably induced by the deformation of the free interface, as discussed above).

As shown in Fig. 4.4d, $\dot{\gamma}_{\max}$ obtained from experiments (solid circles) and calculations (hollowed circles) both obey power laws as functions of U_0, and their pre-factors are both relatively ϕ-independent over the range $\phi \in [0.462, 0.532]$ (see Appendix E). However, the model predicts an exponent around 2 instead of 1.5, and the pre-factor is about one order of magnitude larger. For both the transient and steady-state systems (see Section 4.3), the model overestimates the sharpness of the transition from low to high viscosity. Firstly, this could be due to the complexity of cornstarch granules (irregular shape, poly-dispersity, etc.). Secondly, more sophisticated models describing not only the fraction of frictional contacts, but also the evolution of the anisotropy of the contact network with strain, may be required for a more detailed treatment of the front width.

4.6 Conclusions

By studying the rapidly propagating jamming fronts generated when applying a sudden shear, we proposed and validated a phenomenological framework for fluid-solid front propagation in dense particulate suspensions. We found that besides the applied stress, the properties of such fronts are controlled by the local accumulated shear strain as well. These transient, start-up dynamics can be captured by introducing a characteristic strain scale γ^* into a model [41] that describes the steady-state rheology of shear-thickening suspensions. Despite its simplicity, this extended model gives very good agreement with the experiments, quantitatively reproducing the dependence of the normalized fronts speed k and of the locally accumulated shear strain γ_∞ on packing fraction ϕ. It also predicts correctly the qualitative dependence on system and forcing parameters of the maximum shear rate $\dot{\gamma}_{\mathrm{max}}$ inside the front.

Importantly, the generalized model introduced here establishes a direct link between the steady-state and transient behaviors in dense suspensions. It shows that to obtain jamming fronts, the packing fraction of the suspension must be above the frictional jamming packing fraction ϕ_{m}. In the range between ϕ_{m} and the frictionless jamming packing fraction ϕ_0, the suspension will evolve into a state that jams at high stress, but can still flow at low stress.

While we discussed the model in its simplest form, appropriate for a semi-infinite 1D system, the same ideas and numerical approaches should allow for several extensions. This includes accounting for the presence of walls (which can take up large stresses once reached by the fronts) as well as extension to 2D or 3D systems (where the fronts propagate with different speeds in the directions along the applied forcing and perpendicular to it [57, 97, 98]).

CHAPTER 5

RHEOLOGY IN THE SHEAR JAMMING REGIME

In this Chapter, we are going to compare steady-state rheology in a narrow gap and transient flows in a wide gap, for suspensions in the shear jamming regime. With a quasi-1D transient shear flow, we can perform stress-controlled rheology experiments that allow the suspensions to approach steady shear jammed states. Another major prediction of the model by Wyart and Cates [41] - a stress threshold above which the suspension develops a non-zero shear modulus - is tested quantitatively in experiments for the first time.

5.1 Limitations of narrow-gap steady-state rheology

Let us call a point on a shear stress (Σ) - shear rate ($\dot{\gamma}$) plot a "state" of the suspension. According to Wyart and Cates [41], steady-state rheology of suspensions can be described by two parameters Σ and ϕ. Some predicted Σ-$\dot{\gamma}$ curves in the shear jamming regime are shown in Fig. 5.1(a), where ϕ is above the frictional jamming packing fraction ϕ_{m}. At low stress, the curves grow as $\Sigma \propto \dot{\gamma}$, which is the expected behavior of Newtonian fluids. At high enough stress, the curves start to bend towards low $\dot{\gamma}$, and eventually intersect with the vertical axis where $\dot{\gamma} = 0\ \mathrm{s}^{-1}$. At the intersections, the suspensions can sustain non-zero shear stress at zero shear rate, and therefore they must have developed a non-zero shear modulus. We call the stress at the intersection the onset stress of shear jamming Σ_{SJ}. In principle, a higher shear stress can be applied on the jammed solid, but it does not flow until Σ exceeds its yield stress. For example, when sheared by an incremental Σ, the state of a suspension with $\phi = 0.496$ should move up along the green curve shown in Fig. 5.1(a). After $\dot{\gamma}$ decreases to zero, the jammed state will stay on the $\dot{\gamma} = 0\ \mathrm{s}^{-1}$ axis, until it yields at a higher stress.

However, when these model predictions are compared to experimental results, we can see obvious deviations in Fig. 5.1(a). The rheology experiments were performed with a parallel-

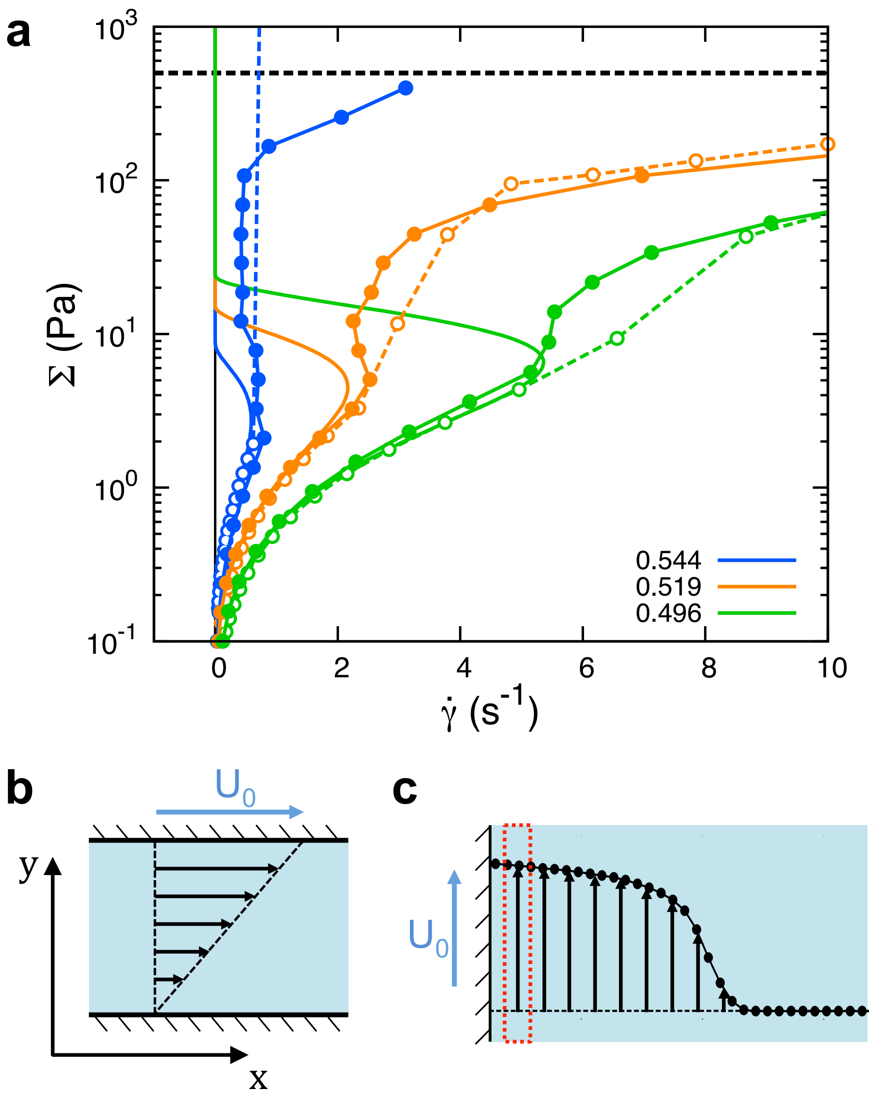

Figure 5.1: (a) Relation between shear stress Σ and shear rate $\dot{\gamma}$ for suspensions in the shear jamming regime. Solid curves show predictions of the Wyart-Cates model. Circles show data collected with cornstarch suspensions under stress controlled conditions. Dashed lines show results with the same samples under conditions where the shear rate was controlled. (b, c) Comparison between narrow-gap rheology (b) and wide-gap shear flow in 1D (c).

plate geometry, and the tested samples were cornstarch suspensions. At each ϕ, we ran both stress controlled and rate controlled experiments. In the stress controlled experiments, we applied a constant torque on the upper plate at each data point, and in the rate controlled experiments, the plate rotated at constant angular velocities. Compared to rate-controlled rheology, data obtained from stress-controlled experiments do bend more towards low $\dot{\gamma}$, but none of them keep decreasing or intersect with the $\dot{\gamma} = 0$ s^{-1} axis. We have confirmed in Chapter 4 that all three suspensions shown here can be jammed dynamically under shear. The question thus arises: Why can't they be jammed with steady-state rheology?

Rheology tests can be performed with different geometries, and among them the ones used most often are parallel plates, cone and plate, and concentric cylinders (Couette cell). For all three geometries, the basic idea is similar: the sample is placed inside a narrow gap, and sheared towards one direction, as schematically illustrated in Fig. 5.1(b). For Newtonian fluids, a linear velocity profile is expected, but for suspensions, this is not always the case [22, 61]. To obtain the correct viscosity from such measurements, certain conditions must hold:

1. The flow is in steady-state, so that $\partial \mathbf{u}/\partial t = 0$.
2. The shear rate and shear stress in the bulk have a well defined spacial profile, so it can be calculated from the conditions applied at the boundaries.
3. There is no slip at any solid boundaries.

For suspensions at high ϕ, these conditions are often violated. As shown by Hermes *et al.* [106], in this regime the flow never settles down to a steady flow, and boundary slip has been observed extensively in experiments [61, 25, 108]. As a result, in a "stress controlled" experiment, though a constant torque is applied on the solid boundary, the stress in the tested sample may vary from place to place, and from time to time. Therefore, with narrow-gap rheology experiments, it is difficult to obtain a shear jammed state in the first place, and even if it is achieved, we may not be able to tell it from the measured Σ-$\dot{\gamma}$ curve.

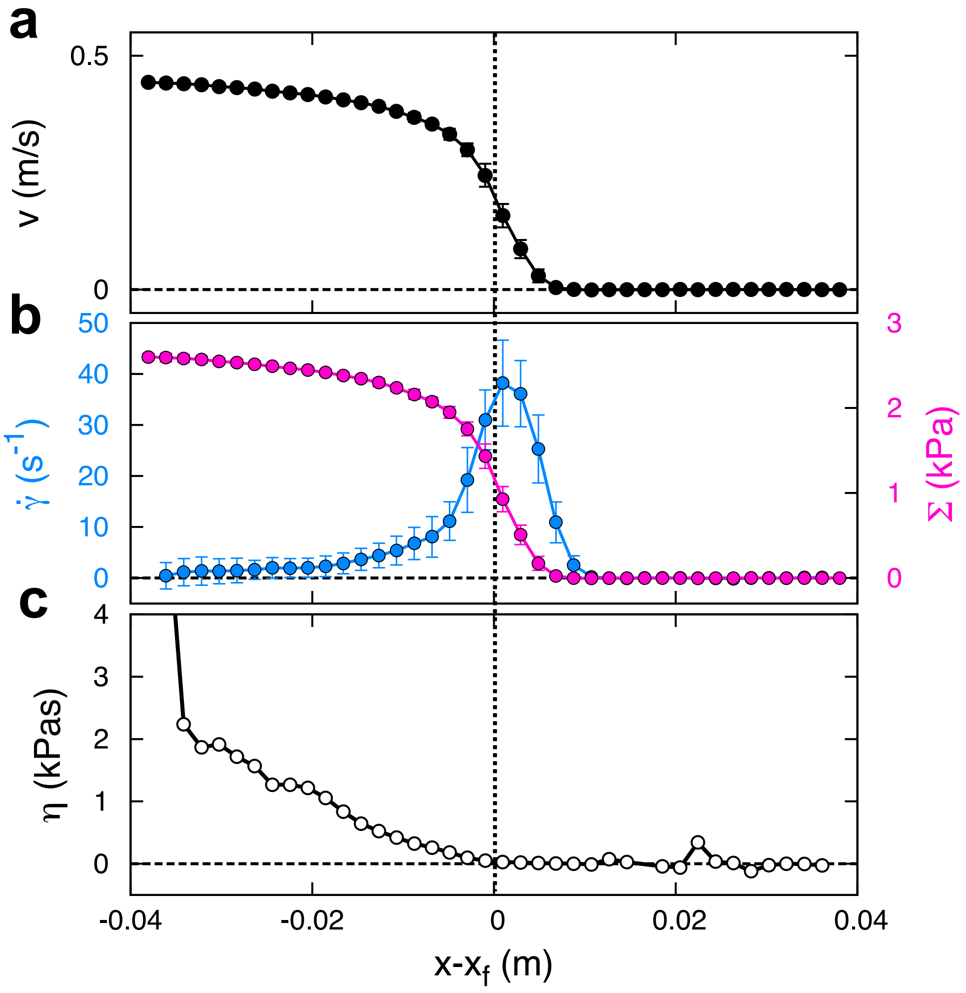

Figure 5.2: (a) Collapsed velocity profile $v(x-x_{\mathrm{f}})$ at $\phi = 0.532$. (b) Shear stress Σ (magenta) and shear rate $\dot{\gamma}$ (blue) calculated from $v(x-x_{\mathrm{f}})$. (c) Local viscosity $\eta = \Sigma/\dot{\gamma}$.

5.2 Steady-state rheology using one dimensional transient flows

Now we introduce a wide-gap shear setup, as sketched in Fig. 5.1(c), with which we can study how dense suspensions evolve towards a steady shear jammed state. When the solid boundary on the left starts to move with a constant speed U_0, a one dimensional (1D) transient flow will develop across the initially quiescent suspension. For suspensions at $\phi > \phi_{\mathrm{m}}$, a shear jamming front can be generated when U_0 is above a certain threshold (Chapter 4). Details on the experimental procedures and properties of the shear fronts are discussed in Chapter 4. Some significant features of the fronts are: The velocity profile of the flow has an approximately invariant shape, so to represent the flow, we can write

$$f(x, t) = f(x - U_{\mathrm{f}}t), \tag{5.1}$$

where f can be velocity v, shear stress Σ, shear rate $\dot{\gamma}$, and so on. The state of an element at any position x will be the state of the element on its right at $(x + U_{\mathrm{f}}\Delta t)$ after time Δt. We define the front position x_{f} as where $v = 0.45U_0$, which is also approximately where $\dot{\gamma}$ peaks. The front propagates with a constant speed $U_{\mathrm{f}} \equiv kU_0$, where k is named the dimensionless front propagation speed. At high enough U_0, k reaches a plateau k_{p} and becomes independent of U_0. What controls k is the accumulated shear strain to jamming $\gamma_\infty(\phi)$, which is not necessary for describing steady-state rheology.

In such a 1D linear system, the equation of motion is Eq. 4.12. This means that the viscous stress in the system is always balanced by the acceleration of the suspension. It allows us to obtain local shear stress without measuring any force: we can just calculate the stress needed for the suspension to accelerate. From Eq. 5.1 and Eq. 4.12, we get

$$\Sigma = \rho U_{\mathrm{f}} v, \tag{5.2}$$

thus the local shear stress has the same shape as the velocity profile, but with a pre-factor ρU_{f}. The mean velocity profile $v(x - x_{\mathrm{f}})$ is shown in Fig. 5.2(a). At each time, $v(x, t)$ is shifted so that the front position x_{f} becomes 0, then they are averaged up to get $v(x - x_{\mathrm{f}})$. The corresponding shear stress is shown in Fig. 5.2(b). As $(x - U_{\mathrm{f}}t) \to -\infty$, $v \to U_0$, and Σ approaches a constant stress Σ_0, which has been shown in Eq. 4.3.

The local shear rate $\dot{\gamma}$ calculated from the averaged velocity profile is also shown in Fig. 5.2(b). In this case the shear rate is the slope of v: $\dot{\gamma} = |\partial v/\partial x|$. Because it is a 1D system, we take $\dot{\gamma}$ to be positive for simplicity. We can see that beyond the front $(x > x_{\mathrm{f}})$, both Σ and $\dot{\gamma}$ increases. However, behind the front $(x < x_{\mathrm{f}})$, Σ keeps increasing and approaches a finite value $\rho k U_0^2$, while $\dot{\gamma}$ decreases and approaches zero as time goes to infinity. This means that the viscosity $\eta = \Sigma/\dot{\gamma}$ increases dramatically behind the front, as shown in Fig. 5.2(c). Note that for the exemplary suspension at $\phi = 0.532$, the solvent viscosity was $\eta_0 = 11 \times 10^{-3}$ Pas, and the Newtonian viscosity of the suspension was $\eta_{\mathrm{N}} = 1.3$ Pas. At only 2 cm behind x_{f}, the viscosity of the suspension was already about 10^5 times more viscous than the solvent, and almost 10^3 times more viscous than η_{N}. The exact shape of the velocity profile is controlled by how the suspension shear thickens. But different from shear thickening at steady-state, where η increases with Σ, in the case of transient flow, η increases because of the accumulation of γ as well. Moreover, compared to DST, where we have $\eta \propto \Sigma$, the shear thickening here is beyond "discontinuous", because now as $\Sigma \rightarrow \Sigma_0$, η grows up almost vertically. If we look at an element close to the solid boundary, as labeled by the dashed red box in Fig. 5.1(c), as time goes on, the end state will be a shear jammed state where the viscosity diverges and a non-zero shear modulus is developed ($\dot{\gamma}|_{t\rightarrow+\infty} \rightarrow 0$).

This provides a second path to reach a shear jammed state. As shown in Chapter 4, for transient flows the viscosity is a function of the accumulated strain γ as well as ϕ and Σ. In the steady-state, DST happens after Σ exceeds a threshold stress, while for transient flows, both Σ and γ need to be high enough for the suspension to jam. Consequently, a shear jammed state does not have to be reached by climbing up along the axis $\dot{\gamma} = 0$ s^{-1} following the steady-state Σ-$\dot{\gamma}$ curve in Fig. 5.1. In Fig. 5.3, we plot the Σ-$\dot{\gamma}$ curves obtained from the velocity profiles of the front at different U_0. These curves are obtained with two methods: The solid points are from the mean velocity profiles $v(x - x_{\mathrm{f}})$. Σ and $\dot{\gamma}$ are extracted the same way as in Fig. 5.2. The open circles are obtained by first calculating Σ and $\dot{\gamma}$ with the velocity profiles at each time, and then averaging Σ and $\dot{\gamma}$. The two methods match well, especially at fast U_0. Compare to the Σ-$\dot{\gamma}$ relation at steady-state (solid black line), for transient flows each curve makes a detour into the higher $\dot{\gamma}$ territories before Σ approaches its asymptotic limit. Identical to what we have seen in Fig. 5.2, first both Σ and $\dot{\gamma}$ grow, then Σ approaches a constant value Σ_0, while $\dot{\gamma}$ decays towards zero.

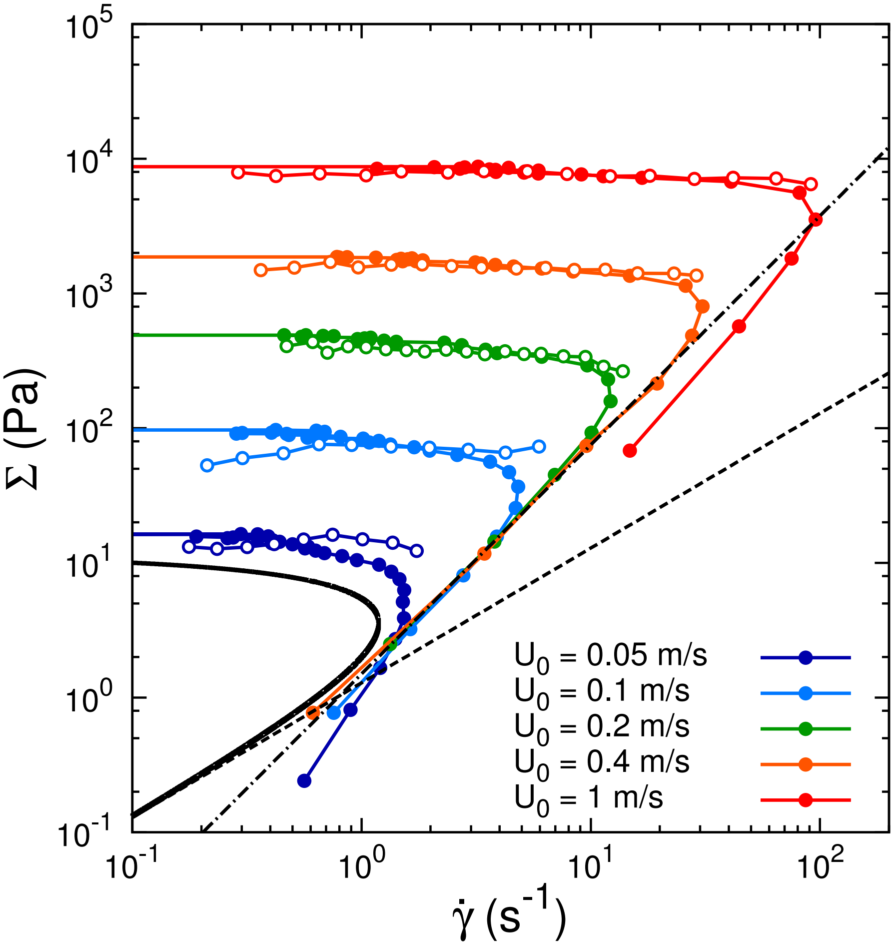

Figure 5.3: Σ-$\dot{\gamma}$ curves obtained for $\phi = 0.532$ with different boundary speed U_0. The solid circles represent data obtained from the collapsed velocity profiles as shown in Fig. 5.2. The open circles are obtained by calculating the local shear rate and shear stress at different times, and then doing the average. The solid black curve shows the prediction of the Wyart-Cates model. The dashed black line shows $\Sigma = \eta_{\mathrm{N}}\dot{\gamma}$. The dash-dot black line is $\Sigma \propto \dot{\gamma}^{1.7}$.

Note that though the Σ-$\dot{\gamma}$ curve obtained form the transient flow at slower U_0 looks close to the steady-state curve as far as shape is concerned, they are different fundamentally. For any point on the black curve, the accumulated strain γ can keep growing without changing the property of the suspension, since it is in steady-state. In contrast, on a transient Σ-$\dot{\gamma}$ curve, each point corresponds to a certain γ. When the accumulated strain increases, the state evolves along the curve accordingly.

5.3 Boundary of shear jamming in suspensions

We now use the new method developed in Section 5.2, which probes a suspension in a stress-controlled manner, to map out the onset stress Σ_{SJ} of steady-state shear jamming. As Eq. 4.3 shows, when $\dot{\gamma} \to 0$, Σ approaches $\Sigma_0 \propto U_0^2$. Therefore by driving the boundary at different speeds U_0, we can control the stress applied on the suspension, provided the spatial extent of the system is large enough so that an asymptotic steady state can be reached, as shown in Fig. 5.3. This allows us to systematically probe how the boundary of shear jamming depends on applied shear stress.

To quantify this boundary, we look at the relation between the dimensionless front propagation speed k and the corresponding boundary stress Σ_0 obtained from plots like Fig. 5.3 for each ϕ. To compare suspensions prepared with different ϕ, we normalized k using the plateau value $k_{\mathrm{p}}(\phi)$, which is shown in Fig. 4.5. The relation between k/k_{p} and Σ_0 is presented in Fig. 5.4(a). In general, as Σ increases, k/k_{p} grows from 0 to 1. But for suspensions at higher ϕ, k starts to increase at a lower Σ, and vice versa. There are three stress scales in the system: Σ^*, Σ_{DST}, and Σ_{SJ}. Among them, Σ^* represents the stress at which the interaction between particles changes from lubrication to direct contact, which is thought to be independent of ϕ. The Wyart-Cates model [41] provides predictions for $\Sigma_{\mathrm{DST}}(\phi)$ (Section 4.3) and $\Sigma_{\mathrm{SJ}}(\phi)$. It turns out that the predicted Σ_{SJ} works well collapsing the data, as

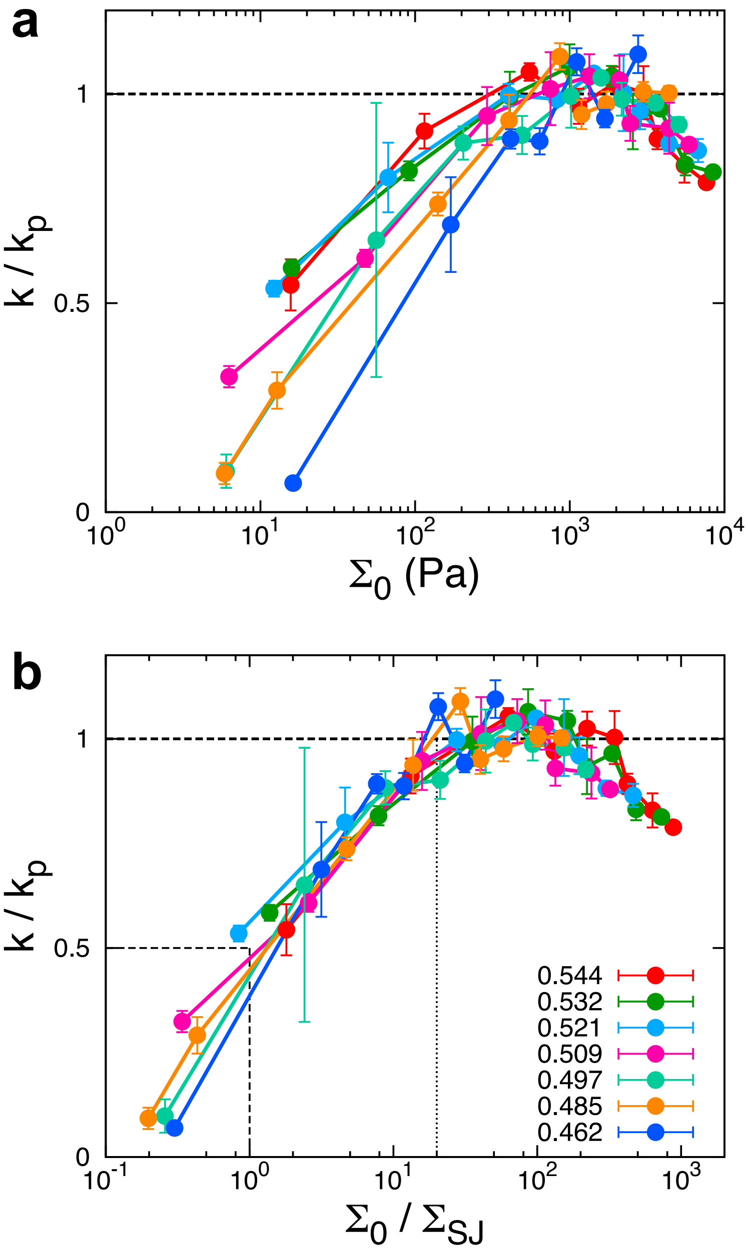

Figure 5.4: Normalized dimensionless front propagation speed k as a function of shear stress Σ for different packing fractions ϕ. (a) k/k_p as a function of Σ. (b) k/k_p as a function of Σ normalized by the value for Σ_SJ predicted by the Wyart-Cates model [41].

shown in Fig. 5.4(b), where Σ_{SJ} is given by

$$\Sigma_{\mathrm{SJ}} = -\Sigma^{*}\ln\left(\frac{\phi - \phi_{\mathrm{m}}}{\phi_{0} - \phi_{\mathrm{m}}}\right). \tag{5.3}$$

From the data collapse, we can see that when $\Sigma_0 > \Sigma_{\mathrm{SJ}}$, $k/k_{\mathrm{p}} > 1/2$. A front that propagates outward, away from the shearing boundary can be formed in this regime, but its relative propagation speed has not reached the maximum yet. This means that we can not tell if the final state will be a shear jammed state or a DST state. However, when k/k_{p} reaches 1, which in that figure occurs for $\Sigma \approx 20\Sigma_{\mathrm{SJ}}$, the suspensions will definitely transform into a shear jammed state after the front has passed by.

The k-Σ_0 relationship allows us to map out the boundary of the shear jamming regime in the state diagram for dense cornstarch suspensions. Here we compare the boundary obtained from transient flows with the prediction of the Wyart-Cates model [41] and previous experimental measurements performed under conditions of steady-state shearing [25]. In Fig. 5.5, the three solid curves show boundaries predicted by the model. The blue curve is the onset of DST, which has been extensively tested by our steady-state rheology experiments (black data points, see Section 4.3), by simulations [37, 39], and by other experiments [48, 106]. The solid green curve is Σ_{SJ} from Eq. 5.3, which up to now has not been tested quantitatively by experiments. The light colored data points are from experimental measurements with a wide-gap Couette cell [25]. In that experiment, shear jamming was determined by dropping a small metal sphere on the surface of the suspension while it was continually sheared between the concentric cylinders. If the sphere did not sink below the surface, the suspension was labeled jammed; if the sphere sank, the suspension was labeled as not jammed. The onset stress of shear jamming obtained from such measurements is the boundary between the light red (DST) and light green (shear jammed) solid circles. Limited by the relatively low sensitivity of this method, the measured boundary is considerably higher than the prediction of the model.

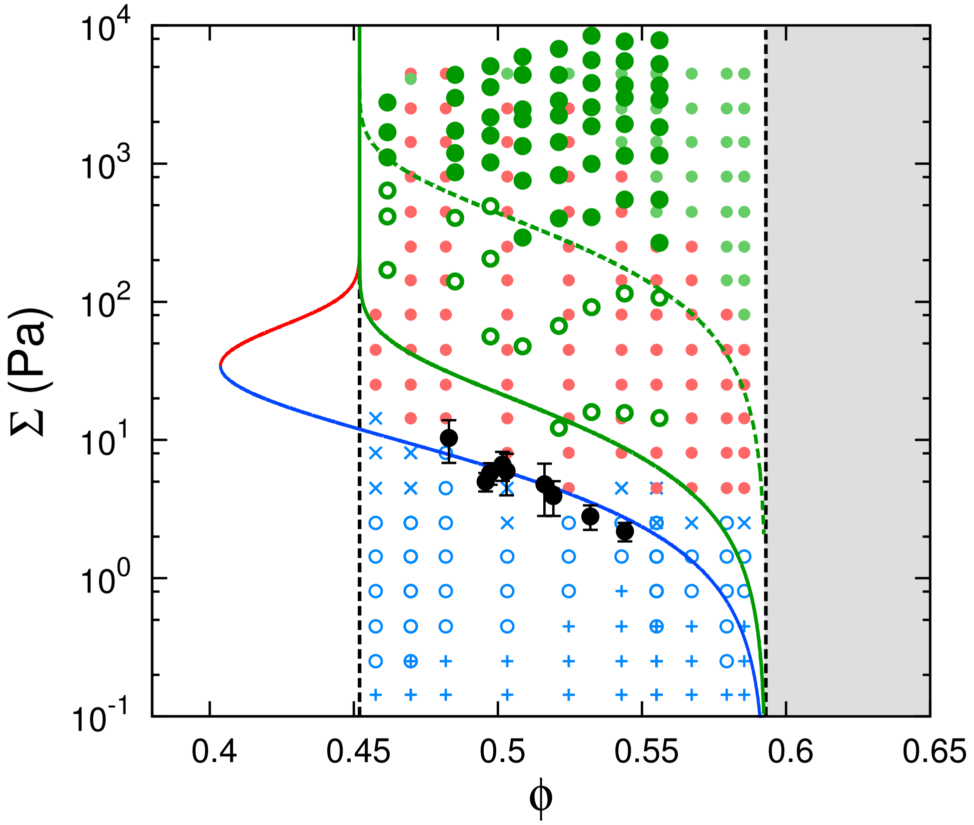

Figure 5.5: State diagram for cornstarch suspensions. The black circles are the onset stress of DST obtained from steady-state rheology experiments. The dark Green circles are obtained from wide-gap transient flows. Among them, the solid points are in the regime where k and γ_∞ are invariant with U_0, and the open circles are in the transition regime. The light colored points are from [25], where shear jamming was measured with a different method. From bottom to top the symbols indicate, with increasing stress, shear thinning (+), Newtonian (○), CST (x), DST (light red), and shear jamming (light green). The two dashed black lines label ϕ_{m} (left) and ϕ_0 (right), respectively, as obtained from steady-state rheology experiments. The solid curves are boundaries predicted by the Wyart-Cates model: blue is Σ_{DST}, green is Σ_{SJ}, and red is the stress at the upper turning points of the sigmoidal Σ-$\dot{\gamma}$ curves in the DST regime.

Our measurements at different ϕ are shown by the dark circles in Fig. 5.5. According to Fig. 5.4, the predicted $\Sigma_{\mathrm{SJ}}(\phi)$ happens to overlap with the iso-contour of $k/k_{\mathrm{p}} = 1/2$. Above $20\Sigma_{\mathrm{SJ}}(\phi)$, which is shown by the dashed green curve in Fig. 5.5, k/k_{p} saturates. We label the points between Σ_{SJ} and $20\Sigma_{\mathrm{SJ}}$ with open circles, and the points above $20\Sigma_{\mathrm{SJ}}$ with solid circles. The onset stress of shear jamming is no higher than the dashed curve. What the means is that, compared to Ref. [25], our new method provides a more accurate determination of $\Sigma_{\mathrm{SJ}}(\phi)$, especially in the low ϕ regime. What we see is that the boundary of the shear-jammed regime is not sharp, but resembles a smooth cross-over that spans roughly one decade in applied shear stress Σ_0, corresponding to a factor of 2 in front propagation speed, from $k/k_{\mathrm{p}} = 0.5$ to $k/k_{\mathrm{p}} = 1$.

5.4 Conclusions

In this Chapter we noted that conventional steady-state rheology with narrow-gap geometries has limitations while testing suspensions in the shear jamming regime. To obtain flow curves for suspensions in this regime, we developed a new method that takes advantage of the transient shear fronts in a one-dimensional wide-gap setup. As the front propagates, the dense suspension behind the front will evolve towards a shear jammed state, and the stress of this jammed state can be controlled by the speed of the shearing boundary. With this experiment, we were able to map out the onset stress of shear jamming for different packing fractions and, for the first time, compare it in a quantitative way to model predictions.

CHAPTER 6

CONCLUSIONS AND OUTLOOK

In this thesis, we presented a detailed investigation of the dynamics of dense particulate suspensions, focusing in particular on the transient dynamics. To achieve a better understanding of the rapidly evolving flows in optically opaque fluids like dense suspensions, we developed a technique to image flows at high frame rate (up to 10,000 frames per second) with ultrasound. Combining speed of sound measurements and high-speed imaging techniques, our experiments demonstrated that ultrasound can be a powerful tool for studying suspensions. In particular, with the help of ultrasound we were able to develop a new and much more detailed understanding of impact-activated solidification. Previously work had shown that impact at the surface of dense suspensions generates a front that propagates fast into the bulk, and transforms the material from a fluid-like state into a solid-like state in its wake. We achieved the first direct observation of such fronts in a three dimensional system. Our speed of sound measurements show that, within the experimental error, there is no detectable increase in packing fraction behind the front, which rules out a model that relates the front propagation speed to (isotropic) jamming via densification [52, 58]. From the measured flow fields, we show that the formation of the fronts is closely related to a narrow, propagating zone of high shear rate. Based on these observations, we conclude that impact-activated fronts are actually shear fronts. We furthermore show that the front propagation speed is controlled by the accumulated strain needed for shear jamming. We explain the measured anisotropy in the front propagation speeds in the directions along and transverse to the impact by tracing its origin to the differences in the mode of shear experienced. To understand this shear front even better and model it quantitatively, we performed further experiments in a quasi-one-dimensional system, which is arguably the simplest geometry. In this geometry, we confirmed that the dimensionless front propagation speed is the inverse of the accumulated strain required to shear jam the suspension. This strain scale is the key that links steady-state rheology to transient flows. To show this we generalize the Wyart and

Cates model [41] that was developed to describe steady-state conditions by introducing a strain term. The generalized model is validated by our experiments, and it matches the data very well both qualitatively and quantitatively. Lastly, we extend the links between steady-state rheology and transient flows even further by realizing that transient flows can be used to study steady-state shear jamming, which is difficult, if not impossible, with conventional rheology experiments. We show that by using an experimental setup that corresponds to a shear flow across a sufficiently wide gap, we can drive suspensions to evolve towards shear jammed states at precisely controlled stress levels. Using this new method, we then are able to map out the onset stress for shear jamming in a state diagram for dense suspensions.

Particulate suspensions are complex systems that involve interactions on a wide range of length scales. On the macroscopic level, the characteristic length scales are of order 1 mm. For example, in standard steady-state rheology, the gap size ranges from 10^{-4} to 10^{-2} m, and for shear fronts, the characteristic length scale is the front width, which is approximately 10^{-3} - 10^{-2} m. A smaller length scale that matters is the particle size, which is in the range of 10^{-6} - 10^{-4} m. Parameters on this scale include particle size, shape, and their spatial configuration, which all control the mechanical properties of the suspension. At an even smaller length scale, we have contact interactions between two particles, which is of order 10^{-9} m or smaller. Among different contact interactions between particles, a crucial one is "friction", which can be related to the frictional coefficient of the materials, the surface roughness of particles, the interactions between polymer brushes on the particle surfaces, or chemical interactions such as hydrogen bonds [45].

Comparatively, phenomena on the macroscopic length scales are the most well understood. Over the years, a huge amount of data have been collected by rheology experiments, on shear thinning, shear thickening, and recently, shear jamming. A separation of length scales allows us to model the macroscopic flows without considering details on the micron and nanometer levels. Till now, the mean field theory by Wyart and Cates and our generalization of this model work reasonably well. With the state diagram $\eta(\phi, \Sigma)$, which has as few as four parameters (solvent viscosity η_0, frictionless and frictional jamming packing fractions ϕ_0 and ϕ_{m}, and a threshold stress scale Σ^*) all measurable on a rheometer, one can predict behaviors of suspensions under different steady-state driving conditions. Shear fronts constitute a clean, exemplary system that helps us reveal the links between steady flows and transient flows in such shear thickening fluids. With one more parameter, a threshold strain scale γ^*, qualitative or even quantitative predictions can be made. However, there are still many other transient phenomena that need to be included to enrich this model. In principle, our current model in one-dimension can be extended to three dimensions by considering the tensorial forms of strain and stress. Oscillatory shear is another good model system to study transient flows, especially for investigating the effect of strain. Last but not least, as discussed in Chapter 5, standard rheology techniques have certain limitations in the jammed regime. We demonstrated one new experimental method to overcome certain of these limitations, but clearly there is much need to develop additional approaches.

When it comes to the micron and nanometer scales, there still is much more to explore. The phenomenological models on macroscopic scales rely on the state diagram, but the parameters that are necessary to map out the diagram are all controlled by properties on the microscopic level. Understanding how microscopic interactions affect macroscopically measurable parameters will not only lead to deeper and richer physics, but also guide us to design and engineer suspensions with expected properties. Currently, some of those links from micro to macro are still missing. For example, we expect that γ^* is related to rearrangement of particle configuration in space, but till now most experiments that explore this relation are performed with quasi-static dry granular systems in two dimensions. To understand how microscopic properties affect macroscopic behaviors of real suspensions, we need to perform experiments on the microscopic level, with techniques such as confocal microscopy, x-ray scattering or tomography, atomic force microscopy (AFM), and so on, and combine them with rheolgoy experiments. Simulations are good tools for studying the effect of particle configurations, but until now numerical approaches have been mostly focusing on steady-state systems, where a relatively small system with several thousand particles will be sufficient. When it comes to transient phenomena the system might need to be much larger because of the emergence of other longer length scales such as the front width, and consequently the computation will be more expensive.

In recent years, research on dense suspensions has progressed dramatically. New ideas are emerging, more powerful frameworks are being established, and bigger pictures are being drawn that need to be tested. The result is a rich field with tremendous opportunities as well as challenges, and surprises might appear on many different length scales.

APPENDIX A

EFFECTIVE DENSITY OF NON-DENSITY MATCHED SUSPENSIONS

For non-density matched suspensions, many models have been proposed for their effective density ρ_{eff} [109, 85, 110, 111, 112, 113]. Among them, Ament (1953) [85] better describes the experimental data [94, 114]. To model sound propagation there are two important length scales: the wavelength of the ultrasound λ and the length scale of the viscous layer δ. All the models described here only work in the regime where λ is much larger than the particle radius a. The thickness of the viscous layer can be expressed as

$$\delta = \sqrt{\frac{2\eta}{\omega\rho_{\text{l}}}}, \tag{A1}$$

where $\omega = 2\pi f$ is the angular frequency of the ultrasound wave and η and ρ_{l} are the dynamic viscosity and density of the liquid in the suspension, respectively. The ratio a/δ is analogous to the Reynolds number. The system is in the inertial regime when $a/\delta \gg 1$ and in the Stokes regime when $a/\delta \ll 1$. In our experiments the suspensions were in the inertial regime.

Ament (1953) [85] derived a function for ρ_{eff} by considering the relative motion of particles and liquid in non-density matched suspensions. He got

$$\rho_{\text{eff}} = \bar{\rho} - 2(\rho_{\text{s}} - \rho_{\text{l}})^2\phi(1-\phi)\frac{Q}{Q^2+U^2} \tag{A2}$$

where $\bar{\rho}$ is the mean density shown in Eq. 2.4, $Q = 2(\rho_{\text{s}} - \rho_{\text{l}})(1-\phi) + (\frac{9}{2}\frac{\delta}{a} + 3)\rho_{\text{l}}$, $U = \frac{9}{2}\rho_{\text{l}}[\frac{\delta}{a} + (\frac{\delta}{a})^2]$. By plugging $\bar{\kappa}$ and ρ_{eff} into Eq. 2.2 we can obtain the speed of sound c.

APPENDIX B

PREPARATION OF SUSPENSIONS

The solid particles we used to make suspensions were cornstarch granules (producers: Ingredion and Roquette). They are non-spherical poly-disperse particles whose diameter ranges from 5 to 30 μm [52, 74], with an average of about 15 μm [115]. The density of cornstarch particles was $\rho_{\mathrm{cs}} = (1.63 \pm 0.01) \times 10^3$ kg/m^3 measured by density matching. Detailed procedure can be found in [114]. The suspending solvent was a mixture of caesium chloride (CsCl), glycerol, and deionized water. The mass ratio between glycerol and water in the solvent controls its viscosity. The density of the solvent was $\rho_{\mathrm{l}} = 1.62 \times 10^3$ kg/m^3, which was matched to ρ_{cs} to prevent sedimentation.

When a suspension was made, we mixed m_{cs} grams of cornstarch particles with m_{l} grams of the solvent. The dry cornstarch particles were stored in a temperature and humidity controlled environment at 22.5 ± 0.5°C and $44 \pm 2\%$ relative humidity (RH), so they initially contained some moisture [74]. Therefore, the m_{cs} grams of cornstarch dispersed into the solvent actually contained $(1 - \xi)m_{\mathrm{cs}}$ grams of cornstarch "material" and ξm_{cs} grams of water. At 44% RH, the moisture content (mass fraction) ξ is approximately 13% ± 1% according to literature [74, 77]. The "material" volume fraction ϕ_{M} for cornstarch is

$$\phi_{\mathrm{M}} = \frac{(1-\xi)m_{\mathrm{cs}}/\rho_{\mathrm{cs}}}{(1-\xi)m_{\mathrm{cs}}/\rho_{\mathrm{cs}} + m_{\mathrm{l}}/\rho_{\mathrm{l}} + \xi m_{\mathrm{cs}}/\rho_{\mathrm{w}}}, \tag{B1}$$

where "w" represents water. Here ϕ_{M} specifically is the fraction of the volume occupied by the impermeable part of the amylose/amylopectin network that comprises the cornstarch particles. The mean density of the suspension $\bar{\rho}$ is also affected by the moisture content, and this in turn affects ρ_{eff} (Eq. A2). If we assume that the water initially contained within the cornstarch particles completely mixes with the solvent, then

$$\bar{\rho} = \frac{m_{\mathrm{cs}} + m_{\mathrm{l}}}{(1-\xi)m_{\mathrm{cs}}/\rho_{\mathrm{cs}} + m_{\mathrm{l}}/\rho_{\mathrm{l}} + \xi m_{\mathrm{cs}}/\rho_{\mathrm{w}}}. \tag{B2}$$

As discussed in Section 2.4, the volume fraction ϕ occupied by the fully soaked particles is $\phi = \phi_{\mathrm{M}}/(1-\psi)$ (Eq. 2.6), where $\psi = 0.31$ is the porosity of the cornstarch granule. In this thesis, the packing fractions we report are all calculated using Eq. B1 and Eq. 2.6.

After mixing the particles and solvent, we left the suspension sit still for approximately 2 hours before performing experiments to allow full wetting of the particles and for big air bubbles to escape. However, for ultrasound visualization, there are still too many bubbles after resting, as shown in Section 2.6. Therefore, the suspensions were debubbled before measurements. To prevent solvent evaporation during debubbling, we placed the mixed suspension samples into 10 mL or 50 mL syringes, sealed the nozzles with rubber septa, and withdrew the plungers to generate low pressure in the syringes. The walls of the syringes were tapped to liberate trapped bubbles. This method has proven effective in getting rid of bubbles in suspensions as shown in Section 2.6.

The debubbled suspensions are almost completely black in the ultrasound B-mode images. They were used directly in the speed of sound measurements. For imaging the flow field (e.g. Chapter 3), a small amount of air bubbles were added back to the debubbled suspensions to act as tracer particles. This was done by slowly stirring the suspension, then tilting and slowly rotating the container till the bubbles were uniformly distributed.

With the speed of sound measurements, we confirmed two more properties of the suspensions: (1) The speed of sound in density-matched suspensions did not change with time over at least 16 hours. (2) The cornstarch particles do not partially dissolve and thereby affect the solvent's speed of sound. To test this, we prepared suspension samples with cornstarch and DI water at different particle concentrations. The suspensions in this case were not density matched, so the particles settled. We decanted the clear supernatant after 2 hours and measured its speed of sound. No significant difference was observed.

APPENDIX C

RELATION BETWEEN K VALUE AND ACCUMULATED STRAIN IN 3D

For an idealized 2D system we define a Cartesian coordinate with x axis in the transverse and y axis in the longitudinal direction. To obtain the relation between the strain threshold ε_c and the normalized front speeds k we consider how much shear strain a suspension element experiences when it accelerates from $u_y = 0$ to $u_y = U_\mathrm{p}$. We consider the propagation in the transverse and longitudinal directions separately as two quasi-1D problems. Exemplary sketches of the velocity profiles are provided in Supplementary Fig. 5. The experimental data did not show a significant change in front width, so here we assume the shape of the front does not change during propagation. In this case the velocity profiles can be expressed as

$$u_y(x,t) = f_\mathrm{t}(x - v_\mathrm{ft}t) \tag{C1}$$

in the transverse direction and

$$u_y(y,t) = f_\mathrm{l}(y - v_\mathrm{fl}t) \tag{C2}$$

in the longitudinal direction. In both equations t is time, v_ft and v_fl are front propagation speeds. $f_\mathrm{t}(X)$ and $f_\mathrm{l}(X)$ are functions that satisfy $f_\mathrm{t} = f_\mathrm{l} = U_\mathrm{p}$ as $X \to -\infty$ and $f_\mathrm{t} = f_\mathrm{l} = 0$ as $X \to +\infty$.

On either side of the impactor the front propagates in transverse direction and the front speed $v_\mathrm{ft} = k_\mathrm{t}U_\mathrm{p}$, while the suspension itself is sheared longitudinally by the advancing front. The acceleration of a suspension element is then

$$\frac{Du_y(x,t)}{Dt} = \frac{\partial f_\mathrm{t}}{\partial t} = -k_\mathrm{t}U_\mathrm{p}f'_\mathrm{t} = -k_\mathrm{t}U_\mathrm{p}\frac{\partial u_y}{\partial x}, \tag{C3}$$

where D/Dt is the material derivative and $f'_\mathrm{t} = df_\mathrm{t}(X)/dX$. Below the impactor there

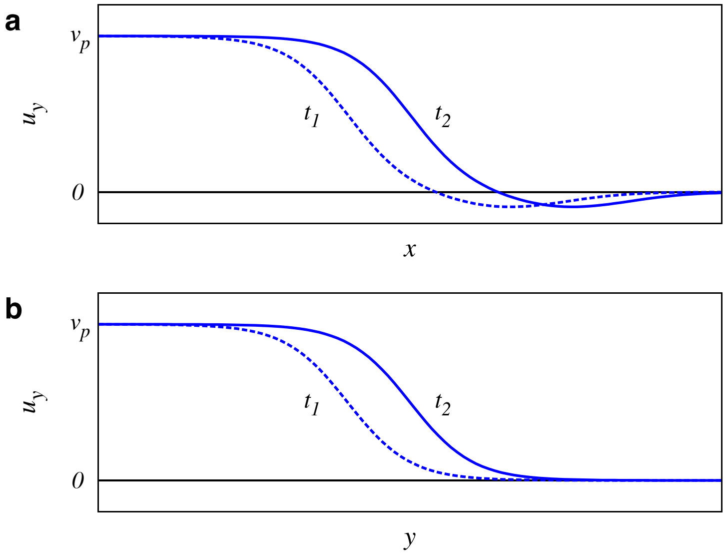

Figure C.1: Schematic illustrations of the front profiles along the transverse (x) and longitudinal (y) directions in 2D. (a) Front profiles in the transverse direction at two times t_1 and t_2 ($t_2 > t_1$). In the jammed region $u_y = U_p$ and in the shear zone it drops quickly to zero. It goes slightly negative at larger x because of the circulation outside of the jammed region, which can be seen in Fig. 3.2. U_p returns back to zero far away from the impactor. (b) Front profiles in the longitudinal direction at t_1 and t_2. Both front profiles $f_t(x - U_{kt}t)$ and $f_l(y - U_{kl}t)$ approach U_p when x or $y \to 0$ and approach 0 when x or $y \to +\infty$.

are two differences: one is that the suspension element now moves along the propagation direction of the front and the other is that $v_{\mathrm{fl}} = (k_{\mathrm{l}} + 1)U_{\mathrm{p}}$ as defined in Eq. 3. The acceleration then becomes

$$\begin{aligned} \frac{Du_y(y,t)}{Dt} &= \frac{\partial f_{\mathrm{l}}}{\partial t} + (u_y \frac{\partial}{\partial y}) f_{\mathrm{l}} = [u_y - (k_{\mathrm{l}} + 1)U_{\mathrm{p}}] f_{\mathrm{l}}' \\ &= [u_y - (k_{\mathrm{l}} + 1)U_{\mathrm{p}}] \frac{\partial u_y}{\partial y}. \end{aligned} \tag{C4}$$

Now we look at the relation between the local shear rate $\dot{\varepsilon}$ and the velocity gradient. In general, for an incompressible 2D fluid the shear rate tensor is

$$\dot{\boldsymbol{\varepsilon}} = \begin{bmatrix} \frac{\partial u_x}{\partial x} & \frac{1}{2}(\frac{\partial u_x}{\partial y} + \frac{\partial u_y}{\partial x}) \\ \frac{1}{2}(\frac{\partial u_x}{\partial y} + \frac{\partial u_y}{\partial x}) & \frac{\partial u_y}{\partial y} \end{bmatrix},$$

where $\frac{\partial u_x}{\partial x} = -\frac{\partial u_y}{\partial y}$. From experimental observation we have $\frac{\partial u_x}{\partial y} \ll \frac{\partial u_y}{\partial x}$. For the transverse direction, where simple shear dominates, the diagonal terms vanish and the shear rate tensor becomes

$$\dot{\boldsymbol{\varepsilon}}_\mathrm{t} = \begin{bmatrix} 0 & \frac{1}{2}\frac{\partial u_y}{\partial x} \\ \frac{1}{2}\frac{\partial u_y}{\partial x} & 0 \end{bmatrix},$$

while for pure shear in the longitudinal direction the off-diagonal terms vanish and we have

$$\dot{\boldsymbol{\varepsilon}}_\mathrm{l} = \begin{bmatrix} -\frac{\partial u_y}{\partial y} & 0 \\ 0 & \frac{\partial u_y}{\partial y} \end{bmatrix}.$$

In either case the matrix has two eigenvalues with the same magnitude but opposite sign and the eigenvalues represent the shear rate on the principal axes. Thus we can represent the shear intensities by the tensors' positive eigenvalues: $\dot{\varepsilon}_\mathrm{l} = |\frac{\partial u_y}{\partial y}| = -\frac{\partial u_y}{\partial y}$ and $\dot{\varepsilon}_\mathrm{t} = \frac{1}{2}|\frac{\partial u_y}{\partial x}| = -\frac{1}{2}\frac{\partial u_y}{\partial x}$.

Using the velocity gradient, we relate the local shear rate with the acceleration of the element:

$$\dot{\varepsilon}_\mathrm{t} = \frac{1}{2}\frac{1}{k_\mathrm{t}U_\mathrm{p}}\frac{Du_y}{Dt}, \tag{C5}$$

$$\dot{\varepsilon}_\mathrm{l} = \frac{1}{(k_\mathrm{l}+1)U_\mathrm{p} - u_y}\frac{Du_y}{Dt}. \tag{C6}$$

Consequently, the total shear strain ε a suspension element experiences before jamming is:

$$\varepsilon_\mathrm{t} = \int_0^\infty \dot{\varepsilon}_\mathrm{t} dt = \int_0^{U_\mathrm{p}} \frac{1}{2k_\mathrm{t}U_\mathrm{p}} du_y = \frac{1}{2k_\mathrm{t}}, \tag{C7}$$

and

$$\varepsilon_\mathrm{l} = \int_0^\infty \dot{\varepsilon}_\mathrm{l} dt = \int_0^{U_\mathrm{p}} \frac{1}{(k_\mathrm{l}+1)U_\mathrm{p} - u_y} du_y = \ln(\frac{k_\mathrm{l}+1}{k_\mathrm{l}}). \tag{C8}$$

Eq. C8 gives $\varepsilon_\mathrm{l} \approx 1/k_\mathrm{l}$ for $k_\mathrm{l} \gg 1$. If we assume the strain threshold to jamming ε_c is isotropic, then $k_\mathrm{t} = 1/(2\varepsilon_\mathrm{c})$ and $k_\mathrm{l} = 1/(e^{\varepsilon_\mathrm{c}} - 1)$.

APPENDIX D

RELATION BETWEEN K_{L} AND K_{T} IN 3D

In 3D the shear rate tensor is shown in equation 3.1. In the longitudinal direction pure shear dominates and the shear rate tensor is

$$\dot{\boldsymbol{\varepsilon}}_{\mathrm{l}} = \begin{bmatrix} \frac{\partial u_r}{\partial r} & 0 & 0 \\ 0 & \frac{u_r}{r} & 0 \\ 0 & 0 & \frac{\partial u_z}{\partial z} \end{bmatrix}, \tag{D1}$$

where $\frac{\partial u_r}{\partial r} \approx \frac{u_r}{r}$ and $\frac{\partial u_r}{\partial r} + \frac{u_r}{r} + \frac{\partial u_z}{\partial z} = 0$. In the transverse direction simple shear dominates. This gives

$$\dot{\boldsymbol{\varepsilon}}_{\mathrm{t}} \approx \begin{bmatrix} 0 & 0 & \frac{1}{2}\frac{\partial u_z}{\partial r} \\ 0 & 0 & 0 \\ \frac{1}{2}\frac{\partial u_z}{\partial r} & 0 & 0 \end{bmatrix}, \tag{D2}$$

where we have used $\frac{\partial u_r}{\partial z} \ll \frac{\partial u_z}{\partial r}$. Note that though the system is three-dimensional simple shear only operates in the rz plane while leaving the azimuthal direction invariant. The eigenvalues become $\dot{e}_{\mathrm{l}} = \{-\frac{1}{2}\frac{\partial u_z}{\partial z}, -\frac{1}{2}\frac{\partial u_z}{\partial z}, \frac{\partial u_z}{\partial z}\}$ and $\dot{e}_{\mathrm{t}} = \{-\frac{1}{2}\frac{\partial u_z}{\partial r}, 0, \frac{1}{2}\frac{\partial u_z}{\partial r}\}$. Unlike the 2D case, we cannot simply use a positive eigenvalue to represent the shear intensity. However, we can define infinitesimal strains e_i $(i = 1, 2, 3)$ along the three principal axes and rank-order them according to $e_1 > e_2 > e_3$. Following the definition given in Ref. [96], the "strain intensity" $\mathscr{D}$ is

$$\begin{aligned} \mathscr{D} &= \sqrt{\left(ln\frac{1+e_1}{1+e_2}\right)^2 + \left(ln\frac{1+e_2}{1+e_3}\right)^2} \\ &\approx \sqrt{(e_1 - e_2)^2 + (e_2 - e_3)^2}. \end{aligned} \tag{D3}$$

For pure shear in the longitudinal direction $e_1 = e_2 = -e_3/2$ and $\dot{e}_3 = \frac{\partial u_z}{\partial z}$, so $\mathscr{D}_{\mathrm{l}} \approx \frac{3}{2}|e_3|$, which leads to $\dot{\mathscr{D}}_{\mathrm{l}} \approx -\frac{3}{2}\frac{\partial u_z}{\partial z}$. For simple shear in the transverse direction $e_1 = -e_3$, $e_2 = 0$ and $\dot{e}_3 = \frac{1}{2}\frac{\partial u_z}{\partial r}$. This leads to $\mathscr{D}_{\mathrm{t}} \approx \sqrt{2}|e_3|$, and therefore $\dot{\mathscr{D}}_{\mathrm{t}} \approx -\frac{\sqrt{2}}{2}\frac{\partial u_z}{\partial r}$. Following the procedure for the 2D case we have

$$\dot{\mathscr{D}}_{\mathrm{t}} = \frac{\sqrt{2}}{2}\frac{1}{k_{\mathrm{t}}U_{\mathrm{p}}}\frac{Du_z}{Dt}, \tag{D4}$$

$$\dot{\mathscr{D}}_{\mathrm{l}} = \frac{3}{2}\frac{1}{(k_{\mathrm{l}}+1)U_{\mathrm{p}} - u_z}\frac{Du_z}{Dt}. \tag{D5}$$

Integration then leads to

$$\mathscr{D}_{\mathrm{t}} = \frac{\sqrt{2}}{2}\frac{1}{k_{\mathrm{t}}},\ \mathscr{D}_{\mathrm{l}} = \frac{3}{2}\ln\left(\frac{k_{\mathrm{l}}+1}{k_{\mathrm{l}}}\right). \tag{D6}$$

Now we again assume that the system shear-jams when $\mathscr{D}$ reaches a threshold strain value $\mathscr{D}_{\mathrm{c}}$, independent of the type of shear it experiences. From this we find

$$k_{\mathrm{l}}^{*} = \frac{1}{e^{\sqrt{2}/(3k_{\mathrm{t}}^{*})} - 1}. \tag{D7}$$

and $k_{\mathrm{l}}^{*}/k_{\mathrm{t}}^{*} \approx 3/\sqrt{2} \approx 2.12$ for large k.

APPENDIX E

SOME CALCULATIONS REGARDING THE GENERALIZED MODEL

Eq. 10 in the main text is an approximate relation between γ_∞ and γ^* in the regime of sufficiently fast U_0 where the front speed can be assumed constant. To keep the calculation simple, we make three approximations that are appropriate for this high speed limit: First, we approximate Eq. 8 in the main text by

$$\Sigma \approx \widetilde{\eta}_0 \cdot \dot{\gamma} \left[\phi_{\mathrm{eff}} - \phi\right]^{-2}, \tag{E1}$$

where $\widetilde{\eta}_0 \equiv \eta_0 \phi_0^2$. Second, in this limit Σ is much larger than Σ^*, so we take $f(\Sigma) \approx 1$. Finally, since the front profile has an approximately invariant shape while propagating, the accumulated strain can be written as $\gamma(x,t) = \gamma(U_{\mathrm{f}} t - x) \equiv \gamma(X)$. This leads to

$$\gamma' \equiv \frac{d\gamma(X)}{dX} = \frac{1}{U_{\mathrm{f}}} \frac{\partial \gamma}{\partial t} = -\frac{\partial \gamma}{\partial x}, \tag{E2}$$

and

$$\gamma'' \equiv \frac{d^2\gamma(X)}{dX^2} = \frac{1}{U_{\mathrm{f}}^2} \frac{\partial^2 \gamma}{\partial t^2} = \frac{\partial^2 \gamma}{\partial x^2}. \tag{E3}$$

Plugging Eq. E1 into the equation of motion:

$$\rho \frac{\partial^2 \gamma}{\partial t^2} = \frac{\partial^2 \Sigma}{\partial x^2}, \tag{E4}$$

we get

$$\rho \frac{\partial^2 \gamma}{\partial t^2} = \frac{\partial^2}{\partial x^2} \left\{ \frac{\widetilde{\eta}_0 \dot{\gamma}}{\left[(\phi_0 - \phi_{\mathrm{m}}) e^{-\gamma/\gamma^*} + \phi_{\mathrm{m}} - \phi\right]^2} \right\}. \tag{E5}$$

Using Eq. E2 and Eq. E3, we obtain

$$\frac{d^2}{dX^2}\left\{\rho U_{\mathrm{f}}^2\gamma - \frac{\widetilde{\eta}_0 U_{\mathrm{f}}\gamma'}{[(\phi_0-\phi_{\mathrm{m}})e^{-\gamma/\gamma^*}+\phi_{\mathrm{m}}-\phi]^2}\right\} = 0,$$

which leads to

$$\rho U_{\mathrm{f}}^2\gamma - \frac{\widetilde{\eta}_0 U_{\mathrm{f}}\gamma'}{[(\phi_0-\phi_{\mathrm{m}})e^{-\gamma/\gamma^*}+\phi_{\mathrm{m}}-\phi]^2} = C_1 X + C_2, \tag{E6}$$

where C_1 and C_2 are constants. In the region not yet reached by the front, both γ and γ' are zero. This means that as $X \to -\infty$ (at large x or small t), the left hand side of Eq. E6 is zero, so the constants should be $C_1 = C_2 = 0$, and we obtain a first order equation governing the evolution of γ:

$$\frac{d\gamma}{dX} = \frac{\rho U_{\mathrm{f}}}{\widetilde{\eta}_0}\gamma\cdot\left[(\phi_0-\phi_{\mathrm{m}})e^{-\gamma/\gamma^*}+\phi_{\mathrm{m}}-\phi\right]^2. \tag{E7}$$

It has two fixed points. For any given x, γ increases with time from an unstable fixed point $\gamma = 0$ to a half-stable fixed point, which is the asymptotic accumulated strain in Eq. 4.19:

$$\gamma_\infty = \gamma^*\cdot\ln\frac{\phi_0-\phi_{\mathrm{m}}}{\phi-\phi_{\mathrm{m}}}.$$

Written as a function of the rescaled packing fraction Φ defined in Eq. 4.7, it becomes

$$\gamma_\infty = -\gamma^*\ln\Phi. \tag{E8}$$

This approximate result captures the relation between γ_∞ and γ^* very well. In Fig. E.1a we compare the numerically calculated k and γ_∞ at $\gamma^* = 0.197$ and $U_0 = 1$ m/s with Eq. 4.19.

Using Eqs. E2 and E7, we can write out the expression for the shear rate:

$$\dot{\gamma} = \left\{\frac{\rho k^2}{\widetilde{\eta}_0}\gamma\cdot\left[(\phi_0-\phi_{\mathrm{m}})e^{-\gamma/\gamma^*}+\phi_{\mathrm{m}}-\phi\right]^2\right\}U_0^2, \tag{E9}$$

where we have replaced U_{f} by kU_0. The maximum shear rate $\dot{\gamma}_{\mathrm{max}}$ is achieved at γ_{m}, where the function in the curly brackets reaches its peak. By calculating the first derivative, we

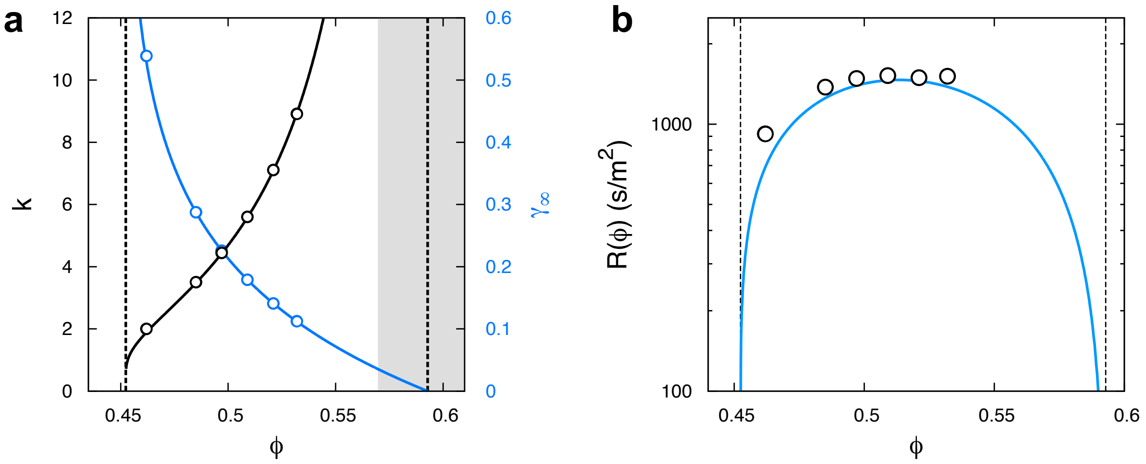

Figure E.1: (a) Dimensionless front propagation speed k and asymptotic accumulated strain γ_∞ at different packing fraction ϕ obtained numerically at $\gamma^* = 0.197$ and $U_0 = 1$ m/s. The solid curves show Eq. 4.19 and its reciprocal at the same γ^*. (b) Comparison of $R(\phi)$ obtained from the numerical calculation (open circles) with the prediction of Eq. E9 (blue line). The dashed black lines show ϕ_m and ϕ_0.

find that this occurs when

$$e^{-\gamma_\mathrm{m}/\gamma^*}\left(1 - 2\frac{\gamma_\mathrm{m}}{\gamma^*}\right) = \Phi. \tag{E10}$$

This can be evaluated numerically to find γ_m. Plugging γ_m into Eq. E9, we can see that everything in the curly brackets is independent of U_0. As a result, the prediction of the maximum shear rate by the model can be written as

$$\dot{\gamma}_\mathrm{max} = R(\phi) \cdot U_0^2, \tag{E11}$$

where the pre-factor $R(\phi)$ is simply a function of the packing fraction. As shown in Fig. E.1b, $R(\phi)$ vanishes as $\phi \to \phi_0$ and $\phi \to \phi_\mathrm{m}$, but in the range $\phi \in [0.462, 0.532]$, it is relatively flat. This agrees well with the numerical results shown in Fig. 2d in the main text. To extract $R(\phi)$ we fit the calculated $\dot{\gamma}_\mathrm{max}(U_0)$ for each ϕ to Eq. E11. The results are given by the open circles in Fig. E.1b.

REFERENCES

[1] H. A. Barnes, J. F. Hutton, and K. Walters. *An introduction to rheology.* Elsevier, 1989.

[2] A. Einstein. A new determination of the molecular dimensions. *Ann. Phys.*, 19:289–306, 1906.

[3] G. K. Batchelor. The effect of brownian motion on the bulk stress in a suspension of spherical particles. *Journal of Fluid Mechanics*, 83(01):97, 1977.

[4] R. C. Ball and P. Richmond. Dynamics of colloidal dispersions. *Physics and Chemistry of Liquids*, 9(2):99–116, 1980.

[5] A. J. Liu and S. R. Nagel. Jamming is not just cool any more. *Nature*, 396(6706):21–22, 1998.

[6] M. E. Cates, J. P. Wittmer, J. P. Bouchaud, and P. Claudin. Jamming force chains and fragile matter. *Physical Review Letters*, 81(9):4, 1998.

[7] S. H. Maron and P. E. Pierce. Application of ree-eyring generalized flow theory to suspensions of spherical particles. *Journal of Colloid Science*, 11:80–95, 1956.

[8] I. M. Krieger and T. J. Dougherty. A mechanism for non-newtonian flow in suspensions of rigid spheres. *Transactions of the Society of Rheology*, 3(1):137–152, 1959.

[9] J. F. Brady. The rheological behavior of concentrated colloidal dispersions. *The Journal of Chemical Physics*, 99(1):567–581, 1993.

[10] H. M. Shewan and J. R. Stokes. Analytically predicting the viscosity of hard sphere suspensions from the particle size distribution. *Journal of Non-Newtonian Fluid Mechanics*, 222:72–81, 2015.

[11] E. Brown and H. M. Jaeger. Shear thickening in concentrated suspensions: phenomenology, mechanisms and relations to jamming. *Rep Prog Phys*, 77(4):046602, 2014.

[12] V. Trappe, V. Prasad, L. Cipelletti, P. N. Segre, and D. A. Weitz. Jamming phase diagram for attractive particles. *Nature*, 411:772–775, 2001.

[13] E. Brown, N. A. Forman, C. S. Orellana, H. Zhang, B. W. Maynor, D. E. Betts, J. M. DeSimone, and H. M. Jaeger. Generality of shear thickening in dense suspensions. *Nat Mater*, 9(3):220–4, 2010.

[14] B. J. Maranzano and N. J. Wagner. The effects of particle size on reversible shear thickening of concentrated colloidal dispersions. *The Journal of Chemical Physics*, 114(23):10514–10527, 2001.

[15] X. Cheng, J. H. McCoy, J. N. Israelachvili, and I. Cohen. Imaging the microscopic structure of shear thinning and thickening colloidal suspensions. *Science*, 333:1276–1279, 2011.

[16] E. Brown and H. M. Jaeger. Through thick and thin. *Science*, 333:1230–1231, 2011.

[17] N. J. Wagner and J. F. Brady. Shear thickening in colloidal dispersions. *Physics Today*, 62(10):27–32, 2009.

[18] J. F. Brady and G. Bossis. The rheology of concentrated suspensions of spheres in simple shear flow by numerical simulation. *Journal of Fluid Mechanics*, 155:105, 1985.

[19] J. F. Brady and G Bossis. Stokesian dynamics. *Annual Review of Fluid Mechanics*, 20:111, 1988.

[20] H. A. Barnes. Shear-thickening (“dilatancy”) in suspensions of nonaggregating solid particles dispersed in newtonian liquids. *Journal of Rheology*, 33(2):329, 1989.

[21] Eric Brown and Heinrich M. Jaeger. The role of dilation and confining stresses in shear thickening of dense suspensions. *Journal of Rheology*, 56(4):875, 2012.

[22] Q. Xu, S. Majumdar, E. Brown, and H. M. Jaeger. Shear thickening in highly viscous granular suspensions. *Europhysics Letters*, 107(6):68004, 2014.

[23] N. Y. Lin, B. M. Guy, M. Hermes, C. Ness, J. Sun, W. C. Poon, and I. Cohen. Hydrodynamic and contact contributions to continuous shear thickening in colloidal suspensions. *Phys Rev Lett*, 115(22):228304, 2015.

[24] D. Bi, J. Zhang, B. Chakraborty, and R. P. Behringer. Jamming by shear. *Nature*, 480(7377):355–8, 2011.

[25] I. R. Peters, S. Majumdar, and H. M. Jaeger. Direct observation of dynamic shear jamming in dense suspensions. *Nature*, 532(7598):214–217, 2016.

[26] Corey S. O'Hern, Leonardo E. Silbert, Andrea J. Liu, and Sidney R. Nagel. Jamming at zero temperature and zero applied stress: The epitome of disorder. *Physical Review E*, 68(1):011306, 2003.

[27] N. Kumar and S. Luding. Memory of jamming - multiscale models for soft and granular matter. *Granular Matter*, 18(3), 2016.

[28] W. Zheng, H. Liu, and N. Xu. Shear-induced solidification of athermal systems with weak attraction. *Phys Rev E*, 94(6-1):062608, 2016.

[29] E. DeGiuli, G. Düring, E. Lerner, and M. Wyart. Unified theory of inertial granular flows and non-brownian suspensions. *Phys. Rev. E*, 91(6):062206, 06 2015.

[30] Edan Lerner, Gustavo Düring, and Matthieu Wyart. A unified framework for non-brownian suspension flows and soft amorphous solids. *Proceedings of the National Academy of Sciences*, 109(13):4798–4803, 2012.

[31] N. Fernandez, R. Mani, D. Rinaldi, D. Kadau, M. Mosquet, H. Lombois-Burger, J. Cayer-Barrioz, H. J. Herrmann, N. D. Spencer, and L. Isa. Microscopic mechanism for shear thickening of non-brownian suspensions. *Physical Review Letters*, 111(10):108301, 2013.

[32] F. Boyer, E. Guazzelli, and O. Pouliquen. Unifying suspension and granular rheology. *Physical Review Letters*, 107(18):188301, 2011.

[33] J. R. Royer, D. L. Blair, and S. D. Hudson. Rheological signature of frictional interactions in shear thickening suspensions. *Phys Rev Lett*, 116(18):188301, 2016.

[34] J. Comtet, G. Chatte, A. Nigues, L. Bocquet, A. Siria, and A. Colin. Pairwise frictional profile between particles determines discontinuous shear thickening transition in non-colloidal suspensions. *Nat Commun*, 8:15633, 2017.

[35] C. Clavaud, A. Berut, B. Metzger, and Y. Forterre. Revealing the frictional transition in shear-thickening suspensions. *Proceedings of the National Academy of Science*, 114(20):5147–5152, 2017.

[36] R. Seto, R. Mari, J. F. Morris, and M. M. Denn. Discontinuous shear thickening of frictional hard-sphere suspensions. *Physical Review Letters*, 111(21):218301, 2013.

[37] R. Mari, R. Seto, J. F. Morris, and M. M. Denn. Nonmonotonic flow curves of shear thickening suspensions. *Phys. Rev. E*, 91(5):052302, 2015.

[38] C. Ness and J. Sun. Shear thickening regimes of dense non-brownian suspensions. *Soft Matter*, 12(3):914–924, 2016.

[39] A. Singh, R. Mari, M. M. Denn, and J. F. Morris. A constitutive model for simple shear of dense frictional suspensions. *Journal of Rheology*, 62(2):457–468, 2018.

[40] S. Sarkar, D. Bi, J. Zhang, J. Ren, R. P. Behringer, and B. Chakraborty. Shear-induced rigidity of frictional particles: Analysis of emergent order in stress space. *Physical Review E*, 93(4):042901, 2016.

[41] M. Wyart and M. E. Cates. Discontinuous shear thickening without inertia in dense non-brownian suspensions. *Physical Review Letters*, 112(9):098302, 2014.

[42] C. Song, P. Wang, and H. A. Makse. A phase diagram for jammed matter. *Nature*, 453(7195):629–632, 2008.

[43] L. C. Hsiao, S. Jamali, E. Glynos, P. F. Green, R. G. Larson, and M. J. Solomon. Rheological state diagrams for rough colloids in shear flow. *Phys Rev Lett*, 119(15):158001, 2017.

[44] C. P. Hsu, S. N. Ramakrishna, M. Zanini, N. D. Spencer, and L. Isa. Roughness-dependent tribology effects on discontinuous shear thickening. *Proc Natl Acad Sci*, 115(20):5117–5122, 2018.

[45] N. James, E. Han, J. Jureller, and H. M. Jaeger. Interparticle hydrogen bonding can elicit shear jamming in dense suspensions. *arXiv preprint arXiv:1707.09401*, 2017.

[46] M Trulsson, E DeGiuli, and M Wyart. Effect of friction on dense suspension flows of hard particles. *arXiv preprint arXiv:1606.07650*, 2016.

[47] F. Blanc, F. Peters, and E. Lemaire. Local transient rheological behavior of concentrated suspensions. *Journal of Rheology*, 55(4):835–854, 2011.

[48] B. M. Guy, M. Hermes, and W. C. Poon. Towards a unified description of the rheology of hard-particle suspensions. *Phys Rev Lett*, 115(8):088304, 2015.

[49] Z. Pan, H. de Cagny, B. Weber, and D. Bonn. S-shaped flow curves of shear thickening suspensions: direct observation of frictional rheology. *Phys Rev E Stat Nonlin Soft Matter Phys*, 92(3):032202, 2015.

[50] Bin Liu, Michael Shelley, and Jun Zhang. Focused force transmission through an aqueous suspension of granules. *Physical Review Letters*, 105(18):188301, 2010.

[51] Stefan von Kann, Jacco H. Snoeijer, Detlef Lohse, and Devaraj van der Meer. Nonmonotonic settling of a sphere in a cornstarch suspension. *Physical Review E*, 84(6):060401, 2011.

[52] S. R. Waitukaitis and H. M. Jaeger. Impact-activated solidification of dense suspensions via dynamic jamming fronts. *Nature*, 487(7406):205–9, 2012.

[53] M. Roche, E. Myftiu, M. C. Johnston, P. Kim, and H. A. Stone. Dynamic fracture of nonglassy suspensions. *Physical Review Letters*, 110(14):148304, 2013.

[54] R. Maharjan, S. Mukhopadhyay, B. Allen, T. Storz, and E. Brown. Constitutive relation for the system-spanning dynamically jammed region in response to impact of cornstarch and water suspensions. *Physical Review E*, 97(5), 2018.

[55] B. Allen, B. Sokol, S. Mukhopadhyay, R. Maharjan, and E. Brown. System-spanning dynamically jammed region in response to impact of cornstarch and water suspensions. *Physical Review E*, 97(5), 2018.

[56] M. I. Smith, R. Besseling, M. E. Cates, and V. Bertola. Dilatancy in the flow and fracture of stretched colloidal suspensions. *Nat Commun*, 1:114, 2010.

[57] I. R. Peters and H. M. Jaeger. Quasi-2d dynamic jamming in cornstarch suspensions: visualization and force measurements. *Soft Matter*, 10(34):6564–70, 2014.

[58] S. R. Waitukaitis, L. K. Roth, V. Vitelli, and H. M. Jaeger. Dynamic jamming fronts. *Europhysics Letters*, 102(4):44001, 2013.

[59] S. R. Nagel. Experimental soft-matter science. *Reviews of Modern Physics*, 89(2):025002, 2017.

[60] M. L. Cowan, I. P. Jones, J. H. Page, and D. A. Weitz. Diffusing acoustic wave spectroscopy. *Phys. Rev. E*, 65:066605, Jun 2002.

[61] S. Manneville, L. Bcu, and A. Colin. High-frequency ultrasonic speckle velocimetry in sheared complex fluids. *The European Physical Journal Applied Physics*, 28(3):361–373, 2004.

[62] T. Gallot, C. Perge, V. Grenard, M. A. Fardin, N. Taberlet, and S. Manneville. Ultrafast ultrasonic imaging coupled to rheometry: principle and illustration. *Rev Sci Instrum*, 84(4):045107, 2013.

[63] X. Jia, C. Caroli, and B. Velicky. Ultrasound propagation in externally stressed granular media. *Phys Rev Lett*, 82(9):1863–1866, 1999.

[64] Y. Khidas and X. Jia. Anisotropic nonlinear elasticity in a spherical-bead pack: influence of the fabric anisotropy. *Phys Rev E Stat Nonlin Soft Matter Phys*, 81(2 Pt 1):021303, 2010.

[65] S. van den Wildenberg, Y. Yang, and X. Jia. Probing the effect of particle shape on the rigidity of jammed granular solids with sound speed measurements. *Granular Matter*, 17(4):419–426, 2015.

[66] V. Langlois and X. Jia. Acoustic probing of elastic behavior and damage in weakly cemented granular media. *Phys Rev E Stat Nonlin Soft Matter Phys*, 89(2):023206, 2014.

[67] Richard S. C. Cobbold. *Foundations of Biomedical Ultrasound*. Oxford University Press, 2007.

[68] C. Errico, J. Pierre, S. Pezet, Y. Desailly, Z. Lenkei, O. Couture, and M. Tanter. Ultrafast ultrasound localization microscopy for deep super-resolution vascular imaging. *Nature*, 527(7579):499–502, 2015.

[69] N. Goldenfeld and L. P. Kadanoff. Simple lessons from complexity. *Science*, 284:87–89, 1999.

[70] R. J. Urick. A sound velocity method for determining the compressibility of finely divided substances. *Journal of Applied Physics*, 18(11):983, 1947.

[71] A. B. Wood. *A Textbook of Sound*. G. Bell & Sons, London, 1941.

[72] V. A. Del Grosso and C. W. Mader. Speed of sound in pure water. *Journal of the Acoustical Society of America*, 52(5B):1442–1446, 1972.

[73] Nykolai Bilaniuk and George S. K. Wong. Speed of sound in pure water as a function of temperature. *Journal of the Acoustical Society of America*, 93(3):1609–1612, 1993.

[74] Roy L. Whistler, James N. Bemiller, and Eugene F. Paschall. *Starch: Chemistry and Technology*. Academic Press Inc., 2nd edition, 1984.

[75] R. F. Tester, J. Karkalas, and X. Qi. Starch - composition, fine structure and architecture. *Journal of Cereal Science*, 39(2):151–165, 2004.

[76] N. H. Hellman and E. H. Melvin. Surface area of starch and its role in water sorption. *Journal of the American Chemical Society*, 72:5186–5188, 1950.

[77] L. Sair and W. R. Fetzer. Water sorption by starches. *Industrial and engineering chemistry*, 36(3):205–208, 1944.

[78] A. Fall, F. Bertrand, D. Hautemayou, C. Mezire, P. Moucheront, A. Lematre, and G. Ovarlez. Macroscopic discontinuous shear thickening versus local shear jamming in cornstarch. *Physical Review Letters*, 114(9):098301, 2015.

[79] Eric Brown and Heinrich M. Jaeger. Dynamic jamming point for shear thickening suspensions. *Physical Review Letters*, 103(8):086001, 2009.

[80] F. Gassmann. Uber die elastizitat poroser medien. *Ver. Natur Gesellschaft*, 96:1–23, 1951.

[81] M. A. Biot. Theory of propagation of elastic waves in a fluid saturated porous solid. i. low-frequency range. *J. Acoust. Soc. Amer.*, 28:168–178, 1956.

[82] R. J. S. Brown and J. Korringa. On the dependence of the elastic properties of a porous rock on the compressibility of the pore fluid. *Geophysics*, 40(4):9, 1975.

[83] M. L. Batzle, D. Han, and R. Hofmann. Fluid mobility and frequency-dependent seismic velocity - direct measurements. *Geophysics*, 71(1):N1–N9, 2006.

[84] D. L. Johnson. Theory of frequency dependent acoustics in patchy-saturated porous media. *J Acoust Soc Am*, 110(2):682–694, 2001.

[85] W. S. Ament. Sound propagation in gross mixtures. *Journal of the Acoustical Society of America*, 25(4):638–641, 1953.

[86] L. Gibiansky and S. Torquato. Rigorous conenction between physical properties of porous rocks. *Journal of Geophysical Research*, 103(B10):23911–23932, 1998.

[87] W. Pabst, E. Gregorova, and G. Ticha. Elasticity of porous ceramics - a critical study of modulus - porosity relations. *Journal of the European Ceramic Society*, 26(7):1085–1097, 2006.

[88] S. R. Waitukaitis. *Impact activated solidification of cornstarch and water suspensions.* Thesis, The University of Chicago, 2014.

[89] G. N. Greaves, A. L. Greer, R. S. Lakes, and T. Rouxel. Poisson's ratio and modern materials. *Nat Mater*, 10(11):823–837, 2011.

[90] O. E. Petel, S. Ouellet, J. Loiseau, D. L. Frost, and A. J. Higgins. A comparison of the ballistic performance of shear thickening fluids based on particle strength and volume fraction. *International Journal of Impact Engineering*, 85:83–96, 2015.

[91] E. J. Windhab and B. Ouriev. Rheological study of concentrated suspensions in pressure-driven shear flow using a novel in-line ultrasound doppler method. *Experiments in Fluids*, 32(2):204–211, 2002.

[92] B. Ouriev and E. J. Windhab. Novel ultrasound based time averaged flow mapping method for die entry visualization in flow of highly concentrated shear-thinning and shear-thickening suspensions. *Measurement Science and Technology*, 14:140–147, 2003.

[93] B. Saint-Michel, H. Bodiguel, S. Meeker, and S. Manneville. Simultaneous concentration and velocity maps in particle suspensions under shear from rheo-ultrasonic imaging. *Physical Review Applied*, 8(1):014023, 2017.

[94] D. J. McClements and M. J. W. Povey. Ultrasound velocity as a probe. *Advances in colloid and interface science*, 27:285–316, 1987.

[95] V. Vitelli and M. van Hecke. Marginal matters. *Nature*, 480:325–326, 2011.

[96] John G. Ramsay and Martin I. Huber. *The Techniques of Modern Structural Geology*, volume 1. Academic Press Inc., 1st edition, 1983.

[97] E. Han, I. R. Peters, and H. M. Jaeger. High-speed ultrasound imaging in dense suspensions reveals impact-activated solidification due to dynamic shear jamming. *Nat Commun*, 7:12243, 2016.

[98] S. Majumdar, I. R. Peters, E. Han, and H. M. Jaeger. Dynamic shear jamming under extension in dense granular suspensions. *Phys. Rev. E*, 95:012603, 2017.

[99] S. R. Waitukaitis, L. K. Roth, V. Vitelli, and H. M. Jaeger. Dynamic jamming fronts. *Europhysics Letters*, 102(4):44001, 2013.

[100] I. Buttinoni, J. Cha, W. H. Lin, S. Job, C. Daraio, and L. Isa. Direct observation of impact propagation and absorption in dense colloidal monolayers. *Proc Natl Acad Sci*, 114(46):12150–12155, 2017.

[101] L. R. Gomez, A. M. Turner, M. van Hecke, and V. Vitelli. Shocks near jamming. *Physical Review Letters*, 108(5):058001, 2012.

[102] L. R. Gomez, A. M. Turner, and V. Vitelli. Uniform shock waves in disordered granular matter. *Physical Review E*, 86(4):041302, 2012.

[103] S. Ulrich, N. Upadhyaya, B. van Opheusden, and V. Vitelli. Shear shocks in fragile networks. *Proc Natl Acad Sci*, 110(52):20929–34, 2013.

[104] D. J. Acheson. *Elementary Fluid Dynamics*. Oxford University Press, 2005.

[105] M. E. Cates and M. Wyart. Granulation and bistability in non-brownian suspensions. *Rheologica Acta*, 53(10-11):755–764, 2014.

[106] M. Hermes, B. M. Guy, W. C. K. Poon, G. Poy, M. E. Cates, and M. Wyart. Unsteady flow and particle migration in dense, non-brownian suspensions. *Journal of Rheology*, 60(5):905–916, 2016.

[107] M. Pailha, M. Nicolas, and O. Pouliquen. Initiation of underwater granular avalanches: Influence of the initial volume fraction. *Physics of Fluids*, 20(11):111701, 2008.

[108] W. H. Boersma, P. J. M. Baets, J. Laven, and H. N. Stein. Time-dependent behavior and wall slip in concentrated shear thickening dispersions. *Journal of Rheology*, 35(6):1093–1120, 1991.

[109] R. J. Urick and W. S. Ament. The propagation of sound in composite media. *Journal of the Acoustical Society of America*, 21(3):115–119, 1949.

[110] A. H. Harker and J. A. G. Temple. Velocity and attenuation of ultrasound in suspensions of particles in fluids. *Journal of Physics D: Applied Physics*, 21:1576–1588, 1988.

[111] H. K. Kytomaa and C. M. Atkinson. Sound propagation in suspensions and acoustic imaging of their microstructure. *Mechanics of Materials*, 16:189–197, 1993.

[112] H. K. Kytomaa. Theory of sound propagation in suspensions: a guide to particle size and concentration characterization. *Powder Technology*, 82:115–121, 1995.

[113] L. Schwartz and T. J. Plona. Ultrasonic propagation in close-packed disordered suspensions. *Journal of Applied Physics*, 55(11):3971, 1984.

[114] Endao Han, Nigel Van Ha, and Heinrich M. Jaeger. Measuring the porosity and compressibility of liquid-suspended porous particles using ultrasound. *Soft Matter*, 13(19):3506–3513, 2017.

[115] J. L. Paterson, A. Hardacre, P. Li, and M. A. Rao. Rheology and granule size distributions of cornstarch dispersions from two genotypes and grown in four regions. *Food Hydrocolloids*, 15:453–459, 2001.